

MULTILAYER CONFIGURATIONS WITH PLASMONIC TRANSDUCERS
NEAR MAGNETIC LAYERS

by
ERDEM ÖĞÜT

Submitted to the Graduate School of Sabanci University
in partial fulfillment of the requirements for the degree of
Doctor of Philosophy

SABANCI UNIVERSITY
AUGUST 2014

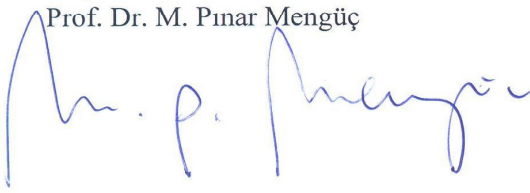
MULTILAYER CONFIGURATIONS WITH PLASMONIC TRANSDUCERS
NEAR MAGNETIC LAYERS

APPROVED BY:

Assoc. Prof. Dr. Kürşat Şendur
(Thesis Supervisor)



Prof. Dr. M. Pınar Mengüç



Assoc. Prof. Dr. Güllü Kızıldaş Şendur



Assoc. Prof. Dr. Cleva Ow-Yang



Assoc. Prof. Dr. Burç Mısırlıoğlu



DATE OF APPROVAL: 06.08.2014

© Erdem Ögüt 2014
All Rights Reserved

MULTILAYER CONFIGURATIONS WITH PLASMONIC TRANSDUCERS NEAR MAGNETIC LAYERS

Erdem Ögüt
Mechatronics Engineering, PhD. Thesis, 2014
Thesis Supervisor: Assoc. Prof. Kürşat Şendur

Keywords: Heat-assisted magnetic recording, integrated heads, nanotransducers, surface plasmon resonance sensors, plasmonics.

ABSTRACT

Magnetic information storage technology has been one of the main technologies that requires a continuous growth due to the need for storing larger amount of data in everyday life. Accordingly, magnetic hard disk drive industry depends on continually increasing areal density. However, historically, specific physical limitations hinder this technology to continually grow. Heat-assisted magnetic recording (HAMR) is an emerging technology that has increased the areal density of conventional recording techniques for hard disc drives. In HAMR, localized optical spots that are produced by integrated heads are utilized to heat the magnetic medium during the recording process. Integrated heads have enabled this increase through localized heating of the recording media during the recording process.

In this thesis, HAMR integrated heads are investigated that are modeled as multilayer configurations with plasmonic films near magnetic films. Multilayer configurations are investigated that minimize radiative and load-induced losses. It is shown that a higher electric field intensity enhancement can be obtained by minimizing radiative and load-induced losses. In order to protect the plasmonic transducer from the load-induced damping effect of the magnetic write head, a novel planarly modeled HAMR head is introduced. By engineering the field gradients in the head, optimum configurations are specified that yield higher field gradient regions in the down-track direction. The planarly layered head is utilized to design a plasmonic planar solid immersion mirror, which is theoretically and experimentally demonstrated to produce intense and localized optical spots beyond the diffraction-limit.

This thesis also demonstrates multilayered surface plasmons resonance sensors with lossy samples that can provide high quality resonances. Surface plasmon resonance sensors operate generally with lossless samples or lossy thin-films. It is demonstrated that surface plasmon resonances can be recovered back when they operate with thick-lossy samples.

ÇOK KATMANLI YAPILARDA MANYETİK KATMANLARIN YAKININDAKİ PLAZMONİK TRANSDÜSERLER

Erdem Ögüt
Mekatronik Mühendisliği, Doktora Tezi, 2014
Tez Danışmanı: Doç. Dr. Kürşat Şendur

Anahtar Kelimeler: Isı destekli manyetik kayıtlama, entegre manyetik kafalar, nanotransdüserler, yüzey plazmon rezonans sensörleri, plazmonik.

ÖZET

Manyetik bilgi kayıtlama teknolojisi, bilgi depolanmasına her geçen gün daha fazla duyulan ihtiyaç sebebiyle sürekli olarak büyümek zorunda olan başlıca teknolojilerden bir tanesidir. Dolayısıyla, manyetik sabit disk sürücü endüstrisi, alansal yoğunlukta süregiden bir artışa bağlıdır. Ancak, tarihsel olarak, belirli fiziksel kısıtlamalar bu teknolojinin sürekli olarak büyümesine engel olmaktadır. Isı destekli manyetik kayıtlama (HAMR) geleneksel kayıtlama teknikleri vasıtasıyla elde edilen alansal yoğunluk değerlerini arttırabilmiş olan, gelişmekte olan bir teknolojidir. HAMR'da, entegre manyetik kafalar tarafından oluşturulan yerleştirilmiş optik beneklerden, manyetik ortamı kayıtlama süreci boyunca ısıtmak için yararlanılmaktadır. Alansal yoğunluktaki bu artışa, kayıtlama süreci boyunca gerçekleşen yerleştirilmiş ısıtma sayesinde entegre kafalar olarak sağlamıştır.

Bu tezde, plazmonik katmanların yakınında bulunan manyetik katmanlardan oluşan çok katmanlı yapılar, HAMR entegre kafaları şeklinde modellenerek incelenmiştir. Işınımsal ve yüke bağlı olarak oluşan kayıplar incelenmiştir. Işınımsal ve yüke bağlı kayıplar minimize edilerek, daha yüksek elektrik alan değerleri elde edilebildiği gösterilmiştir. Plazmonik transdüserleri manyetik yazma kafasının yüke bağlı sönümlenme etkisinden korumak için, düzlemsel katmanlı bir HAMR kafası tanıtılmıştır. Manyetik kafadaki alan gradyanlarının mühendisliği yapılarak, optimum konfigürasyonlar belirlenmiş ve daha yüksek alan gradyan değerlerine ulaşılmıştır. Düzlemsel katmanlı kafa tasarımından yararlanılarak, plazmonik bir katı daldırma aynası tasarlanmış ve hem teorik hem de deneysel olarak incelenerek, katı daldırma aynasının kırınım sınırının ötesinde yerleşmiş optik benekler oluşturabildiği gösterilmiştir.

Bu tez aynı zamanda, çok katmanlı yüzey plazmon rezonans sensörlerinde yüksek kayıplı örnekler mevcut olduğunda yüksek kalitede rezonanslar sağlayabilen konfigürasyonları da incelemektedir. Yüzey plazmon rezonans sensörleri genellikle kayıpsız ya da kayıplı ince-filmler ile çalışmaktadır. Kalın ve kayıplı filmler ile çalışıldığında yüzey plazmon rezonanslarının geri getirebildiği gösterilmiştir.

ACKNOWLEDGEMENTS

First and foremost, I want to convey my sincere thanks to my thesis advisor, Dr. Kürşat Şendur, for his continuous support during my Ph.D. studies. He has been not only a mentor for me during my Ph.D. studies, but also a role model, providing me a lot about conducting research in a specific area. I want to express my thanks to my thesis dissertation jury, Dr. M. Pınar Mengüç, Dr. Güllü Kızıldaş Şendur, Dr. Cleva Ow-Yang, and Dr. Burç Mısırlıođlu for their valuable comments about my Ph.D. dissertation.

Many thanks to Cenk Yanık and Rüştü Umut Tok for their support in the fabrication processes. This thesis would not come true without the support and unrequited love of my wife, Dicle. She has been a continuous source of love, understanding, and encouragement for me. Finally, I want to thank to my family for their support and care during my Ph.D. studies.

TABLE OF CONTENTS

1	INTRODUCTION.....	23
1.1	Definition of the Problem, Importance, and Original Value	23
1.2	Literature Survey	27
1.2.1	HAMR Head Design and Recording Demonstrations	27
1.2.2	HAMR Media Design	41
1.2.3	Thermal Aspects of HAMR	42
1.2.4	Magneto-Optics Sensors	48
1.3	Contribution.....	53
1.4	Thesis Outline.....	54
2	INTEGRATING MAGNETIC HEADS WITH PLASMONIC NANOSTRUCTURES IN MULTILAYER CONFIGURATIONS.....	55
2.1	Methodology.....	57
2.2	Losses and Evanescent Coupling of Multilayers.....	58
2.3	Zero Reflection Multilayers.....	62
2.4	Conclusion	64
3	INVESTIGATING THE RELIABILITY AND PERFORMANCE OF HAMR INTEGRATED HEADS VIA MULTILAYER CONFIGURATIONS.....	65
3.1	Weakening and Losing Plasmon Resonances in the Presence of Magnetic Layers.....	65
3.2	Recovering the Intensity Enhancement and Plasmon Resonances via Thin-Film Coatings	69
3.3	Improving Optical Field Intensities and Optical Field Gradients to Facilitate HAMR Recording	71
3.3.1	Methodology	73
3.3.2	Engineering the Field Gradient	75
3.4	Predicting and Minimizing the Wavevector Shift in Dispersion Curves	80
3.5	Conclusion	83
4	PLASMONIC PLANAR SOLID IMMERSION MIRROR (PLASMONIC PSIM) 85	
4.1	Introduction	85

4.2	Planar Transducers for Heat-Assisted Magnetic Recording.....	91
4.2.1	Planar Transducers With Diffraction-Limited Optical Spots.....	91
4.2.2	Planar Transducers With Optical Spots Beyond the Diffraction-Limit..	98
4.2.2.1	Introduction	98
4.2.2.2	Plasmonic PSIMs.....	99
4.2.3	Near-Field Scanning Optical Microscope (NSOM) Measurements of the Plasmonic PSIM	106
4.3	Conclusion	108
5	RECOVERING DAMPED PLASMON RESONANCES IN SURFACE PLASMON RESONANCE SENSORS WITH LOSSY LAYERS	109
5.1	Introduction	109
5.2	Methodology.....	111
5.2.1	Obtaining and Tuning the Poles of Various SPR Sensor Configurations to Recover Plasmon Resonances	111
5.2.2	Obtaining the Electric Field Profiles of Various Multilayer Configurations	113
5.3	Results and Discussion	115
5.3.1	Damping of Plasmon Resonances Near Absorbing Layers	115
5.3.2	Recovering Surface Plasmon Resonances with a Glass-Gold-Sensing-Dielectric-Cobalt Configuration.....	117
5.4	Conclusion	120
6	CONCLUSION	121
7	REFERENCES	124

LIST OF FIGURES

Figure 1.1 Areal density in magnetic storage devices as a function of time. The curve with empty squares represents demonstrations in research laboratories and the curve with filled squares represents the areal density of products. The blue line represents the 100 Gbit/inch ² where the switch from longitudinal recording to perpendicular recording occurred. The red line indicates the expected limits of the state-of-the-art perpendicular recording.	25
Figure 1.2 Schematic comparison of perpendicular recording and heat-assisted magnetic recording.	25
Figure 1.3 Hysteresis loops for various material compositions. As the temperature increases the area that is enclosed by the M-H curves reduces. Courtesy of Ikemoto et.al., IEEE Trans. Magn., 44, 11, (2008).....	26
Figure 1.4 Schematic comparison of the HAMR heating and cooling process. The coercivity value is reduced below the head field value to enable recording. Courtesy of Wu. et. al., IEEE Trans. Magn., 49, 2, (2013).	26
Figure 1.5 (a) A double grating structure that is placed at the end of a waveguide, and (b) the metallic slit at the center of the grating structure. Courtesy of D.-S. Lim et. al., Asia Pacific Magnetic Recording Conference, pp. 1-2, 2006.....	29
Figure 1.6 (a) Schematic representation of the plan view and optical image of the dielectric and plasmonic waveguide, and (b) experimental realization of the coupling phenomena. Courtesy of Y. Kong et. al., IEEE Trans. Magn, vol. 47, pp. 2364-2367, 2011.	30
Figure 1.7 (a) A fabricated PSIM on a ceramic substrate and (b) the implemented micro-optical structure with lithographic techniques, (c) NSOM image of a focused optical spot by the PSIM. Courtesy of W. A. Challener et. al., vol. 13, no. 18, pp. 7189-7197, 2005.	31

Figure 1.8 (a) Schematic representation of the PSIM with a near-field nanotransducer at its focus, and (b) photothermal images at various operation wavelengths. Courtesy of C. Peng et. al., IEEE Trans. Magn, vol. 48, pp. 1801-1806, 2012.	31
Figure 1.9 Schematic illustration of the near-field transducer near a recording medium. Courtesy of C. Peng, Appl. Phys. Lett, vol. 112, 043108, 2012.....	33
Figure 1.10 Normalized absorption profile for (a) A 12 x 12 x 12 nm bit patterned FePt media and (b) a continuous FePt media. Courtesy of A. Ghoreyshi et. al., J. Appl. Phys., vol. 115, 17B719, 2014.....	33
Figure 1.11 Electric field intensity distributions of the (a) C-aperture nanotransducer and the lollipop nanotransducer without the recording media, (b) with the recording media, and (c) electric field profiles in the presence of the recording media. Courtesy of B. Xu et. al., IEEE Trans. Magn., vol. 49, pp. 3580-3583, 2013.	34
Figure 1.12 (a) Intensity distributions at the top surface of the cobalt layer with various slit and rectangular holes dimensions. The cobalt layer is placed 15 nm below the bottom surface of the transducer, and (b) the gold transducer that is coupled with a plasmonic waveguide. Courtesy of S. Omodani et. al., J. Appl. Phys., vol. 105, 013101, 2009.	36
Figure 1.13 (a) Schematic representation of the triangular nanoantenna, the wing structure, and the magnetic pole, and (b) absorbed power distribution in the recording medium. Courtesy of T. Matsumoto et. al., Opt. Express, vol. 20, no. 17, pp. 18946-18954, 2012.....	38
Figure 1.14 Recorded marks in a phase-change medium by the PSIM at (a) 833 nm, (b) 488 nm for 10 mW incident optical power, and (c) 488 nm for 15 mW incident optical power. Courtesy of C. Peng et. al., Appl. Phys. Lett., vol. 87, 151105, 2005.	39
Figure 1.15 (a) Schematic representation of a near-field nanotransducer above a recording medium, (b) magnetic force microscopy images of a recorded track. Courtesy of W. A. Challener et. al., Nature Photon., 3, 220-224, 2009.	39
Figure 1.16 (a) Schematic representation of the integrated recording head, and (b) magnetic force microscopy image of the written tracks on a bit-patterned medium. Courtesy of B. C. Stipe, Nature Photon. 4, pp. 484-488, 2010.....	40

Figure 1.17 Schematic representation of two types of recording media. (a) A continuous recording medium, and (b) a patterned recording medium. Courtesy of K. Şendur et. al., <i>Appl. Phys. Lett.</i> , 94, 032503, 2009.	41
Figure 1.18 (a) Recording medium, MgO interlayer, and NiTa seed layer, and (b) electric field intensity distribution in the recording layer. Courtesy of B. Xu et. al., <i>IEEE Trans. Magn.</i> , vol. 49, no. 6, 2013.	42
Figure 1.19 Schematic representation of the longitudinal recording process. (a) The magnetic head and the recording layer before the recording process, (b) a produced transition as a result of the switch in the head field, and (c) the transition moving along the disk motion away from the gap of the magnetic head. Courtesy of T. Rausch et. al., <i>IEEE Trans. Magn.</i> , vol. 40, no. 1, 2004.....	43
Figure 1.20 Schematic illustration of the HAMR head and the recording medium, (b) temperature distributions in the medium, and (c) thermal spot sizes in the medium. Courtesy of D.-S. Lim et. al., <i>IEEE Trans. Magn.</i> , vol. 45, no. 10, 2009.....	45
Figure 1.21 (a) Schematic representation of the rectangular nanotransducer and the writer pole, (b) electric field intensity distribution on the cut-plane through the nanotransducer in the air-bearing surface, and (c) electric field intensity distribution on the cut-plane through the nanotransducer in the recording medium. Courtesy of J. Li et. al., <i>IEEE Trans. Magn.</i> , vol. 49, no. 7, 2013.....	45
Figure 1.22 (a) Schematic representation of the optical waveguide and the near-field nanotransducer, and (b) the two-stage heating scheme of the recording medium. Courtesy of S. Xiong et. al., <i>Appl. Phys. Lett.</i> , 115, 17B702, 2014.....	46
Figure 1.23 (a) Magnetically dominant HAMR, (b) intermediate HAMR, (c) thermally dominant HAMR, (d) average remanent magnetization for a modeled isolated HAMR transition, and (e) standard deviation of the magnetization from the average remanent magnetization. Courtesy of N. J. Gokemeijer et. al., <i>Appl. Phys. Lett.</i> , 105, 07B905, 2009.	47
Figure 1.24 Schematic illustration of a magneto-optic sensor in the form of an Au/Co/Au structure within the Kretschmann configuration. Courtesy of D. Regatos et. al., <i>Opt. Express</i> , vol. 19, no. 9, 2011.....	49
Figure 1.25 Schematic representation gold nanodisks with and without SiO ₂ layers. Courtesy of J. C. Banthí, <i>Adv. Mater.</i> , vol. 24, no. 10, 2002.	49
Figure 1.26 (a) Schematic representation of an Au/Co/Au multilayer with a PMMA overlayer, (b) PMMA thickness as a function of surface plasmon propagation	

length, and (c) figure of merit $\Delta k_{\text{spp}} \times L_{\text{spp}}$ for the multilayer for various refractive indices of the overlayer. Courtesy of D. Martín-Becerra et. al., Appl. Phys. Lett., 97, 183114, 2010.	51
Figure 1.27 Schematic illustration of a gold/cobalt/gold multilayer with a tilted groove-slit pair. Courtesy of V. V. Temnova et. al., Nature Photon., 4, 2, pp. 107-111, 2010.	52
Figure 2.1 Schematic illustration of a four-layer multilayer with a gold thin-film near a cobalt layer. The red arrow illustrates the primary reflections from the H-G interface. The light blue and blue arrows represent the reflections from the G-D and D-C interface, respectively. The thickness of the gold layer and dielectric layer is d_1 and d_2	56
Figure 2.2 Reflectivity as a function of the angle of incidence for various operation wavelengths of (a) 550 nm, 633 nm and 750 nm, and gold thicknesses of (b) 20 nm, 25 nm and 30 nm. The thickness of the dielectric layer in (b) is 98 nm, 126 nm, and 176 nm, respectively. The operation wavelength in (b) is 633 nm. The refractive index of the dielectric is $n=1.2$	59
Figure 2.3 Intensity enhancement at the cobalt/dielectric interface as a function of gold thickness and dielectric thickness. The refractive index of the dielectric layer is $n = 1.2$. The operation wavelength is 633 nm.	60
Figure 2.4 Electric field intensity profiles of various multilayers with a dielectric thickness of (a) 50 nm, (b) 176 nm, and (c) 300 nm. The thickness of the gold layer is selected as 30 nm. Refractive index of the dielectric layer is $n = 1.2$. The incident angle is 67° . The operation wavelength is 633 nm.	60
Figure 2.5 Electric field intensity profile for a gold thickness of 30 nm and a dielectric thickness of 160 nm. The operation wavelength is 633 nm.....	62
Figure 2.6 Intensity enhancement at the cobalt/dielectric interface as a function of the thickness and refractive index of the dielectric layer. The thickness of the gold layer is different for each multilayer configuration to obtain maximum intensity enhancement. The operation wavelength is 633 nm.....	63
Figure 2.7 Intensity enhancement at the cobalt/dielectric interface as a function of gold thickness and refractive index of the dielectric layer. The thickness of the dielectric layer is different for each multilayer configuration to obtain maximum intensity enhancement. The operation wavelength is 633 nm.....	63

Figure 3.1	Schematic illustration of a three-layer multilayer with a gold thin-film adjacent to a cobalt thin-film. The thickness of the gold layer is d_1	67
Figure 3.2	Real part of the dielectric functions of gold and cobalt as a function of wavelength.....	67
Figure 3.3	Reflectivity as a function of the angle of incidence. h-g-d denotes the High-index/Gold/Dielectric multilayer, and h-g-c denotes the High-index / Gold / Cobalt multilayer. The incident wavelength is 633 nm.....	67
Figure 3.4	Electric field intensity profiles of various layers that laminated on the gold layer. The incident wavelength is 633 nm.....	68
Figure 3.5	Intensity values at the gold-cobalt interface as a function of incident wavelength, gold thickness, and refractive index of the high-index medium. The wave amplitude of the incident wave is selected as 1 V/m.	68
Figure 3.6	Schematic illustration of a five-layer multilayer with a gold thin-film near a cobalt layer. The red arrow illustrates the primary reflections from the H-G interface. The light blue, blue, and dark blue arrows represent the reflections from the G-D, D-G, and G-C interfaces, respectively. The thickness of gold and dielectric layers is d_1 , d_2 , and d_3	70
Figure 3.7	Reflectivity as a function of the angle of incidence for a high-index / gold / dielectric / gold / cobalt multilayer. The thickness of the gold layers is 30 nm, and the dielectric layer is 176 nm.....	70
Figure 3.8	Electric field intensity profiles of various multilayers with a dielectric thickness of (a) 300 nm, (b) 176 nm, and (c) 50 nm. The thickness of the gold layer is selected as 30 nm. Refractive index of the dielectric layer is $n = 1.2$. The operation wavelength is 633 nm.....	71
Figure 3.9	Schematic illustration of the proposed layer in an integrated head in a HAMR system. The proposed plasmonic layer is adjacent to the magnetic head, and it isolates the optical interaction of the other plasmonic layer with the magnetic head.	73
Figure 3.10	Dispersion relation of H-G-M and H-G-D-M multilayers. The thickness of the gold layer (d_1), dielectric layer (d_2), and gold layer (d_3) is selected as 50 nm, 200 nm, and 50 nm, respectively. The refractive index of the high-index layer is selected as 1.5.	76
Figure 3.11	Dispersion relation of H-G-D-G (MIM configuration) and H-G-D-G-M multilayers. The thickness of the gold layer (d_1), dielectric layer (d_2), and gold	

layer (d_3) is selected as 50 nm, 200 nm, and 50 nm, respectively. The refractive index of the high-index layer is selected as 1.5.....	77
Figure 3.12 Electric field intensity gradient profiles in the dielectric layer as a function of (a) the dielectric thickness, (b) gold thickness, (c) incident wavelength, and (d) incident angle. The gold thickness (d_1), and dielectric thickness (d_2), and gold thickness (d_3) is 30 nm, 176 nm, and 30 nm, respectively for (a) and (b). The refractive index of the high-index layer is selected as 1.5.....	78
Figure 3.13 Electric field intensity gradient values as a function of the (a) dielectric thickness (d_2) and gold thickness (d_1), (b) dielectric thickness (d_2) and gold thickness (d_3), (c) refractive indices n_0 and n_2 , and (d) gold thickness (d_1) and incident wavelength.. The thickness of the gold layer (d_1), dielectric layer (d_2), and gold layer (d_3) is selected as 50 nm, 200 nm, and 50 nm, respectively. The refractive index of the high-index layer is selected as 1.5.....	79
Figure 3.14 Internal damping of the H-G-D-G-C multilayer as a function of various system parameters.....	80
Figure 3.15 Schematic illustration of a three-layer multilayer with a gold thin-film that is laminated on a high-index layer. The thickness of the gold layer is d_1	81
Figure 3.16 Reflectivity as a function of the incident angle for a three layer H-G-D and five layer H-G-D-G-C configuration.	82
Figure 3.17 (a) Reflectivity as a function of the refractive index of the high-index layer, and (b) electric field intensity profile for $n=1.655$	82
Figure 3.18 Reflectivity as a function of the dielectric index, and (b) electric field intensity profile for $n=1.09$	82
Figure 3.19 Reflectivity as a function of the incident wavelength, and (b) electric field intensity profile for $\lambda=1200$ nm.....	83
Figure 4.1 A schematic illustration of a PSIM. Light rays that enter the PSIM are reflected at different angles from the parabolic side walls at either sides to the focal point of the PSIM. Courtesy of Challener et.al., Optics Express, 13, 18 (2005)....	90
Figure 4.2 Images of fabricated PSIMs with $Al_2O_3/Ta_2O_5/Al_2O_3$ dielectric layers that sit on a ceramic substrate. (a) Light is incident on the two coupling gratings that are fabricated at the upper region of the PSIM, and (b) A three-layer PSIM with a high index core that is sandwiched between lower index claddings is shown. Courtesy of Rottmayer et.al., IEEE Transactions on Magnetics, 42, 10 (2006), and Challener et.al., Optics Express, 13, 18 (2005).....	90

Figure 4.3 Schematic illustration of a planar dielectric waveguide with a high index core n_{co} laminated between lower index claddings n_{cl} that is etched into a planar mirror.	92
Figure 4.4 A TE plane wave is incident at an oblique incidence on the core and cladding regions of a symmetric slab waveguide. The relative permittivity of the core is ϵ_{r0} and that of the cladding is ϵ_{r1} . The thickness of the core region is d	92
Figure 4.5 Normalized electric field intensity distribution $ E(x=0,y=0,z) ^2$ in a symmetric slab waveguide for various refractive indices of the core n_{co} . The refractive index of the cladding is $n_{cl}=1.4$. The thickness of the core is $d = 105$ nm.	95
Figure 4.6 Normalized electric field intensity distribution $ E(x=0,y=0,z) ^2$ in a symmetric slab waveguide for various refractive indices of the core n_{co} . The refractive index of the cladding is $n_{cl}=1$. The thickness of the core is $d = 105$ nm.	95
Figure 4.7 Normalized electric field intensity distribution $ E(x=0,y=0,z) ^2$ in a symmetric slab waveguide for various refractive indices of the core n_{co} . The refractive index of the cladding is $n_{cl}=1$. The thickness of the core is $d = 70$ nm.	95
Figure 4.8 Normalized electric field intensity distribution $ E(x=0,y=0,z) ^2$ in a symmetric slab waveguide for various core thicknesses $d = 70$ nm and $d = 210$ nm. The refractive indices of the core is $n_{co} = 4$ and that of the cladding is $n_{cl} = 1$. The right boundary of the core region is varied from $x = 70$ nm to $x = 210$ nm. The left boundary is kept constant at $x = 0$ nm.	96
Figure 4.9 Full-width half maximum of electric field intensity $ E(x=0,y=0,z) ^2$ profile as a function of the core thickness for $n_{co} = 1.5, 2, 2.5,$ and 3 . The index of the cladding is $n_{cl} = 1$	97
Figure 4.10 Full-width half maximum of electric field intensity $ E(x=0,y=0,z) ^2$ profile as a function of the core index n_{co} for $d = 20, 25, 30,$ and 35 nm. The index of the cladding is $n_{cl} = 1$	97
Figure 4.11 The plasmonic planar solid immersion mirror (plasmonic PSIM).	98
Figure 4.12 Plasmonic PSIM designs with various numerical apertures. The dielectric index of the superstrate and substrate is selected as $n_0=2.5,$ and $n_2=1,$ respectively. The incident wavelength is 633 nm.	100
Figure 4.13 A closer view of optical spots for various numerical apertures. (a), (b) and (c) represent the electric field intensity distributions along the $z=0$ cut-plane	

$ \mathbf{E}(x,y,z=0) $. The dielectric index of the superstrate and substrate is selected as $n_0=2.5$, and $n_2=1$, respectively. The incident wavelength is 633 nm.....	101
Figure 4.14 Surface plasmon wavelength in an dielectric/metal configuration as a function of the refractive index of the dielectric medium n_2 . The incident wavelength is $\lambda = 633$ nm.....	101
Figure 4.15 Dispersion relations of surface plasmons at a metal/dielectric interface as a function of various dielectric indices $n_2 = 1, 1.5$, and 2	102
Figure 4.16 Dispersion relations of plasmonic PSIMs with various substrate and superstates indices. The light line and the light line in the substrate is given as a reference. The dispersion relation for a single metal/dielectric interface is also provided. (a) $n_0 = 2, n_2 = 1.7$, (b) $n_0 = 2.6, n_2 = 2.1$, (c) $n_0 = 2.8, n_2 = 2.2$, and (d) $n_0 = 3.2, n_2 = 2.4$. The incident wavelength is 633 nm.	103
Figure 4.17 Plasmonic PSIMs with various substrate and superstates indices. (a) $n_0 = 2, n_2 = 1.7$, (b) $n_0 = 2.6, n_2 = 2.1$, (c) $n_0 = 2.8, n_2 = 2.2$, and (d) $n_0 = 3.2, n_2 = 2.4$. The incident wavelength is 633 nm.	104
Figure 4.18 Plasmonic PSIMs in the form of metal/insulator/metal (MIM) configurations. (a) Schematic representation of the MIM geometry, (b) $ \mathbf{E}(x,y,z = 0) $, (c) $ \mathbf{E}(x=0,y,z) $, and (d) $ \mathbf{E}(x,y=0,z) $. Refractive index of the superstrate and the dielectric interlayer is selected as 3.2 and 1.2, respectively. The incident wavelength is 633 nm.	105
Figure 4.19 Plasmonic PSIMs (a) before lift-off, and (b) after lift-off. The height and width of the structures is $8.7 \mu\text{m}$ and $6 \mu\text{m}$, respectively.	106
Figure 4.20 NSOM and simulation results of PSIMs. (a) 2D view of an NSOM image of a single PSIM, (b) simulation of a single PSIM, (c) 2D view of an array of PSIMs, and (d) 3D view of a single PSIM.	107
Figure 4.21 Intensity profiles along the x-direction and y-direction of the PSIM.....	107
Figure 5.1 Schematic illustration of the (a) Kretschmann configuration, (b) a glass-gold-air-cobalt configuration, and (c) a glass-gold-sensing-dielectric-cobalt configuration.....	110
Figure 5.2 Reflectivity curve of (a) the glass-metal-sensing configuration, and (b) glass-gold-sensing-cobalt multilayer. The thickness of the gold and sensing layer is selected as 50 nm and 100 nm, respectively. The permittivity of the glass and the sensing layer is selected as 2.25 and 1.8, respectively.	116

Figure 5.3 Electric field intensity profiles $ \vec{E}(x = 0, y = 0, z) ^2$ of metal-gold-sensing and metal-gold-sensing-cobalt multilayers.....	116
Figure 5.4 Transfer functions $ r_{ms} $, $ r_{msc} $, $ r_{msdc} $ of gold-sensing, gold-sensing-cobalt, and gold-sensing-dielectric-cobalt multilayers, respectively.....	117
Figure 5.5 Two-dimensional dispersion plot of the sensing-dielectric-cobalt multilayer as a function of the dielectric thickness and permittivity of the sensing layer. White-dotted regions denote the reflectivity values for $ r_{sdc} \approx 0$ of the multilayer.	118
Figure 5.6 Reflectivity curve of (a) prism-gold-sensing, (b) prism-gold-sensing-dielectric multilayer and (c) prism-gold-sensing-dielectric-cobalt multilayer. The thickness of the gold, sensing, and dielectric layer is selected as 50 nm, 100 nm, and 40 nm, respectively. The relative permittivity of the prism, sensing, and dielectric layers is selected as 4, 1.8, and 1, respectively.	119
Figure 5.7 Electric field intensity profiles $ \vec{E}(x = 0, y = 0, z) ^2$ of glass-gold-sensing-dielectric-cobalt multilayers for glass permittivities of 2.25 and 4.	120

LIST OF SYMBOLS

A_0	Field amplitude in Region 0 of the waveguide
B_0	Field amplitude in Region 0 of the waveguide
c	Speed of light in vacuum
d	Thickness of the core layer of the waveguide
$d(\cdot)$	Differential operator
d_0	Thickness of layer 0
d_1	Thickness of layer 1
d_2	Thickness of layer 2
d_3	Thickness of layer 3
d_4	Thickness of layer 4
ϵ_1	Relative permittivity of the first layer
ϵ_2	Relative permittivity of the second layer
ϵ_j	Relative permittivity of medium j
ϵ_m	Relative permittivity of the metal layer
ϵ_s	Relative permittivity of the sensing layer
E_{-1}	Field amplitude of evanescent wave in Region -1
E_{+1}	Field amplitude of evanescent wave in Region 1
\vec{E}^i	Electric field vector
E_m^i	Incident field amplitude in layer m
E_l^i	Incident field amplitude in layer l
\vec{E}^s	Scattered field
\vec{E}^t	Total field
$ \vec{E}^i $	Magnitude of the electric field in the dielectric layer along the down track direction
\vec{E}_1^\perp	Normal component of the electric field in medium 1
\vec{E}_2^\perp	Normal component of the electric field in medium 2
i	Index number
R	Reflection coefficient of multilayer

k_B	Boltzmann's constant
k_{mz}	Normal component of the wavevector in layer m
k_{sz}	Normal component of the wavevector in layer s .
K_u	Anisotropy of magnetic particles
k_x	Tangential component of wavevector
k_{spp}	Surface plasmon wavevector
k_z	Normal component of wavevector
k_{z0}	Transverse wave number in layer 0
k_{z1}	Transverse wave number in layer 1
k_{z2}	Transverse wave number in layer 2
k_{z3}	Transverse wave number in layer 3
k_{z4}	Transverse wave number in layer 4
n_{cl}	Refractive index of the cladding layer
n_{co}	Refractive index of the core layer
$\tilde{R}_{2,3}$	Generalized reflection coefficient that incorporates reflections from the quartz layer
r_{ms}	Reflectivity of metal-sensing bilayer
r_{msc}	Transfer function of metal-sensing-cobalt layer
r_{msdc}	Transfer function of metal-sensing-dielectric-cobalt layer
r_{pm}	Reflectivity of glass-metal bilayer
r_{pms}	Transfer function of the glass-metal-sensing layer
r_{pmsc}	Transfer function of glass-metal-sensing-cobalt layer
r_{pmsdc}	Transfer function of glass-metal-sensing-dielectric-cobalt layer
R_{12}	Reflection coefficient between layer 1 and layer 2
R_{34}	Reflection coefficient between layer 3 and layer 4
T	Ambient temperature
TE	Transverse electric
V	Volume of magnetic particles
$\overline{V}_{(l+1)l}$	Propagation matrix
ω	Angular frequency
θ_c	Critical angle of total internal reflection
λ	Vacuum wavelength

λ_{spp}

Surface plasmon wavelength

TABLE OF ABBREVIATIONS

ATR	Attenuated Total Reflection
FDTD	Finite-Difference Time Domain
FVM	Finite Volume Method
FWHM	Full-Width Half Maximum
HAMR	Heat-Assisted Magnetic Recording
LSPR	Localized Surface Plasmon Resonance
MOSPR	Magneto-Optic Surface Plasmon Resonance
NSOM	Near-Field Scanning Optical Microscope
PMMA	Poly(methyl methacrylate)
PSIL	Planar Solid Immersion Lens
PSIM	Planar Solid Immersion Mirror
SPAH	Surface Plasmon Assisted HAMR
SPR	Surface Plasmon Resonance
TMOKE	Transverse Magneto-Optic Kerr Effect

1 INTRODUCTION

1.1 Definition of the Problem, Importance, and Original Value

Magnetic information storage technology has been used to store digital information for over 50 years. It is one of the main technologies that has driven technological progress in information technology. Many government and private sector transactions, as well as social and economic activities were previously completed on paper. Many of these activities are now performed using computers, and the resulting data is stored on magnetic storage systems. The amount of information produced has been rapidly growing with advances in information technology and the internet. A large amount of information, which is produced as a result of everyday activities, is stored on magnetic storage systems. Some examples include banking, the health sector, transportation, the finance sector, university research, communication (e-mail), entertainment (music, movies, computer games) and government activities. There may be serious consequences to any of these sectors if there is a slowdown in the growth in magnetic information storage devices.

The magnetic hard disk drive industry depends on continually increasing areal density, which is a measure of the amount of data that can fit to a disk drive. The industry is observing a major slowdown in the increase in areal density as it approaches 1 Tb/inch². Recent studies suggest that conventional magnetic recording is limited around 1 Tb/inch². This metric has been the focus of the hard disk drive industry, since it determines the storage capability of enterprise and personal computer systems, as well as portable electronic devices. Longitudinal recording technology has been employed in hard disk drives since the beginning of the magnetic storage technology [1,2]. In longitudinal recording, areal density growth has been achieved by continuously scaling down the bit dimensions [3]. Unfortunately, longitudinal recording reached its limits for data storage around 100 Gb/inch² due to the superparamagnetic limit [4,5]. The superparamagnetic limit became an issue as the grain volume of the recording magnetic

medium was reduced in order to control media noise for high areal density recording. A major challenge in HAMR is the superparamagnetic limit of magnetic particles. The thermal stability of the magnetic particles in magnetic disk drives is determined by the anisotropy K_u and volume V of the magnetic particles. There are materials available in nature with high anisotropy constants, however, the required magnetic fields to switch their magnetization is higher than the available head-fields. As the areal density increases, the volume of the magnetic particles decreases. To preserve the thermal stability of the magnetic particles, their anisotropy needs to be increased. Namely, there is a trade-off between anisotropy and particle volume. The ambient temperature stability factor relation determines this trade-off in mathematical means:

$$\frac{K_u V}{k_B T} \geq 70 \quad (1.1)$$

where k_B is the Boltzmann's constant and T is the ambient temperature. Thus, utilizing from materials with high anisotropy, the lifetime of the encoded bits can extend to tens of years. A higher stability factor certainly means a longer lifetime for magnetic storage devices. There are materials available in nature with high anisotropy constants, however, the required head-fields to switch their magnetization is very high.

Due to this fundamental limitation, the data storage sector switched to perpendicular recording. Since 2007, hard disk drive companies have been utilizing perpendicular recording instead of longitudinal recording to extend the areal density limits. Perpendicular recording can extend areal density limits to 1 Tb/inch². The timeline of areal density for both laboratory demonstrations and products are illustrated in Figure 1.1, which illustrates when the switch from longitudinal to perpendicular recording occurred. The blue line represents the 100 Gbit/inch² where the switch from longitudinal recording to perpendicular recording occurred. The red line indicates the expected limits of the state-of-the-art perpendicular recording.

Since storage limitations will threaten the future of information technology and related economic growth, fundamental research in this area is essential. HAMR [6-13] is a potential technique to extend the physical limits of conventional magnetic recording in hard disk drives beyond 1 Tbit/in.². The main difference between state-of-art

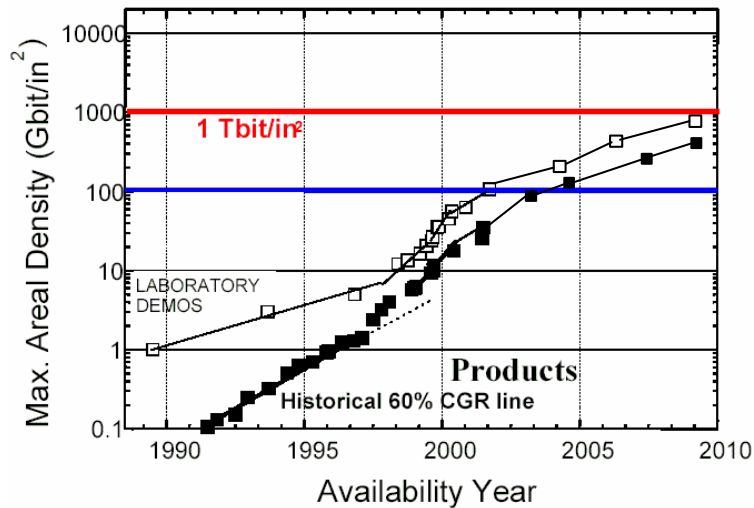


Figure 1.1 Areal density in magnetic storage devices as a function of time. The curve with empty squares represents demonstrations in research laboratories and the curve with filled squares represents the areal density of products. The blue line represents the 100 Gbit/inch² where the switch from longitudinal recording to perpendicular recording occurred. The red line indicates the expected limits of the state-of-the-art perpendicular recording.

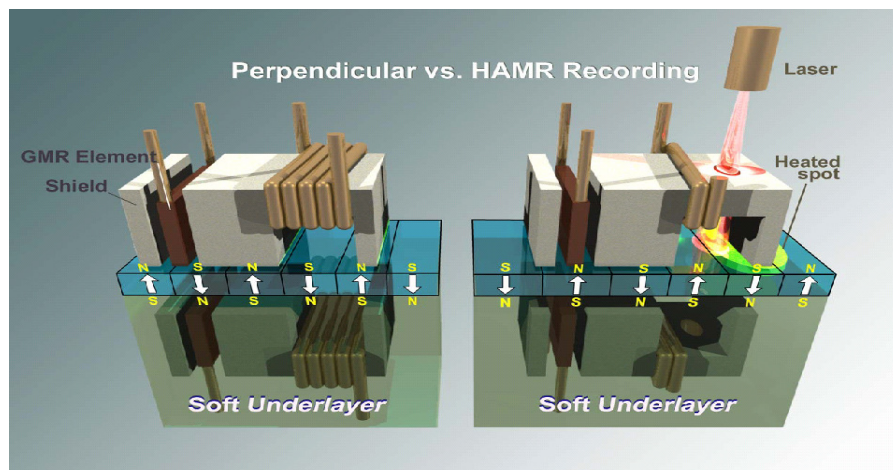


Figure 1.2 Schematic comparison of perpendicular recording and heat-assisted magnetic recording.

recording and a HAMR system is that in HAMR an optical spot is utilized to heat the recording medium as illustrated in Figure 1.2. Magnetic recording in HAMR is executed as follows: The optical spot reduces the coercive field of the magnetic particles to nearly zero below the head field by localized heating of the magnetic

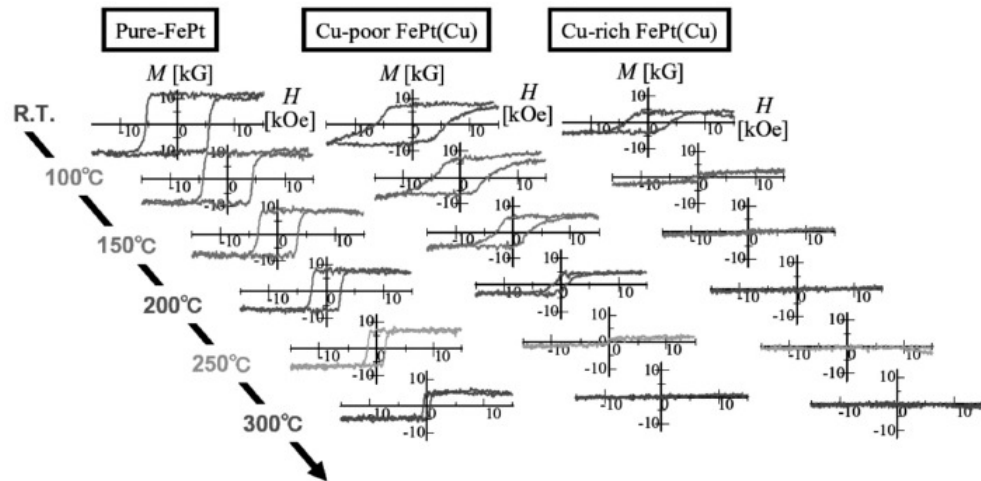


Figure 1.3 Hysteresis loops for various material compositions. As the temperature increases the area that is enclosed by the M-H curves reduces. Courtesy of Ikemoto et.al., IEEE Trans. Magn., 44, 11, (2008).

particles. The recording medium that is utilized to write magnetic information is ferromagnetic, therefore it exhibits hysteresis. The hysteresis loops as shown in Figure 1.3 are modified during the heating process such that the area enclosed by the M-H curves becomes smaller, thus the value of the coercive field decreases [14]. At an elevated temperature, the head field remains available until the magnetic grains are cooled back to the ambient temperature at ~1 nanosecond to achieve necessary data

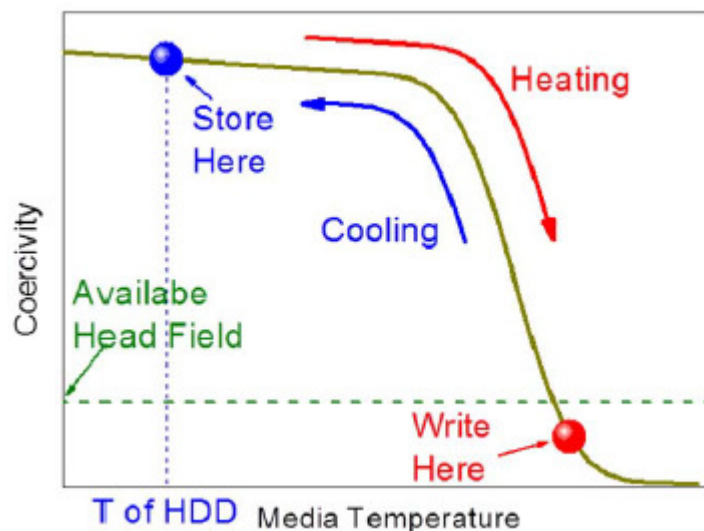


Figure 1.4 Schematic comparison of the HAMR heating and cooling process. The coercivity value is reduced below the head field value to enable recording. Courtesy of Wu. et. al., IEEE Trans. Magn., 49, 2, (2013).

rates, and 1 bit of magnetic information is thereby written. A schematic representation of the heating and cooling process is illustrated in Figure 1.4. Lastly, the slider moves the magnetic head to the adjacent grain in the cross-track or down-track direction to write magnetic information.

1.2 Literature Survey

1.2.1 HAMR Head Design and Recording Demonstrations

Literature studies in this section present a detailed summary of different head designs, discuss the effect of various HAMR components on the performance of the heads, suggest solutions to enhance the transducer performance, and present specific recording demonstrations. In this section, a step-by-step approach is followed that begins with the design of isolated nanotransducers and takes a step forward by adding to nanotransducer designs necessary components that build up a real HAMR head. At the end of this section, three recording demonstrations of HAMR heads are presented.

Furthermore, the relevance of this thesis with the literature studies and the added-value of this thesis to the literature studies are presented. It may be useful for the reader to briefly mention the relevance of the thesis in advance, at the beginning of this section. A more detailed discussion has been carried out within the literature survey: Chapter 2 of this thesis contributes to the literature by carrying out a parametric study to minimize radiation loss, internal damping, and load-induced losses in an integrated head. It is shown that a higher intensity enhancement can be obtained by minimizing radiative and load-induced losses through adjusting layer thicknesses in multilayer configurations.

In the literature, a magnetic head and a plasmonic nanotransducer in a HAMR head are integrated with each other, which reduces the intensity enhancement of the plasmonic nanotransducer due to various losses. Chapter 2 of this thesis investigates these losses. Chapter 3 demonstrates a specific approach to isolate the magnetic head from the plasmonic nanotransducer. A gold layer is introduced near a magnetic layer in

an integrated head, which is represented by a multilayer configuration. Thus, a higher intensity enhancement from the nanotransducer can be obtained.

In Chapter 2 and Chapter 3, a HAMR head is modeled as a multilayer configuration and is investigated in various aspects. Chapter 4 treats a HAMR head as a parabolic structure and investigates it numerically and experimentally. Finite-element method simulations and near-field scanning electron microscopy experiments reveal focused spot sizes from the plasmonic transducer as small as $1/60$ of the incident wavelength, which is about $1/4$ of the incident wavelength in the current literature.

Chapter 5 leaves the HAMR concept to investigate the underlying reasons of the damped plasmon resonances in multilayered SPR sensors with thick lossy samples, and presents specific sensor configurations that recover the plasmon resonances in the presence of the samples. In the literature, SPR sensors with lossless samples and with thin and lossy samples are present. On the other hand, thick and lossy samples degrade the performance of SPR sensors. Therefore, specific sensor configurations are presented that recover the performance of SPR sensors.

Designing plasmonic nanotransducers that can produce intense optical spots beyond the diffraction-limit and that have high transmission efficiency has been a primary goal to achieve by the magnet-optic recording community [15-17]. In order to advance the areal density of hard drives beyond 1 Tbit/in^2 , various nanotransducer configurations are proposed. In one of the studies, three types of ridge apertures; a bow-tie aperture, a half bow-tie aperture, and a C-aperture is investigated to produce optical spots beyond the diffraction limit for their utilization as a near-field nanotransducer for HAMR [18]. As a result, optical spots with FWHM dimensions of $37.7 \times 13.6 \text{ nm}$ and $43.2 \times 16.3 \text{ nm}$ are produced by the bow-tie and half bow-tie apertures. In addition, circular grooves are considered around a bow-tie aperture to increase its transmission efficiency. The transmission efficiency of the apertures is enhanced due to surface plasmons propagating along the grooves to the gap of the apertures.

In another study, a double grating structure with a metallic slit at the center of the grating is placed at the end of a slab waveguide and this configuration is proposed as a

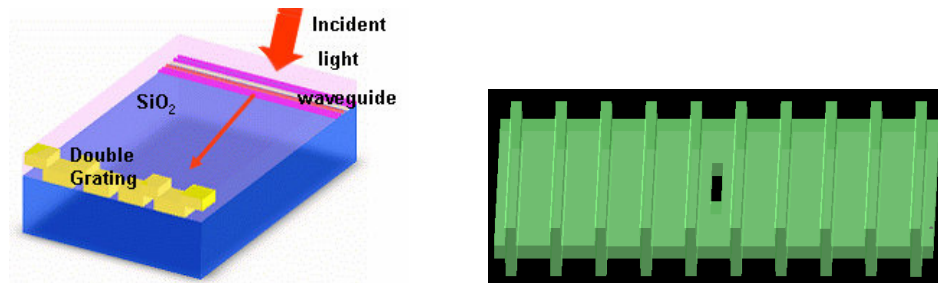


Figure 1.5 (a) A double grating structure that is placed at the end of a waveguide, and (b) the metallic slit at the center of the grating structure. Courtesy of D.-S. Lim et. al., Asia Pacific Magnetic Recording Conference, pp. 1-2, 2006.

HAMR optical head, as illustrated in Figure 1.5 [19]. By matching the wavevector of surface plasmons to the grating vector of the double grating structure a higher optical throughput is obtained through the metallic slit.

A parametric study is performed to study the geometric properties of various nano-apertures and the polarization of the incident light on the transmission efficiency of the nano-apertures. The recording media is chosen as a patterned FePt media. C-shaped and I-shaped apertures provided higher near-field intensity and a smaller optical spot [20].

In HAMR heads, incident laser light is usually confined by a primary optical structure, which then focuses the confined light onto a plasmonic nanotransducer for further confinement. The coupling efficiency between the primary structure and the plasmonic nanotransducer depends on various parameters and specifies the efficiency of the nanotransducer. In a recent study, this issue is investigated as the evanescent coupling between a dielectric and a plasmonic waveguide in the context of HAMR applications [21]. A system with a dielectric waveguide near a nanotransducer is considered. In this system, if there is a mismatch in the mode indices, a confined mode in the dielectric waveguide will not be able to evanescently couple to the nanotransducer. To reduce this mismatch, a plasmonic waveguide is introduced between the dielectric waveguide and the near-field transducer. A coupling grating at the beginning of the dielectric waveguide is utilized to couple incident light to the dielectric waveguide, as depicted in Figure 1.6(a). The specific distance between the dielectric

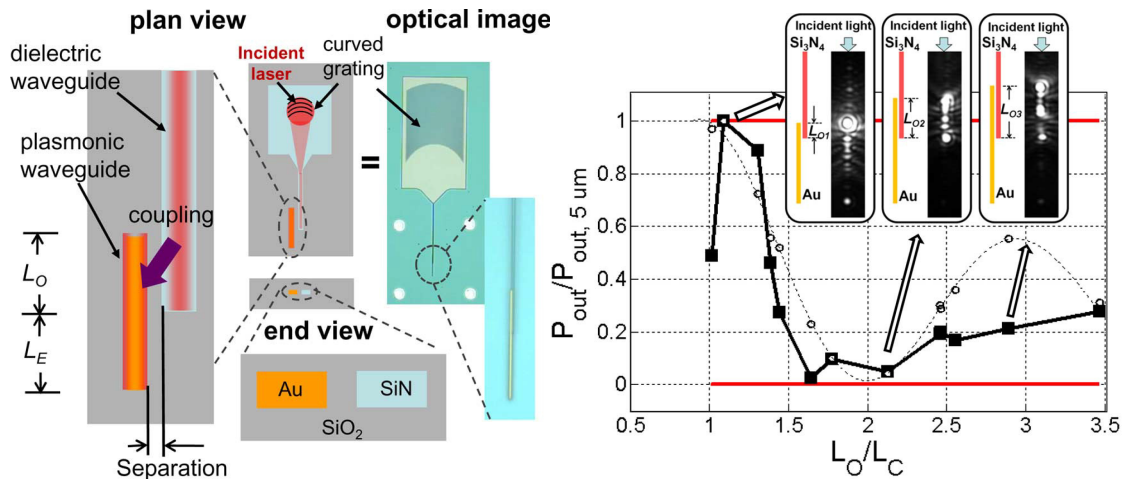


Figure 1.6 (a) Schematic representation of the plan view and optical image of the dielectric and plasmonic waveguide, and (b) experimental realization of the coupling phenomena. Courtesy of Y. Kong et. al., IEEE Trans. Magn, vol. 47, pp. 2364-2367, 2011.

and plasmonic waveguide, which is the coupling length, allows the confined mode in the dielectric waveguide to evanescently couple to the plasmonic waveguide. Thus, the confined mode can couple to the plasmonic waveguide. This two-step method helps to efficiently couple a dielectric waveguide and a near-field nanotransducer. As shown in Figure 1.6(b), light that scatters out at the end of the plasmonic waveguide signifies that two waveguides can couple efficiently. Obviously, the intensity of the scattered light varies with the overlap length between the waveguides.

A planar solid immersion mirror (PSIM) with high throughput is suggested that can produce optical spots with dimensions that are less than quarter of the incident wavelength, as illustrated in Figure 1.7(a) [22]. The basic operation principle of the PSIM can be summarized as follows: A TE polarized beam is incident on a dual offset grating coupler that is at the opening of the PSIM. The offset between the gratings, which is half a period, creates a π -phase shift between the TE modes at the either side of the PSIM. Light rays that reflect at the parabolic edges of the PSIM, meet at the focus of the PSIM. Characterization of the optical spot by a near-field scanning optical microscope (NSOM) has demonstrated an optical spot size of ~ 90 nm, as presented in Figure 1.7(b).

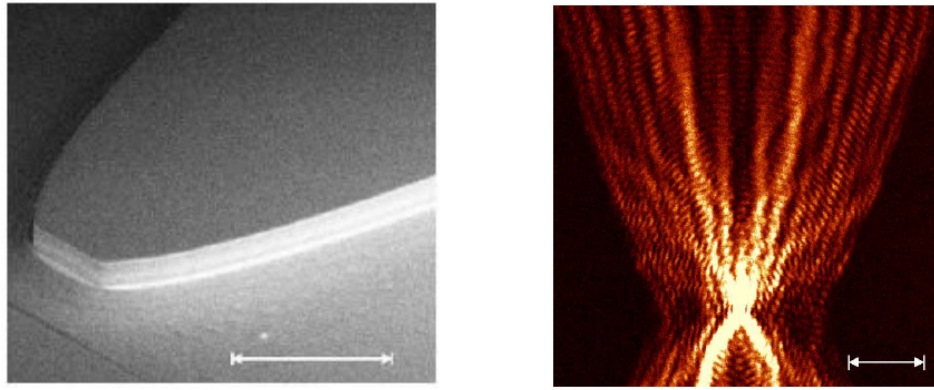


Figure 1.7 (a) A fabricated PSIM on a ceramic substrate and (b) the implemented micro-optical structure with lithographic techniques, (c) NSOM image of a focused optical spot by the PSIM. Courtesy of W. A. Challener et. al., vol. 13, no. 18, pp. 7189-7197, 2005.

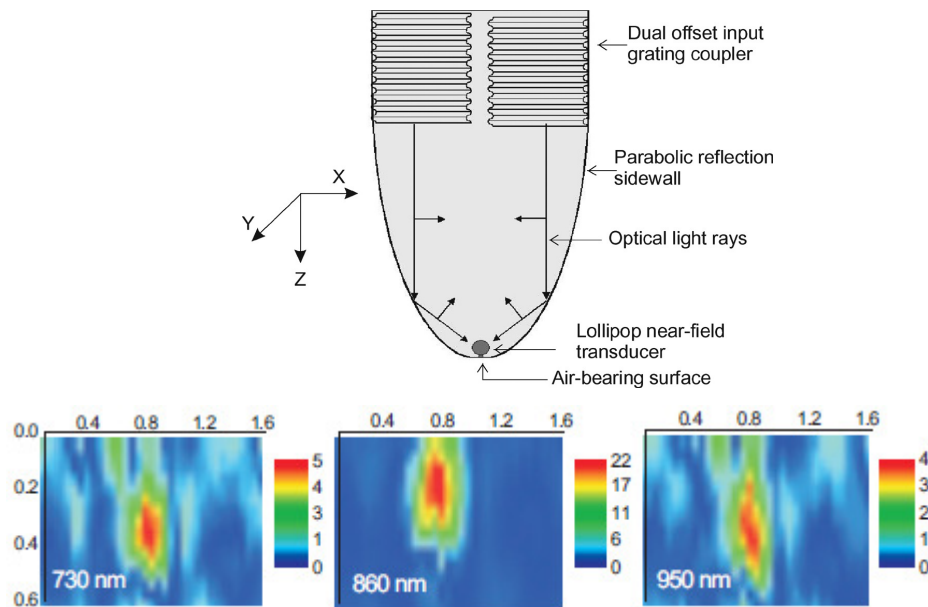


Figure 1.8 (a) Schematic representation of the PSIM with a near-field nanotransducer at its focus, and (b) photothermal images at various operation wavelengths. Courtesy of C. Peng et. al., IEEE Trans. Magn, vol. 48, pp. 1801-1806, 2012.

As a follow-up to the above study, a lollipop-shaped near-field nanotransducer with a rectangular protruded peg is placed at the focus of PSIM to further confine the incident light at the focus of the PSIM, as illustrated in Figure 1.8 [23]. In order to excite localized surface plasmons on the vertically-oriented peg, a vertically-oriented field component is required. For the nanotransducer, a pump-probe thermal measurement is utilized. The hot spots clearly show an evidence for a plasmonic

enhancement, as shown in Figure 1.8(b). An experimental sweep for various operation wavelengths resulted in two peaks of the probe signal at 710 nm and 870 nm, which correspond for two surface plasmon modes.

As demonstrated in the previous studies in this section, various transducers are designed without considering the effects of the recording media. In a HAMR setup there are various magnetic components in the vicinity of the nanotransducer that affect the performance of the nanotransducer. The recording media that is separated by an air bearing surface from the nanotransducer is one of those components. The following studies take into account the recording medium and examine the absorptive properties on the performance of the nanotransducers.

In the presence of a recording layer, the protruded peg of the near-field nanotransducer is optimized to yield a higher efficiency [24]. The near-field transducer is designed as rectangular body with a protruded peg, as illustrated in Figure 1.8(a). An efficiency measure is defined as the fraction of total optical power propagating in the PSIM that is dissipated within a 50 x 50 nm region in the recording layer. Various parameters such as the transducer width, transducer height, transducer-to-waveguide core spacing and core thickness are studied and optimal parameters are specified numerically. Using the optimal parameters, a confined spot of 56 x 60 nm is obtained in the recording medium, as shown in Figure 1.9(b). In addition, a peak intensity is obtained that is 16.5 times greater than a PSIM focusing field without a recording medium. In order to gain a physical insight on the optimal size of the transducer, the PSIM is modeled as a strip waveguide and the effective wavelength corresponding to the fundamental waveguide mode is specified. It is found that the optimal height of the transducer is half of the effective wavelength. Therefore it is concluded that the transducer behaves as a half-wave receiving antenna.

The performance of a lollipop near-field transducer that is placed in PSIM is assessed on a patterned FePt media and a continuous thin-film by the finite-difference time domain (FDTD) method, as demonstrated in Figure 1.10 [25]. For the patterned media, an areal density of ~ 1 Tbit/inch² is demonstrated. The patterned media provided a better concentrated optical spot than the continuous media. A peak value is obtained

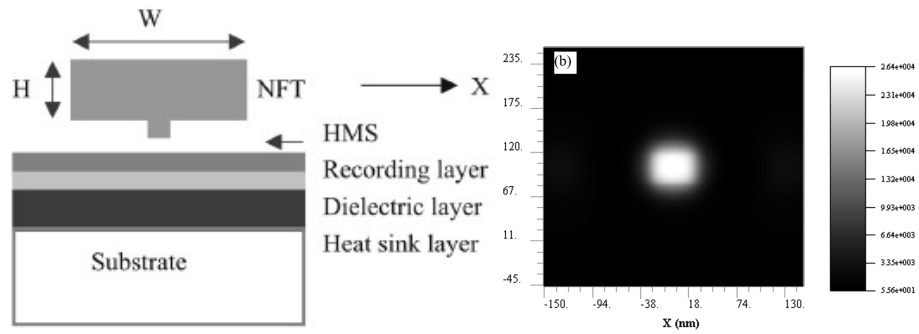


Figure 1.9 Schematic illustration of the near-field transducer near a recording medium. Courtesy of C. Peng, Appl. Phys. Lett, vol. 112, 043108, 2012.

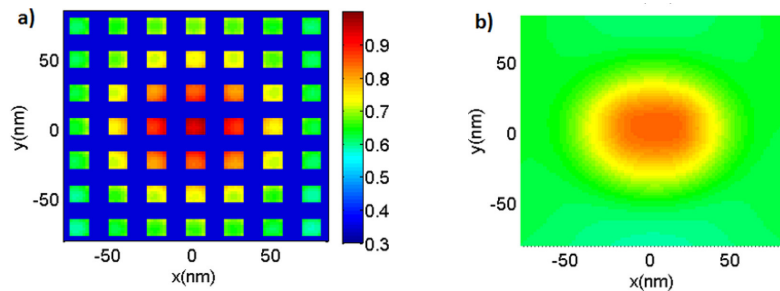


Figure 1.10 Normalized absorption profile for (a) A 12 x 12 x 12 nm bit patterned FePt media and (b) a continuous FePt media. Courtesy of A. Ghoreyshi et. al., J. Appl. Phys., vol. 115, 17B719, 2014.

for the absorbed power by the patterned FePt media that is about 5 times larger than that the peak power that is absorbed by the continuous media.

A recent study thoroughly investigates the transducer efficiency of C-apertures and lollipop nanotransducers with and without the recording media, as illustrated in Figure 1.11(a) [26]. Intensity enhancement of the nanotransducers is obtained near the nanotransducers. For both C-apertures and lollipop nanotransducers it is specified that the longitudinal component of the electric field, E_z , is responsible for a high field enhancement, since the longitudinal component is the one that can excite surface plasmons on the peg of the nanotransducer. As shown in Figure 1.11(b) and Figure 1.11(c), a specific field enhancement is observed in the vicinity of the transducer in the absence of the recording media, and in the air gap that separates the recording media and the nanotransducer, respectively. As depicted in Figure 1.11(c), the intensity distribution in the air gap is efficiently coupled to the recording medium. Within the recording medium, a substantially lower field enhancement is obtained, as depicted by

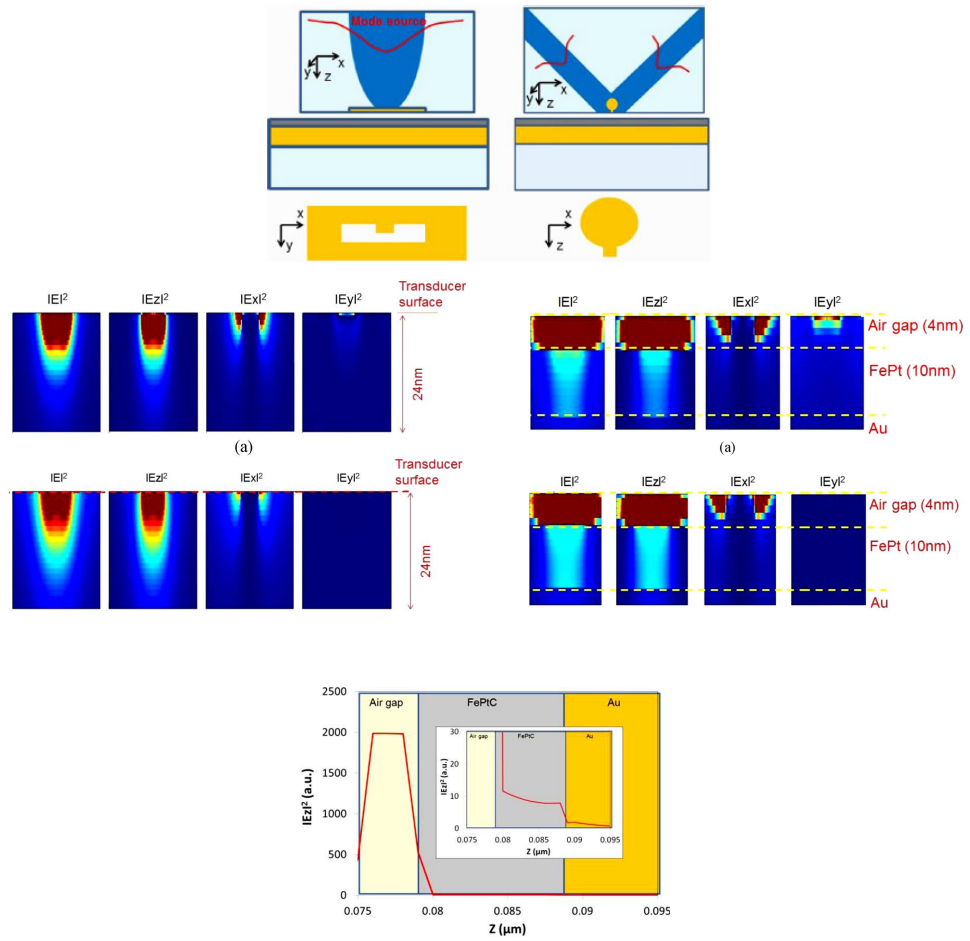


Figure 1.11 Electric field intensity distributions of the (a) C-aperture nanotransducer and the lollipop nanotransducer without the recording media, (b) with the recording media, and (c) electric field profiles in the presence of the recording media. Courtesy of B. Xu et. al., IEEE Trans. Magn., vol. 49, pp. 3580-3583, 2013.

the intensity profiles in Figure 1.11(d). This lower enhancement is due to the very low ratio between the relative permittivities of air and FePt, which is 1/162. This results in a very low ratio between the normal components of the electric field across the air/FePT interface. The main reason that limits the transducer efficiency is this low ratio between the permittivities.

To evaluate the performance of the whole system, the dissipated power by reflection and absorption is also investigated. The highest portion of dissipated power is specified to be due to the back reflection of the laser light. The absorption by the transducer and the FePt layer are specified as the other main loss mechanisms. In order to reduce the reflection loss, an additional gold layer is laminated below the recording layer so that

the distance between the gold layer and the transducer can be adjusted to obtain a π -phase difference between the incident and reflected light at the nanotransducer. The π -phase difference results in a destructive interference of the incident and reflected light. As a result, reflection loss due to the back reflected light is eliminated.

In the above study, a bright solution has been proposed to reduce the reflection loss by adding a gold layer below the FePtC media. The gold layer is added to tune the amount of back reflection from the Air/FePtC/Au multilayer. Chapter 3 of this thesis demonstrates a similar approach to isolate a magnetic head from a plasmonic nanotransducer. A gold layer is added near a magnetic layer in an integrated head, which is represented by a multilayer configuration. Thus the back reflected light from the multilayer is increased. The back reflected light interacts with the nanotransducer to yield a higher intensity enhancement from the nanotransducer. In addition, the nanotransducer is isolated from the absorptive effects of the recording medium.

Another study investigates the effect of a FePt medium on the resonant behavior of C-apertures [27]. Transmission spectra of the apertures are simulated with and without the medium and for various medium thicknesses. As the medium thickness increased, a blue shift in the resonant wavelength and a weaker resonance is observed. This shift and weakening occurs because the light reflected from the recording medium changes the surface charge distribution on the aperture. Since the amount of reflected light varies with varying medium thickness, a shift is observed in the resonant wavelength for different medium thicknesses. To recover the weak resonance in the presence of the recording medium, the arm length of the C-aperture is optimized.

In another study, a dielectric tapered waveguide is designed with the aim to deliver a highly focused optical spot for HAMR applications [28]. In the first design, a rib waveguide is placed on top of a traditional waveguide to better confine the optical spot laterally. In the second tapered waveguide, three traditional waveguides with different dimensions are overlapped on top of one another. The designed waveguides produced free space optical spots with dimensions down to $0.009 \mu\text{m}^2$, which are smaller than that of traditional tapered waveguides, which is $0.011 \mu\text{m}^2$. Optical efficiencies of the dielectric tapered waveguides and various plasmonic nanotransducers are also compared. A higher efficiency is obtained for the dielectric waveguides. This is

due to the lesser heating of the all-dielectric waveguides compared to the metallic nanotransducers.

A metallic slit aperture is designed as an optical head for HAMR, which has neighboring subwavelength rectangular holes at both sides of the metallic slit, as illustrated in Figure 1.12 [29]. The rectangular holes are utilized to further reduce the size of the optical spot in the thickness direction and to increase the intensity of the optical spot in the recording medium. Via this design, a subwavelength optical spot with FWHM dimensions of $82 \times 46 \text{ nm}^2$ and with a plasmonic enhancement of 4.86 is obtained as shown in Figure 1.12. The dimensions of the optical spot are found to be dependent on the sizes of the rectangular holes and their distance to the metallic slit. Furthermore, a plasmon waveguide is coupled to this configuration, and an optical head with a coupling efficiency to the recording medium of % 5.6 is obtained.

A group of the above studies [16-29] have profoundly investigated various transducer designs and their operation with the recording medium. It may have called the attention of the reader that in these studies the magnetic head is not included in the investigations. In fact, in realized HAMR systems in the literature [32, 33] the nanotransducer is integrated with the magnetic head to perform the writing process. In the presence of the magnetic head, one of the

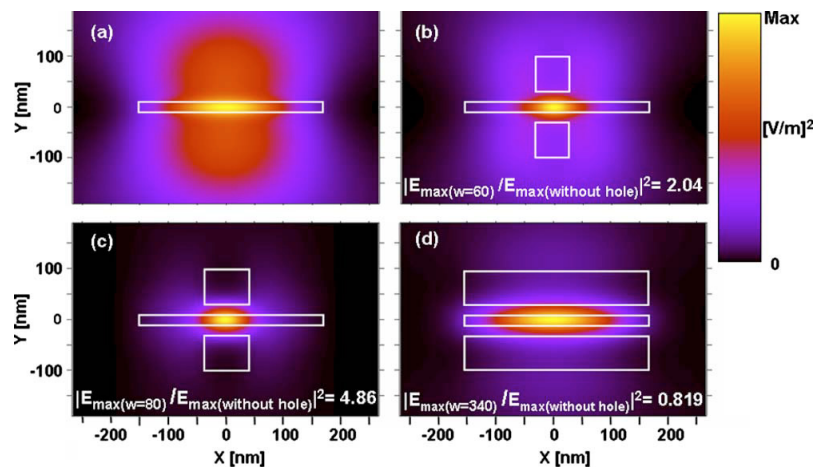


Figure 1.12 (a) Intensity distributions at the top surface of the cobalt layer with various slit and rectangular holes dimensions. The cobalt layer is placed 15 nm below the bottom surface of the transducer, and (b) the gold transducer that is coupled with a plasmonic waveguide. Courtesy of S. Omodani et. al., J. Appl. Phys., vol. 105, 013101, 2009.

problems is the resulting losses. Various losses effect the performance of the nanotransducer in the integrated head such as the radiation loss, internal damping in the nanotransducer and the magnetic head, and load-induced loss due to the magnetic head. Chapter 2 of this thesis carries out a parametric study to minimize these losses. The magnetic head and the nanotransducer are modeled with multilayer configurations. The effect of load-induced damping of the magnetic head and evanescent coupling between the nanotransducer and the magnetic head is identified with the intensity enhancement near the magnetic head. It is shown that a higher intensity enhancement can be obtained by minimizing radiative and load-induced losses through adjusting layer thicknesses in multilayer configurations.

Although the aforementioned studies focus on performance of nanotransducers by taking into account the recording medium, there are other magnetic components that limit the transducer efficiency. As mentioned above, the magnetic write head that is in the vicinity of the nanotransducer is one of the magnetic components. There are a limited amount of valuable studies in the literature that present a complete HAMR system with all the necessary optical and magnetic components in the system. Among these studies, a triangular nanoantenna at the bottom of a thin-film wing structure is introduced as a near-field transducer for HAMR, as illustrated in Figure 1.13(a) [30]. Incident light is coupled to a rectangular waveguide that is in the vicinity of the wing structure, as illustrated in Figure 1.13(a). When the evanescent field of the waveguide is polarized along the x-direction the waveguide mode couples with the wing to excite surface plasmons on the wing. Surface plasmons then propagate toward the bottom of the wing, where a triangular nanoantenna is located, and excite localized surface plasmons on the nanoantenna. Thus, an optical spot is produced at the apex of the nanoantenna, as demonstrated in Figure 1.13(b). A FWHM of 16 nm for the absorption power distribution is obtained when the apex diameter is 12 nm. The ratio between the absorbed power in the medium and the power in the waveguide, which is named as the utilization efficiency, is obtained as % 8 by utilizing from an apex diameter of 12 nm. An areal density of 2.5 Tbit/in² is expected to be obtained by the recording head.

In addition to the above studies, recording demonstrations on storage media are presented with various HAMR heads. In one of the demonstrations, a PSIM without a

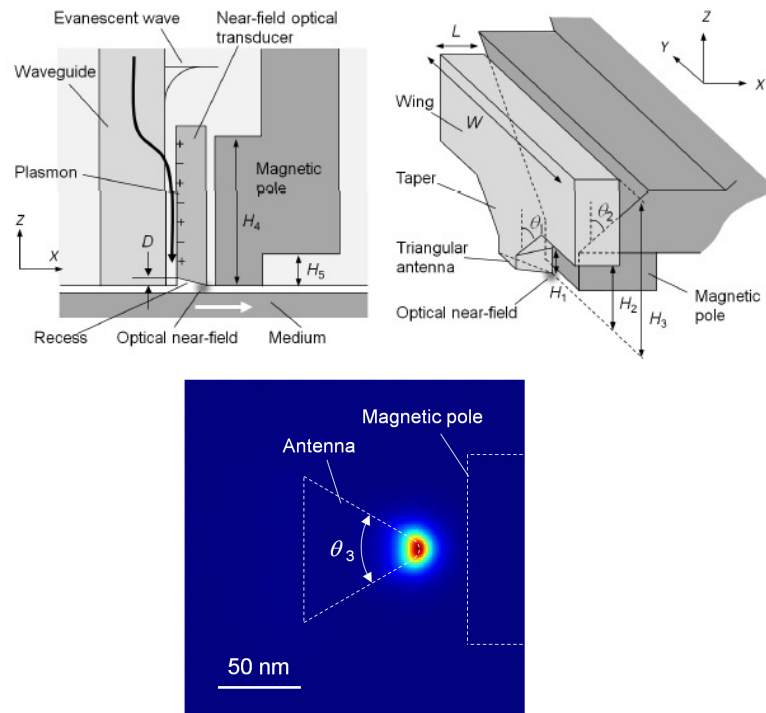


Figure 1.13 (a) Schematic representation of the triangular nanoantenna, the wing structure, and the magnetic pole, and (b) absorbed power distribution in the recording medium. Courtesy of T. Matsumoto et. al., *Opt. Express*, vol. 20, no. 17, pp. 18946-18954, 2012.

near-field nanotransducer at its focus is utilized to record tracks on a phase-change medium [31]. Obviously, the PSIM produced a diffraction-limited focused spot without the nanotransducer. Incident wavelengths of 488 nm and 833 nm are utilized. For an incident wavelength of 833 nm, a FWHM track width of $\sim 0.3 \mu\text{m}$ and track length of $\sim 0.25 \mu\text{m}$ that corresponds to $\lambda_{\text{inc}}/3$ is obtained, as depicted in the NSOM images in Figure 1.14(a). An asymmetry between the recorded marks in the down-track and cross-track directions is caused due to the asymmetric focused spot normal to the waveguide plane. For an incident wavelength of 488 nm, the dimensions of the recorded marks are reduced to a track width of 100-120 nm and track length of 130-150 nm, corresponding to $\lambda_{\text{inc}}/3$ - $\lambda_{\text{inc}}/4$, as seen in Figure 1.14(b). As seen in Figure 1.14(b) and Figure 1.14(c), at the high laser power, the recorded marks compose of a central spot and a side lobe; however for low laser power the marks are written with a central focused spot only.

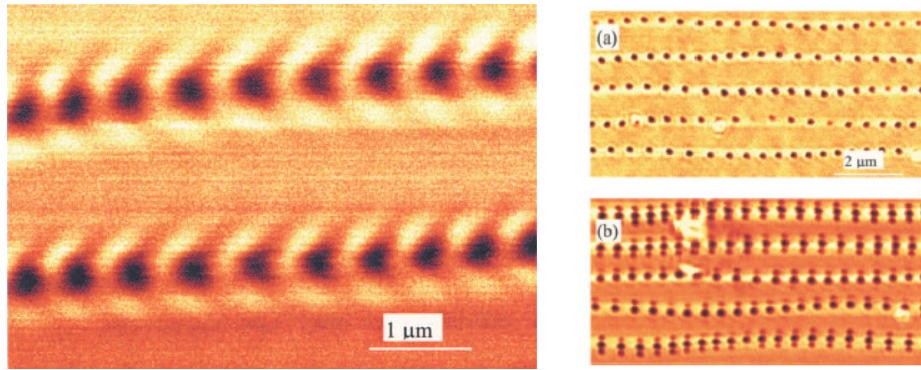


Figure 1.14 Recorded marks in a phase-change medium by the PSIM at (a) 833 nm, (b) 488 nm for 10 mW incident optical power, and (c) 488 nm for 15 mW incident optical power. Courtesy of C. Peng et. al., Appl. Phys. Lett., vol. 87, 151105, 2005.

To further reduce the track width and track length for higher areal density, a PSIM with a near-field nanotransducer is utilized in the recording process, as shown in Figure 1.15(a) [32]. As discussed in the previous studies [22-35], the PSIM can provide optical spots well beyond the diffraction limit, therefore higher areal densities can be obtained at the recording. During recording, an incident wavelength of 830 nm and optical power of 80 mW is utilized. Magnetic force microscopy images of the recorded tracks, as shown in Figure 1.15(b), demonstrate a track width of 74 nm. Thus, an areal density of $\sim 375 \text{ Tb m}^{-2}$ can be obtained. The track width is comparable to the width of the peg of the nanotransducer and has dimensions beyond the diffraction-limit of the incident wavelength.

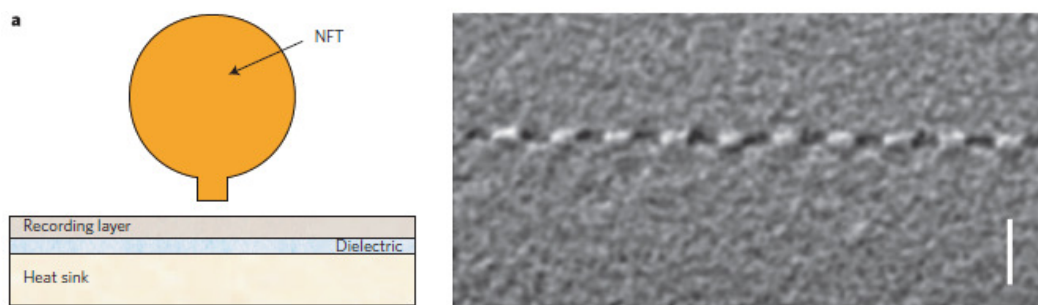


Figure 1.15 (a) Schematic representation of a near-field nanotransducer above a recording medium, (b) magnetic force microscopy images of a recorded track. Courtesy of W. A. Challener et. al., Nature Photon., 3, 220-224, 2009.

Another recording demonstration is performed by a HAMR head on bit-patterned media with an E-antenna nanotransducer [33]. A schematic representation of the

integrated head is shown in Figure 1.16(a). An incident focused light is coupled to a thin-film waveguide, propagates to the end of the waveguide, and couples with the E-antenna that is at the end of the waveguide. The E-antenna consists of a body, a wing, and a notch. The incident light is polarized parallel to the notch. The notch utilizes from the lightning rod effect to further localize the incident field. Utilizing from this configuration, an absorption profile of 30 nm x 28 nm is simulated in the cobalt medium. Utilizing from a bit-patterned medium recording has been performed. As seen via the magnetic force microscopy images, as seen in Figure 1.16(b), an areal density of 1.5 Tbit/inch² is achieved.

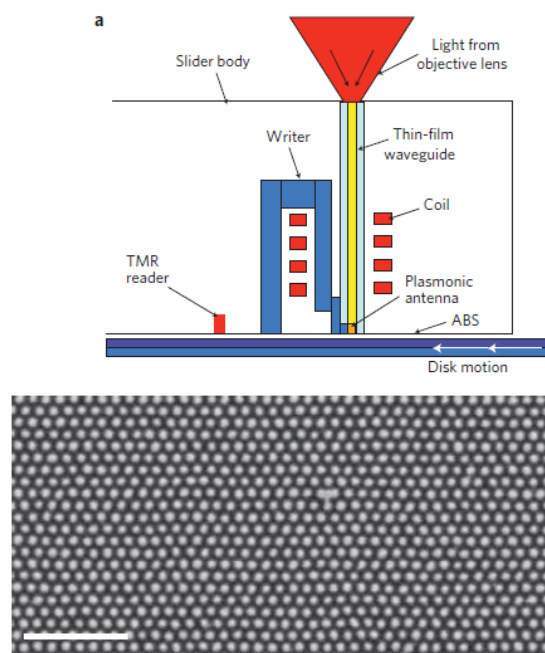


Figure 1.16 (a) Schematic representation of the integrated recording head, and (b) magnetic force microscopy image of the written tracks on a bit-patterned medium. Courtesy of B. C. Stipe, Nature Photon. 4, pp. 484-488, 2010.

In conclusion, various studies concerning the design and implementation of HAMR heads, and specific recording demonstrations with these heads have been presented. The effect of the recording medium and the magnetic write pole on the performance of nanotransducers are discussed and specific ways to recover the performance have been specified. As frequently highlighted in the studies, designing nanotransducers that can produce intense optical spots beyond the diffraction-limit and that have high transmission efficiency has been set as major design criteria in HAMR head design to achieve higher areal densities.

1.2.2 HAMR Media Design

In the above studies, the effect of the recording medium on the efficiency of various nanotransducers is widely discussed. In HAMR, the performance of the near-field nanotransducer can also be enhanced by properly designing the recording medium. For example, a patterned magnetic medium can be utilized that can provide higher optical energy coupling between a near-field transducer and the medium [34]. For conventional recording media, inefficient energy coupling exists between the transducer and the medium. The cause of this inefficiency is the discontinuity of the perpendicular component of the electric field between the transducer and the medium, as illustrated in Figure 1.17(a). A small perpendicular component in the medium results in a low coupling efficiency. Due to the need of a higher coupling, a patterned medium is designed that consists of isolated magnetic volumes filled with dielectric volumes in between them, as illustrated in Figure 1.17(b). In this medium, the tangential component of the electric field on the isolated volumes is continuous that brings forth a better optical coupling and a higher optical absorption. As a result, higher and more localized temperature distributions are obtained in the patterned medium compared to continuous recording medium.

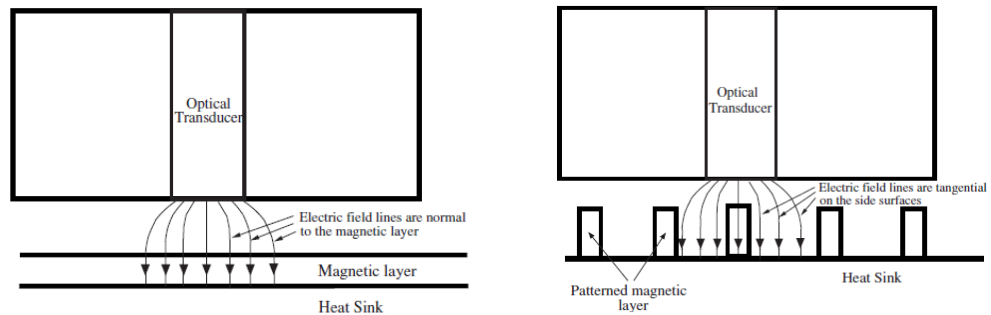


Figure 1.17 Schematic representation of two types of recording media. (a) A continuous recording medium, and (b) a patterned recording medium. Courtesy of K. Şendur et. al., *Appl. Phys. Lett*, 94, 032503, 2009.

In another study, a parametric study is performed to investigate the optical and thermal performance of a lollipop nanotransducer. Various thicknesses of a NiTa seed layer and an MgO interlayer underneath a FePtC recording layer is investigated, as

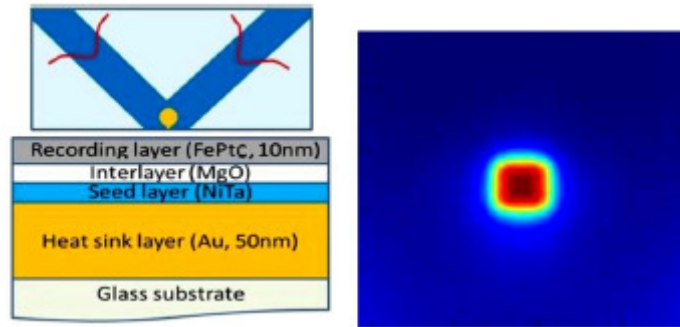


Figure 1.18 (a) Recording medium, MgO interlayer, and NiTa seed layer, and (b) electric field intensity distribution in the recording layer. Courtesy of B. Xu et. al., IEEE Trans. Magn., vol. 49, no. 6, 2013.

illustrated in Figure 1.18(a) [35]. It is demonstrated that the transducer efficiency increases with increasing MgO thickness, and decreases with increasing NiTa thickness. Furthermore, when the thickness of both MgO and NiTa is increased, the optical intensity distribution (FWHM of $|E|^2$) within the recording layer gets broadened. The thermal spot size within the recording medium is also investigated. The thermal spot size in the cross-track direction specifies the recorded track density, therefore smaller spot size are required. It is shown that the thermal spot size slightly increases as the thickness of the NiTa layer increases.

1.2.3 Thermal Aspects of HAMR

There are various optical and magnetic components in a HAMR system and the performance increase in the system depends on the consideration of each of these components. In the former sections, efforts to make HAMR systems more efficient were tackled from the optical head and recording media point of view. Resolving the thermal issues in an HAMR system has also an impact to further increase the performance of the system. This section discusses a wide range of studies that deal with the thermal aspects of HAMR systems. For example, one of the studies is about developing a thermal William-Comstock model to predict the transition length in a longitudinal HAMR system, as represented in Figure 1.19 [36].

Conventionally, William-Comstock model is utilized to predict the transition parameters in non-HAMR systems. For HAMR systems, thermal gradients and heating

is incorporated to the William-Comstock model to investigate the effect of transition parameters on the transition length. To adapt the William-Comstock model for HAMR, the William-Comstock slope equation is modified by introducing an additional thermal term to the equation. This term is the product of the thermal gradient of coercivity (dH_c/dT) and the spatial derivative of the temperature profile in the medium (dT/dx). The slope equation is solved assuming an arctangent transition profile. Since the transition profile is characterized by the transition parameter and the transition center, as depicted in Figure 1.19, the transition parameter is utilized in the micromagnetic simulations.

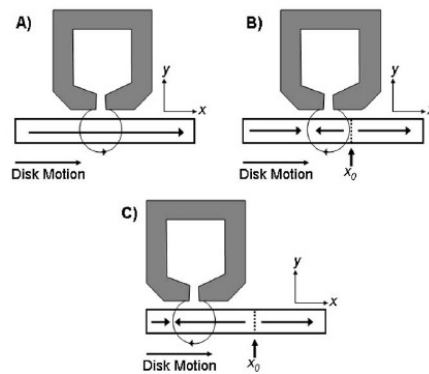


Figure 1.19 Schematic representation of the longitudinal recording process. (a) The magnetic head and the recording layer before the recording process, (b) a produced transition as a result of the switch in the head field, and (c) the transition moving along the disk motion away from the gap of the magnetic head. Courtesy of T. Rausch et. al., IEEE Trans. Magn., vol. 40, no. 1, 2004.

In another study, a novel recording medium is proposed that yields small thermal spot sizes in the medium. A new media structure called surface plasmon assisted HAMR (SPA-H) media is introduced, and optical and thermal aspects of the media are investigated, as illustrated in Figure 1.20(a) [37]. The media is composed inter-digitated cobalt recording strip layers on metal/dielectric layers. A linearly polarized light is incident on a HAMR head consisting of a nano-slit aperture in between two silver gratings. The incident light on the aperture couples with the metal/dielectric layers in the recording medium, and excites surface plasmons at the metal/dielectric interfaces. As a result, optical spots with FWHM dimensions of 8 x 170 nm are obtained on the interfaces, as shown in Figure 1.20(b). In order to investigate the cross-talk issues in the recording medium, the temperature distributions were also obtained for continuous and

SPAH media, as depicted in Figure 1.20(c). For continuous media, the temperature distributions are in the form of thermal spots in the recording medium enabling a local increase in the medium temperature only on the recorded track, as seen in Figure 1.20(c). For SPAH media, the thermal spot size in the medium is also small, and the maximum of the temperature is higher than the continuous medium. Due to small spot sizes, SPAH media is a strong candidate to be utilized as a HAMR recording medium.

Another study investigates the recorded mark width as a function of the laser power theoretically and experimentally [38]. The finite volume method (FVM) is utilized to solve the heat transfer problem. A multilayer stack that is composed of a substrate and a recording layer is considered. All four sides of the model are kept at room temperature, a symmetric boundary condition is applied at the bottom surface, and the top surface is selected as a convective surface. The width of the model is selected to be 5 times larger than the size of the laser spot. It is demonstrated that a smaller laser spot produces a larger mark width; however the increase is not linear due to the Gaussian distribution of the laser intensity. Furthermore, the variation of the time-varying temperature distribution within the lubricant is investigated. It is found that after the laser is removed, the temperature in the lubricant layer decreases very quickly. It is shown that the temperature decreases more rapidly when there is a heat sink layer under the recording medium.

The efficiency of a near-field nanotransducer is evaluated for various writer pole arrangements and for various distances from the writer pole [39]. The nanotransducer is modeled as a rectangular tip, as illustrated in Figure 1.21. As seen in Figure 1.21(b) and Figure 1.21(c), a strong plasmonic enhancement is obtained at the edges of the nanotransducer. The distance between the media and the nanotransducer is crucial. Evanescent decay is observed in the intensity with increasing distance of the media from the nanotransducer. Thus, the HAMR head design may operate with a higher efficiency when the distance between the air-bearing surface and media is reduced.

A two-step heating scheme is proposed for HAMR to increase the reliability of near-field nanotransducers under cyclic thermal loading conditions [40]. The optical head consists of a bow-tie aperture near a waveguide, as illustrated in Figure 1.22(a). As seen in Figure 1.22(b), in the first step, the waveguide confines and transmits laser

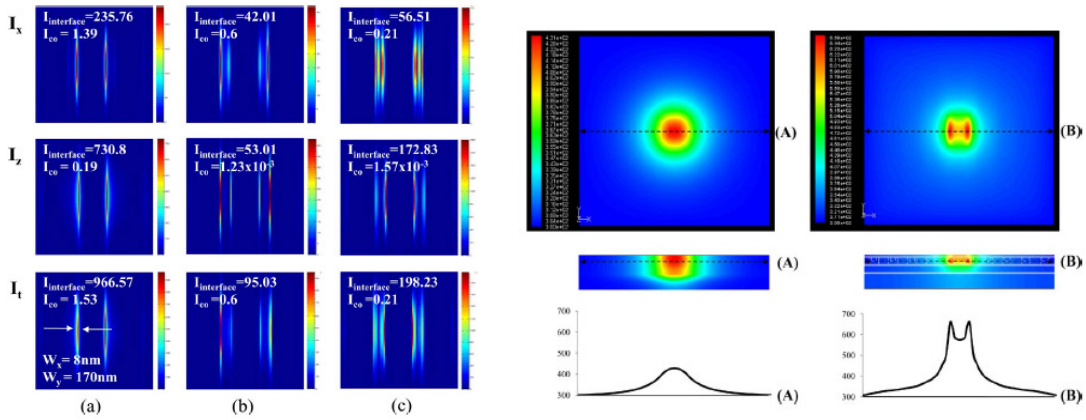
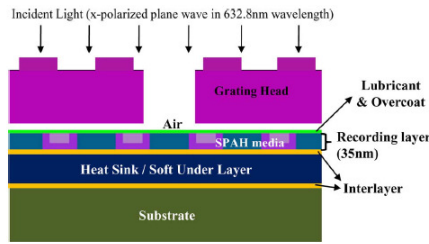


Figure 1.20 Schematic illustration of the HAMR head and the recording medium, (b) temperature distributions in the medium, and (c) thermal spot sizes in the medium. Courtesy of D.-S. Lim et. al., IEEE Trans. Magn., vol. 45, no. 10, 2009.

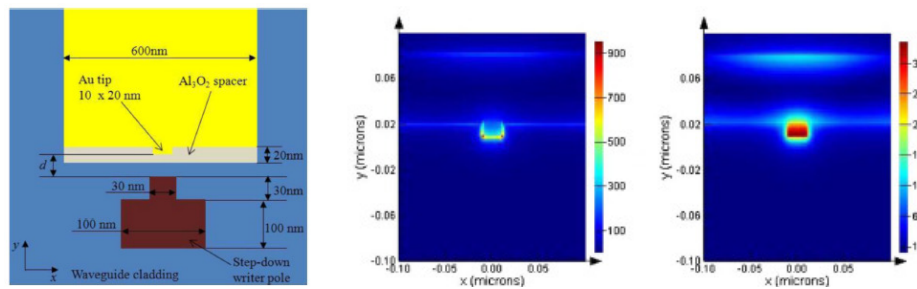


Figure 1.21 (a) Schematic representation of the rectangular nanotransducer and the writer pole, (b) electric field intensity distribution on the cut-plane through the nanotransducer in the air-bearing surface, and (c) electric field intensity distribution on the cut-plane through the nanotransducer in the recording medium. Courtesy of J. Li et. al., IEEE Trans. Magn., vol. 49, no. 7, 2013.

energy and heats the disk to a temperature of about 200°C, which is lower than the Curie temperature. At this temperature, the magnetic bits in the neighboring tracks are

not erased. In the second step, the nanotransducer further heats a smaller area inside the heated area to reach the Curie temperature. As a result of this two-step process, the thermal load on the nanotransducer is reduced, and longer lifetimes for the transducer may be expected, which may ensure the five year warranty requirements for magnetic data storage devices.

The effect of alignment between the thermal gradient and the field gradient is investigated by a micromagnetic recording model [41]. Three modes of HAMR have been proposed, as schematically represented in Figure 1.23: (1) magnetically dominant HAMR where there is a large optical spot and a smaller magnetic write bubble than the optical spot. In this configuration, the temperature can be raised just below the Curie temperature, consequently the heated spot has no effect on the writing process. This configuration negatively affects the thermal stability of the neighboring track due to the

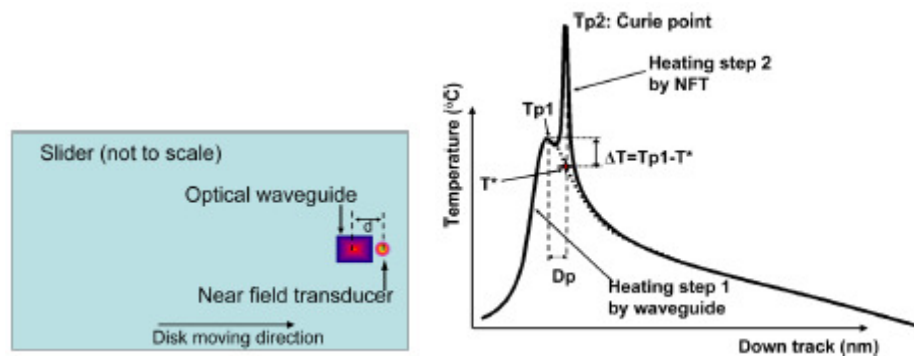


Figure 1.22 (a) Schematic representation of the optical waveguide and the near-field nanotransducer, and (b) the two-stage heating scheme of the recording medium. Courtesy of S. Xiong et. al., Appl. Phys. Lett., 115, 17B702, 2014.

large optical spot. The neighboring track is heated to a temperature that has almost the same temperature as the track that will be written. (2) Intermediate HAMR mode where the optical spot and the magnetic write bubble have almost the same size. In this design, collocating the heated spot and the magnetic write bubble is more difficult, but the adjacent track is not erased. (3) Thermally dominant HAMR mode where the heated spot is smaller than the write bubble. In this configuration, the recording medium can be heated near the Curie temperature. Collocating the magnetic delivery system with the optical delivery system is easier in this configuration.

The thermally dominant HAMR mode is utilized to simulate the recording process via a micromagnetic media model, as depicted in Figure 1.23(d). The thermally dominant HAMR mode is utilized because a significant increase in the areal density is obtained when the writing process is performed near the Curie temperature. From the simulations, it is concluded that the thermal-magnetic separation, which is the separation between the maximum of the field profile and maximum of the thermal profile, is crucial in specifying the achievable linear density. As the thermal-magnetic separation decreased, the signal to noise ratio (SNR) increased.

By utilizing from a multilayered micromagnetic model, the vertical thermal gradient in a recording medium is investigated [42]. For the write head, a 3-D finite element model was utilized to study a monopole perpendicular head with a soft underlayer. A thermally dominant HAMR configuration is considered in which the magnetic bubble is larger than the thermal spot in the recording medium.

The optical spot is assumed to be perfectly aligned with the maximum value of the magnetic field. In addition, for the media model, an array of square sized grains is utilized to simulate the perpendicular recording media. The media is assumed to possess a temperature dependent anisotropy, saturation magnetization, and anisotropy constant. The signal-to-noise ratio (SNR) is simulated at a linear density of 2300 kfc/in and an areal density of $\sim 1\text{Tbit/in}^2$.

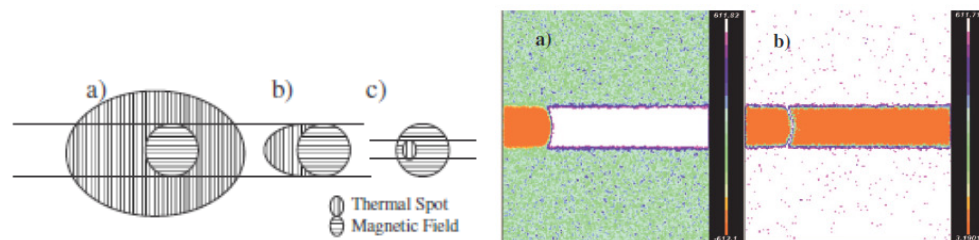


Figure 1.23 (a) Magnetically dominant HAMR, (b) intermediate HAMR, (c) thermally dominant HAMR, (d) average remanent magnetization for a modeled isolated HAMR transition, and (e) standard deviation of the magnetization from the average remanent magnetization. Courtesy of N. J. Gokemeijer et. al., *Appl. Phys. Lett.*, 105, 07B905, 2009.

1.2.4 Magneto-Optics Sensors

At first glance, magneto-optics seems to reside in a completely different category than heat-assisted magnetic recording. Even so, their geometric configurations and underlying physical phenomena have common similarities. The presence of thin magnetic films near plasmonic layers that are utilized to alter the surface plasmon resonance properties in magneto-optical sensors, and the presence of magnetic recording heads in the form of thick-films near plasmonic nanostructures in HAMR define the geometric commonalities. As for physical similarities, surface plasmons in magneto-optical sensors and on plasmonic nanotransducers are both subject to induced damping due to the magnetic components in the system, which degrades the quality of surface plasmon resonances.

This section aims to present a survey of studies that utilize from the magneto-optic effect and surface plasmon resonances to design surface plasmon resonance (MOSPR) sensors. Specific sensor configurations are demonstrated that use the magneto-optic effect to enhance the performance of surface plasmon resonance (SPR) sensors. MOSPR sensors have main differences in their operating principles in comparison with SPR sensors. Unlike SPR sensors, a magnetic field is applied to MOSPR sensors that have a field component perpendicular to the direction of surface plasmon propagation. MOSPR sensors consist of a ferromagnetic thin-film near a plasmonic thin-film, as illustrated in Figure 1.24 [43]. The applied magnetic field excites the transverse magneto-optic Kerr effect (TMOKE) and surface plasmon resonances. The applied magnetic field can induce a specific shift in the surface plasmon wavevector. Consequently, it varies the surface plasmon excitation angle and creates a specific shift in the reflectance spectra of surface plasmons. These very small variations in the reflectance spectra can be exploited to characterize a variety of biological and chemical samples.

In the literature, MOSPR sensors are investigated for the label-free detection of DNA hybridization of very short DNA chains [43]. For this purpose, multilayer configurations with cobalt and gold layers are utilized, as shown in Figure 1.24. Like SPR sensors, MOSPR sensors have drawbacks that suffer them from optical losses.

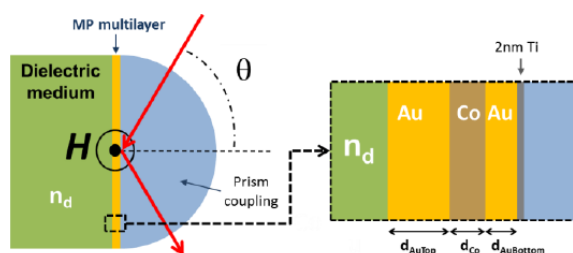


Figure 1.24 Schematic illustration of a magneto-optic sensor in the form of an Au/Co/Au structure within the Kretschmann configuration. Courtesy of D. Regatos et al., *Opt. Express*, vol. 19, no. 9, 2011.

Enhancing the magneto-optic activity increases the optical absorption of ferromagnetic metals, which causes damping of surface plasmons resonances. Therefore, the balance between magneto-optic activity and sensing performance should be taken into account while designing these devices.

On the other hand, there are recent efforts to achieve high magneto-optic activity with reduced optical losses by utilizing from SiO₂ interlayers in Au/Co/Au nanodisks, as illustrated in Figure 1.25 [44]. The SiO₂ layer can modify the extinction properties of the nanodisks, and specific locations of the SiO₂ layer enable to control the spectral region where the extinction is maximized or minimized. Extinction spectra of the nanodisks are investigated to characterize the optical properties. In the spectra of Au/Co/SiO₂/Au nanodisks, a peak around 750 nm (high wavelength peak) and a shoulder around 600 nm (low wavelength peak) is observed, similar to the spectra of Au/SiO₂/Au nanodisks. A certain discrepancy in the Au/Co/SiO₂/Au spectra is the damping and blueshift of surface plasmon resonances due to the absorption of the cobalt layer.

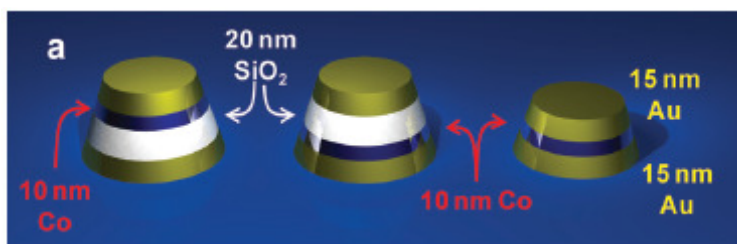


Figure 1.25 Schematic representation gold nanodisks with and without SiO₂ layers. Courtesy of J. C. Banthí, *Adv. Mater.*, vol. 24, no. 10, 2002.

For the Au/SiO₂/Co/Au nanodisks a drastic change is observed in the optical response. The extinction spectrum is reversed, having a shoulder only in the low wavelength peak region. However, the complex Kerr rotation spectrum of Au/SiO₂/Co/Au nanodisks is found to be very similar to Au/Co/SiO₂/Au nanodisks with a peak in the high wavelength peak region and a shoulder in the low wavelength peak region. This implied a high magneto-optic activity with a lower optical extinction in the high wavelength peak region.

Besides exhibiting magneto-optic activity, some specific nanostructures can demonstrate both magneto-optic activity and plasmonic effects. In one of these studies, it is demonstrated that nanoparticles of Au/Co/Au layers fabricated by colloidal nanolithography can exhibit high magneto-plasmonic effects [45]. The extinction spectra of the nanoparticles showed a distinct peak that depicts the existence of localized surface plasmon resonances (LSPR) in the nanoparticles. The extinction spectrum of an Au/Co/Au multilayer and a single gold nanoparticle is compared. Broadening is observed in the LSPR peak, as well as a shift of the peak to higher energies for the Au/Co/Au multilayer. The broadening has been ascribed due to the high absorption of cobalt. The effect of nanoparticle diameter is also investigated. The LSPR peak shifted to lower energies as the diameter of the nanoparticle increased.

As mentioned in the above studies [43-45] cobalt thin-films lead to a magneto-optic activity in MOSPR sensors, which greatly enhances their performance. On the other hand, damping of cobalt films on surface plasmon resonances is observed that reveals itself as shifting and broadening of the resonances. In conventional SPR sensors similar problems may be encountered. Lossy samples may induce damping that deteriorates the quality of plasmons resonances. The amount of damping varies with the amount of loss and thickness of the samples. For optically thick and lossy films, damping levels may elevate and even diminish the resonances. In SPR sensors, high quality resonances are required to characterize lossy films with high sensitivity. Chapter 5 of this thesis treats this issue by investigating the underlying reasons of the damped plasmon resonances in multilayered SPR sensors with thick cobalt samples, and presents specific sensor configurations that recover the plasmon resonances in the presence of the samples. As a contribution to the literature, analytical expressions that represent the poles of various multilayers are specified and adjusted to yield a better

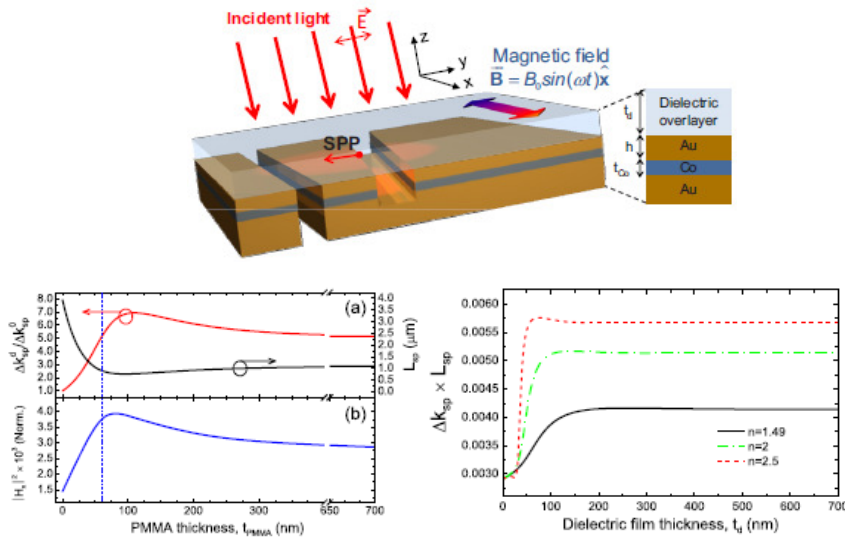


Figure 1.26 (a) Schematic representation of an Au/Co/Au multilayer with a PMMA overlayer, (b) PMMA thickness as a function of surface plasmon propagation length, and (c) figure of merit $\Delta k_{spp} \times L_{spp}$ for the multilayer for various refractive indices of the overlayer. Courtesy of D. Martín-Becerra et. al., Appl. Phys. Lett., 97, 183114, 2010.

sensor performance. As a result of the recovered resonances, a higher plasmonic enhancement on the sensing layer of the sensors is obtained. Electric field intensity profiles corresponding to the recovered resonances are evaluated for specific sensor configurations.

Studies in the literature aim to enhance and manipulate the modulation of the surface plasmon wavevector. In one of these studies, poly(methyl methacrylate) (PMMA) coatings on Au/Co/Au multilayers are utilized, as illustrated in Figure 1.26 [46]. It is analytically shown that the modulation term has a squared dependence on the permittivity of PMMA. Thus, utilizing from a high index dielectric such as PMMA can provide a higher modulation of the wavevector. The application of an overlayer increases the modulation, but decreases the surface plasmon propagation length. On the other hand, high plasmon propagation lengths are required in devices such as magneto-plasmonic interferometers to exploit from the unique properties of surface plasmons.

A magneto-plasmonic interferometer is basically a gold/cobalt/gold multilayer. To analyze the dependence of propagation length on the overlayer thickness, a figure of merit of $\Delta k_{spp} \times L_{spp}$ is specified where Δk_{spp} is the shift in the surface plasmon wavevector and L_{spp} is the propagation length. As Figure 1.26(b) depicts, as the

thickness of the dielectric film increases, L_{spp} decreases. This decrease can be compensated by an increase in Δk_{spp} such that $\Delta k_{\text{spp}} \times L_{\text{spp}}$ increases, as shown in Figure 1.26(c). The figure of merit $\Delta k_{\text{spp}} \times L_{\text{spp}}$ is proportional to the modulation depth in magneto-plasmonic interferometers. Thus, it is shown that the modulation depth can be increased despite the reduction of the propagation length. This finding is therefore a step towards the miniaturization of magneto-plasmonic devices.

One of the important studies aims to modify the wavevector of surface plasmons in a gold/cobalt/gold multilayer configuration by a weak external magnetic field of a few militesla to allow for local probing of the electromagnetic field distribution within the gold layer [47]. As illustrated in Figure 1.27, surface plasmons are excited by a groove that is processed on the gold layer. Surface plasmons once excited, propagate to the slit. As they propagate, they are converted into free-space radiation and interfere with the transmitted radiation through the slit. Due to the slit-groove tilt angle, surface plasmons exhibit a linearly changing path difference as they propagate to the slit, which results in a sinusoidal interference pattern.

To rigorously handle the wavevector shift of surface plasmons an analytical expression for the wavevector shift as a result of the magnetization switching in the magnetic layer is provided as a function of the magnetic field and the position of the cobalt layer. It can be seen from that expression that the wavevector modulation reaches its maximum when magnetization

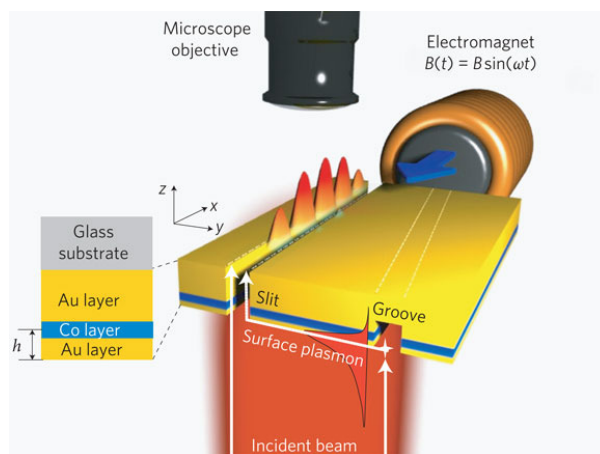


Figure 1.27 Schematic illustration of a gold/cobalt/gold multilayer with a tilted groove-slit pair. Courtesy of V. V. Temnova et. al., Nature Photon., 4, 2, pp. 107-111, 2010.

switching ($M = \pm 1$) occurs. Thus, when an external and oscillating magnetic field is applied to the multilayer the wavevector can be varied. Consequently, the phase and contrast of the interferogram is altered, allowing by a scanning imaging optical setup to obtain the interference pattern.

In conclusion, various MOSPR sensors in the form of multilayer films and nanodisks were reviewed. These sensors utilized from the magneto-optic effect and surface plasmon resonances to enhance the signal-to-noise ratio and measurement sensitivity. Lower absorptive losses in these sensors were obtained and high magneto-optic activity was achieved. Furthermore, the modulation of the wavevector of magneto-optic interferometers was improved by dielectric coatings. As can be seen from the studies, one of the problems in MOSPR sensors is the resulting losses. Remedies were found to reduce the losses.

1.3 Contribution

The contributions of this PhD dissertation are listed below:

- A. Multilayer configurations with gold thin-films near magnetic thin-films are investigated that minimize radiative and load-induced losses.
- B. A novel planarly modeled HAMR head is introduced that can protect the damping effect of the magnetic write head from the plasmonic transducer.
- C. A plasmonic planar solid immersion mirror (Plasmonic PSIM) is designed, and theoretically and experimentally demonstrated to produce intense and localized optical spots beyond the diffraction-limit.
- D. Multilayered surface plasmons resonance sensors with lossy samples are demonstrated that can provide high quality resonances.

1.4 Thesis Outline

Section 4 of this dissertation investigates various multilayer configurations with gold thin-films near magnetic thin-films to minimize radiative and load-induced losses. Section 5 investigates the reliability and performance of HAMR integrated heads via multilayer configurations. In Section 6, a plasmonic planar solid immersion mirror (PSIM) that is to be utilized as a HAMR head is theoretically and experimentally investigated. Section 7 leaves the HAMR concept by treating the multilayer configurations with gold thin-films near magnetic films as plasmonic sensors with lossy samples. It is demonstrated that plasmon resonances can be recovered in the presence of lossy samples.

2 INTEGRATING MAGNETIC HEADS WITH PLASMONIC NANOSTRUCTURES IN MULTILAYER CONFIGURATIONS

Integrating magnetic thin-film heads with plasmonic nanotransducers has gained importance in magnetic data storage concepts because of its promise to overcome the superparamagnetic limit [48-49]. Integrated heads offer significant advancement in the performance of hard disc drives by lowering the coercivity of magnetic grains via localized heating of the grains during the recording process [50-55]. The magnetization of the grains can then be changed by the applied magnetic field of the integrated head, which has paved the way for HAMR. In addition to several other technical challenges [56-58], integrating plasmonic structures with magnetic heads involves difficulties. Recently, there has been increased interest in integrating plasmonic structures with magnetic heads [59,60].

Several studies in the literature have utilized magnetic thin-films near gold thin-films in multilayer configurations. By periodically switching the magnetization of a cobalt film by a weak external magnetic field the wave vector of surface plasmons in a gold/cobalt/gold multilayer is modulated [61]. The skin depth of an optical field in the gold thin-film is specified from the shift in the wave vector. Furthermore, the large magneto-optic response of cobalt is utilized to increase the reflectivity of a gold/cobalt/gold multilayer; this principle has been used in biosensor applications [62].

In a HAMR system, a near-field transducer in an integrated head produces an intense and localized optical spot to locally heat the magnetic grains above the Curie temperature. Moreover, the optical spot should be collocated with the magnetic field produced by the magnetic head in the recording medium to vary the magnetization of a grain during heating. Integrating magnetic heads with plasmonic transducers leads to a performance loss as a result of load-induced damping, internal damping, and radiation loss, which cause lower intensity enhancements near the magnetic heads.

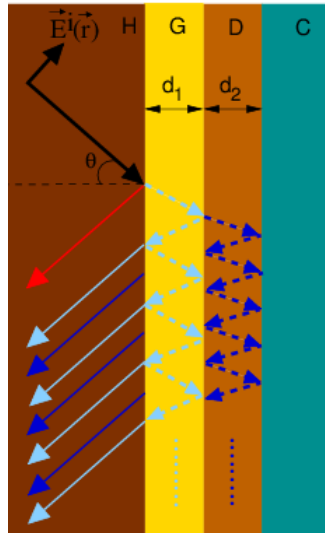


Figure 2.1 Schematic illustration of a four-layer multilayer with a gold thin-film near a cobalt layer. The red arrow illustrates the primary reflections from the H-G interface. The light blue and blue arrows represent the reflections from the G-D and D-C interface, respectively. The thickness of the gold layer and dielectric layer is d_1 and d_2 .

In this study, multilayer configurations with gold thin-films near magnetic films are investigated, and optimum configurations are identified to minimize losses. The effects of load-induced damping and evanescent field coupling on the intensity enhancement near magnetic films are identified. Optimum configurations yield higher intensity enhancement due to lower losses and better evanescent coupling.

A four-layer multilayer that is composed of quartz, gold, dielectric, and cobalt films is illustrated in Figure 2.1. A linearly polarized plane wave is incident on the quartz/gold interface. The quartz layer is chosen to increase the value of the incident wave vector to the surface plasmon wave vector in order to excite surface plasmons on the gold thin-film. The magnitude of the incident field is selected as 1 V/m in this study. Thus, the electric field intensity values that are obtained in the multilayers correspond to intensity enhancements. The operation wavelength is selected as $\lambda = 633$ nm. The dielectric constants of gold and cobalt at 633 nm are $\epsilon_1 = -9.51 + 1.15i$ and $\epsilon_3 = -12.49 + 18.45i$, respectively [63].

2.1 Methodology

In this study, various four-layer multilayer configurations are investigated to minimize radiative and load-induced losses. To analyze this problem, the propagation matrix method [64] is employed. The multilayer is illuminated with a linearly polarized plane wave that can be expressed as

$$\vec{E}^i(\vec{r}) = \vec{E}_0^i \exp(i\vec{k} \cdot \vec{r}) . \quad (2.1)$$

where \vec{E}_0^i is composed of tangential and perpendicular components to the quartz/gold interface. When the incident field \vec{E}^i interacts with the multilayer film, various primary and secondary reflections and transmissions occur at the interfaces that generate scattered field \vec{E}^s . The total field \vec{E}^t is the summation of the incident field \vec{E}^i and scattered field \vec{E}^s . To obtain the total field \vec{E}^t in each layer, the total field \vec{E}^t in the quartz layer is calculated using the reflection coefficient of the four-layer multilayer [64], which can be expressed as

$$R = \frac{\exp(2ik_{z0}d_0)}{R_{01}} + \frac{\left[1 - (1/R_{01}^2)\right] \exp\left[2i(k_{z0} + k_{z1})d_0\right]}{(1/R_{01}) \exp(2ik_{z1}d_0)} \Big| \quad (2.2)$$

$$+ \frac{\exp(2ik_{z1}d_1)}{R_{12}} + \dots + R_{23} \exp\left[2ik_{z2}(d_1 + d_2)\right] .$$

where R_{01} , R_{12} , and R_{23} are the reflection coefficients of the quartz/gold, gold/dielectric, and dielectric/cobalt interface, respectively. In addition, d_0 , d_1 , and d_2 are the thicknesses of the gold, dielectric, and cobalt layer, respectively. k_{z0} and k_{z1} are the transverse wave numbers in quartz and gold, respectively. The vertical bar | operates as a continued fraction for the second term and other specific terms in the reflection coefficient expression. Thus, the reflection coefficient may be obtained by calculating the last term and advancing to the first term of the expression. In this study, the values for reflectivity for various multilayers are obtained using Equation (2.2).

Considering the continuity of the tangential component of the electric field across an interface between two layers, a propagation matrix may be obtained that relates the

electric field amplitudes of the total field \vec{E}^t in the quartz layer to other layers [64]. This matrix can be expressed as

$$\begin{pmatrix} E_m^r \exp(-ik_{zm}d_m) \\ E_m^i \exp(ik_{zm}d_m) \end{pmatrix} = \overline{\overline{V}}_{m(m-1)} \cdot \overline{\overline{V}}_{(m-1)(m-2)} \dots \overline{\overline{V}}_{(l+1)l} \cdot \begin{pmatrix} E_l^r \exp(-ik_{zl}d_l) \\ E_l^i \exp(ik_{zl}d_l) \end{pmatrix}. \quad (2.3)$$

where E_l^i and E_m^i are the incident field amplitudes, and the sub-index denotes the layer number. E_l^r and E_m^r are the reflected field amplitudes in layer l and layer m . For $m > l$ a forward propagation matrix is obtained that relates the field amplitudes of an upper layer to a lower layer. $\overline{\overline{V}}_{(l+1)l}$ is the propagation matrix, which relates the incident and reflected field amplitudes in layer l to that in layer $l+1$. As expressed in Equation (2.3), by the multiplication of propagation matrices the electric fields in various layers can be obtained. By adding the fields in each layer, the total field \vec{E}^t in the multilayer is obtained.

2.2 Losses and Evanescent Coupling of Multilayers

The effect of various losses on the intensity enhancement near cobalt films is investigated. An important factor on the intensity enhancement is the evanescent coupling of surface plasmons on the gold film with the cobalt film, which may increase the intensity enhancement when the coupling between the films is strong. To investigate these aspects, exciting surface plasmons on a gold thin-film is assessed by utilizing the attenuated total reflection (ATR) configuration as illustrated in Figure 2.1.

As shown in Figure 2.2(a), for a multilayer with a gold and dielectric thickness of 30 nm and 176 nm, the minimum value of the reflectivity curves shifts to a smaller angle of incidence when the incident wavelength is longer. Since the incident wavevector \vec{k} has a smaller value when the incident wavelength has a higher value, the transverse wavenumber k_z gets smaller. To compensate for the optical path length, k_z

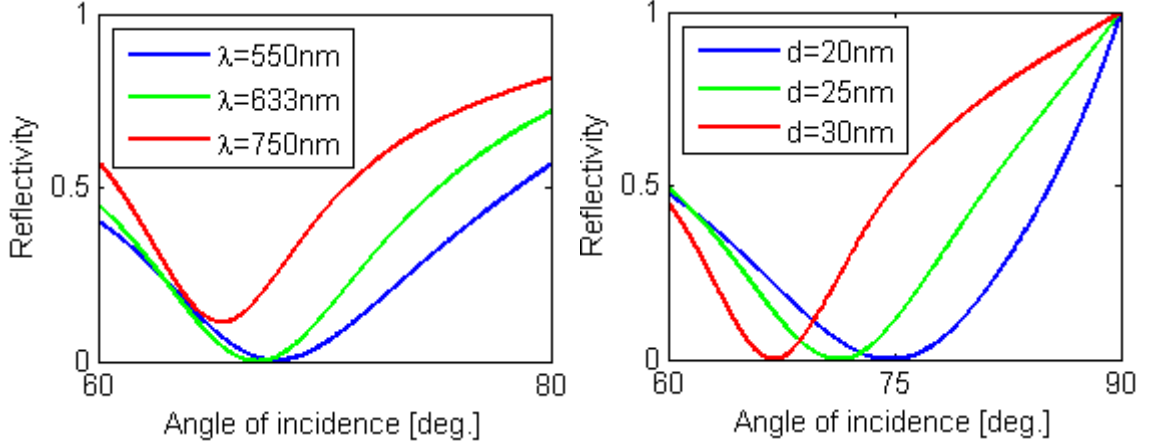


Figure 2.2 Reflectivity as a function of the angle of incidence for various operation wavelengths of (a) 550 nm, 633 nm and 750 nm, and gold thicknesses of (b) 20 nm, 25 nm and 30 nm. The thickness of the dielectric layer in (b) is 98 nm, 126 nm, and 176 nm, respectively. The operation wavelength in (b) is 633 nm. The refractive index of the dielectric is $n=1.2$.

is increased for a smaller angle of incidence. As shown in Figure 2.2(b), various multilayers with a gold thickness of $d_1 = 20$ nm, 25 nm, and 30 nm have a zero reflectivity at angles of incidence values of 74.7° , 71.3° , and 67° , respectively. These results show that destructive interference happens at a smaller incident angle when the thickness of the gold and dielectric layer increases. The reflectivity expression of a four-layer system can be expressed as [65]

$$r = \left| \frac{R_{1,2} + \tilde{R}_{2,3} \exp(2ik_{z,2}d_1)}{1 + R_{1,2}\tilde{R}_{2,3} \exp(2ik_{z,2}d_1)} \right|^2 \quad (2.4)$$

where $R_{1,2}$ is the reflection coefficient of the quartz/gold interface. $\tilde{R}_{2,3}$ is the generalized reflection coefficient that incorporates reflections from the quartz layer. The term $\tilde{R}_{2,3} \exp(2ik_{z,2}d_1)$ incorporates the optical path length of the reflected waves in the gold layer. The reflectivity expressions in Equation (2.2) and (2.4) provide the same values, however the electric field profiles can only be obtained by Equation (2.2), whereas it is easier to specify conditions for destructive interference in the multilayer by the closed-form expression in Equation (2.4).

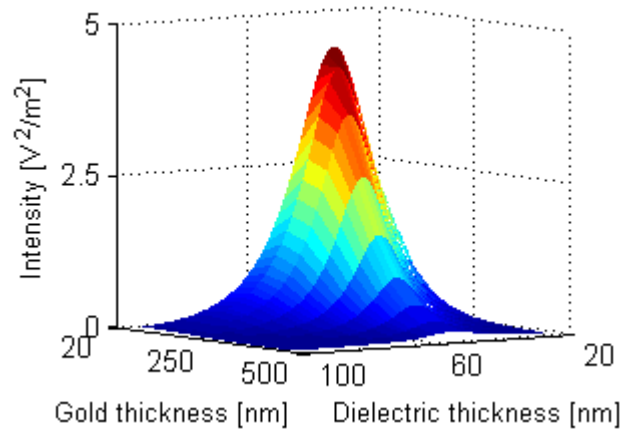


Figure 2.3 Intensity enhancement at the cobalt/dielectric interface as a function of gold thickness and dielectric thickness. The refractive index of the dielectric layer is $n = 1.2$. The operation wavelength is 633 nm.

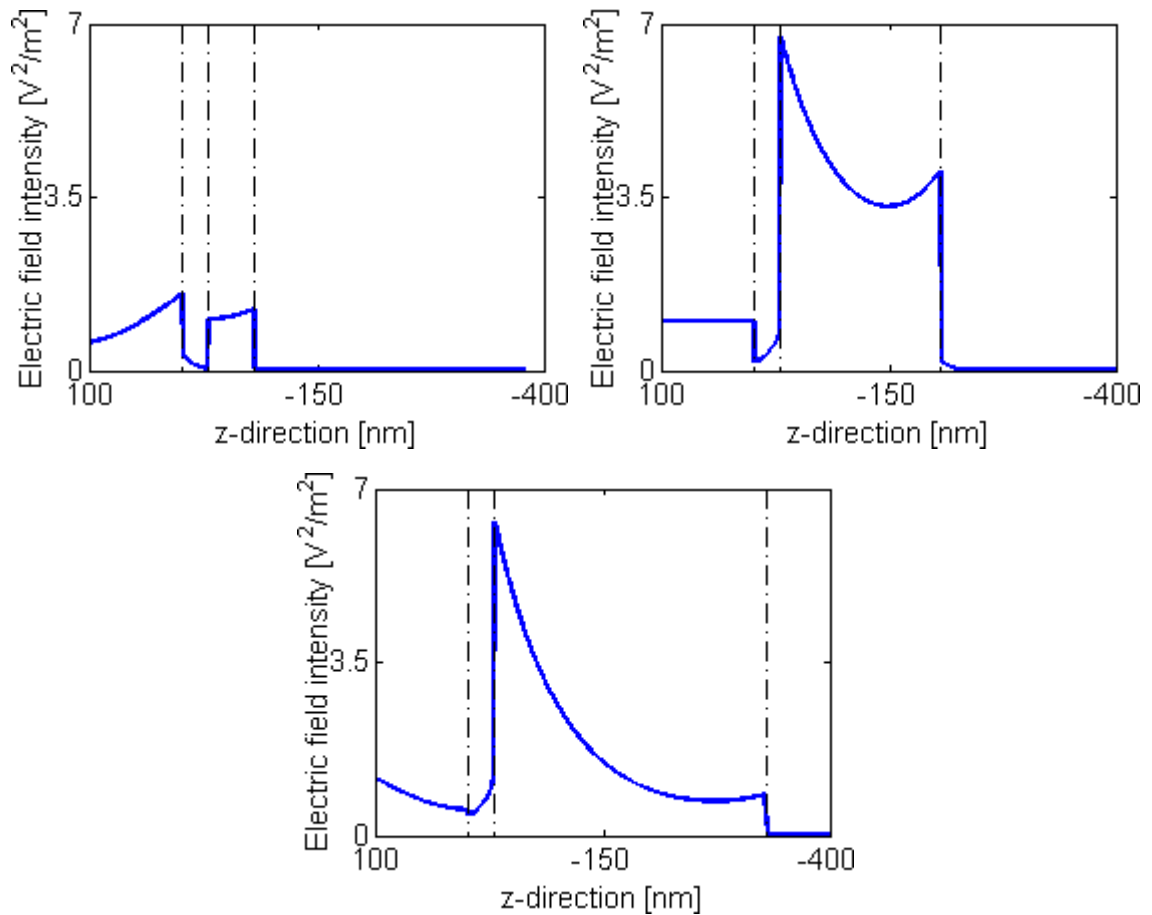


Figure 2.4 Electric field intensity profiles of various multilayers with a dielectric thickness of (a) 50 nm, (b) 176 nm, and (c) 300 nm. The thickness of the gold layer is selected as 30 nm. Refractive index of the dielectric layer is $n = 1.2$. The incident angle is 67° . The operation wavelength is 633 nm.

When the incident angle decreases from 71.3° to 67° the gold thickness increases from 25 nm to 30 nm, and the amplitude and phase of the reflection coefficient $R_{1,2}$ obtains a value of $A_{1,2} = 0.94$ and $\phi_{1,2} = 0.6\pi$. In addition, the magnitude and phase of the term $\tilde{R}_{2,3} \exp(2ik_{z,2}d_1)$ obtains a value of $A_{2,3} = 0.94$ and $\phi_{2,3} = -0.4\pi$. A unit amplitude ratio and a phase difference of π is obtained for the electric field components at the quartz/gold interface. Therefore, incident and back-scattered fields destructively interfere, resulting in zero reflectivity.

Intensity enhancements on cobalt film as a function of gold and dielectric film thicknesses are demonstrated in Figure 2.3. A maximum intensity enhancement of 4.12 is obtained when the thickness of gold and dielectric is 30 nm and 160 nm, respectively. The intensity enhancement decreases as the gold and dielectric thickness are varied from these values. When the gold thickness increases, a bigger fraction of incident photons are absorbed in gold film, and interaction of photons with surface plasmons at gold/dielectric interface decreases. When the dielectric thickness is varied, evanescent coupling decreases, resulting in weaker intensity enhancement.

The effect of cobalt-induced damping and evanescent coupling on intensity enhancement is further investigated in Figure 2.4. Electric field profiles are obtained for a gold thickness of 30 nm, and various dielectric thicknesses of 50 nm, 176 nm, and 300 nm. As shown in Figure 2.4, the electric field profile has a discontinuity across each interface by an amount $|\vec{E}_1^\perp|/|\vec{E}_2^\perp| = \varepsilon_2/\varepsilon_1$, where ε_1 and ε_2 are the permittivities of each material.

As shown in Figure 2.4(a), at the gold/dielectric interface a plasmonic enhancement of 3.19 is obtained, which attenuates to a value of 0.84 at the cobalt/dielectric interface. As seen in Figure 2.4(a), the spacing between gold and cobalt is 300 nm, which has a larger value than the coupling length. Thus, evanescent coupling between gold and cobalt is weak. Although large gold-cobalt spacing brings a low cobalt-induced damping on the plasmonic enhancement, the negative effect of a weaker evanescent coupling dominates the positive effect of a lower cobalt-induced damping on the enhancement. Therefore, the intensity enhancement decays to 0.84 on the cobalt surface. As shown in Figure 2.4(b), when gold-cobalt spacing decreases to 176 nm, a

stronger evanescent coupling is obtained and the intensity enhancement on cobalt increases to 3.99. In addition, cobalt-induced damping also increases; however, the effect of evanescent coupling becomes larger. For this case, surface plasmons also provide higher intensity values on the cobalt surface because they are at resonance. Nevertheless, surface plasmons can provide higher intensities because a strong evanescent coupling is present between gold and cobalt. As shown in Figure 2.4(c), plasmonic enhancement on gold is lower than other cases, since cobalt-induced damping is higher due to smaller spacing of 50 nm. Although the spacing is smaller than the coupling length, cobalt-induced damping dominates. An additional effect occurs for the field localization when gold and cobalt layers are closely located. Cobalt and gold films act as absorptive claddings for plasmonic waveguide modes, which localize the field in the dielectric layer as demonstrated in Figure 2.4(c). Plasmonic enhancement in Figure 2.5 is higher compared to Figure 2.4(b), but the intensity enhancement on cobalt is lower, since cobalt-induced damping is higher due to smaller gold-cobalt spacing.

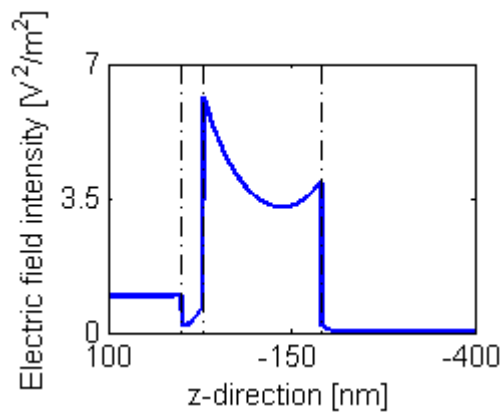


Figure 2.5 Electric field intensity profile for a gold thickness of 30 nm and a dielectric thickness of 160 nm. The operation wavelength is 633 nm.

2.3 Zero Reflection Multilayers

In this section, load-induced and radiative losses in multilayer configurations with zero reflectivity are discussed, and various multilayers that have minimized losses are specified. As shown in Figure 2.6 and Figure 2.7, each enhancement value corresponds

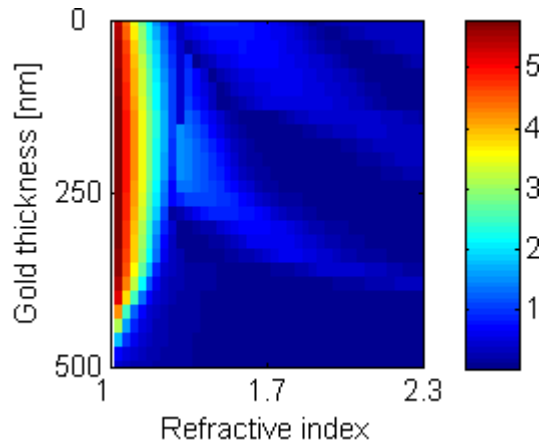


Figure 2.6 Intensity enhancement at the cobalt/dielectric interface as a function of the thickness and refractive index of the dielectric layer. The thickness of the gold layer is different for each multilayer configuration to obtain maximum intensity enhancement. The operation wavelength is 633 nm.

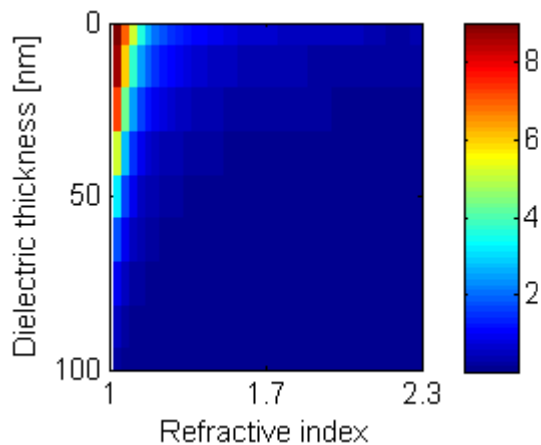


Figure 2.7 Intensity enhancement at the cobalt/dielectric interface as a function of gold thickness and refractive index of the dielectric layer. The thickness of the dielectric layer is different for each multilayer configuration to obtain maximum intensity enhancement. The operation wavelength is 633 nm.

to a specific multilayer that has zero reflectivity. Thus higher intensity values are obtained on cobalt.

Intensity enhancement at the cobalt/dielectric interface as a function of the thickness of the dielectric layer is presented in Figure 2.6. As shown in Figure 2.6, plasmonic enhancement increases to 5.8 when gold-cobalt spacing increases to 280 nm, since cobalt-induced damping on surface plasmons at the gold/dielectric interface

decreases. In addition, radiative loss due to quartz decreases as the dielectric thickness increases because the quartz layer gets further away from the cobalt/dielectric interface, which contributes to the enhancement. As the dielectric thickness further increases, a lower enhancement is obtained due to the lower interaction between the evanescent tail of surface plasmons and cobalt. Furthermore, as the refractive index increases to $n = 1.2$, the intensity enhancement decreases to 4.2, since the perpendicular field component on the dielectric at the gold/dielectric interface has a lower magnitude for a higher refractive index. When the gold thickness gets smaller radiative loss increases because the distance between the dielectric/cobalt and quartz/gold interface decreases. On the other hand, surface plasmons are near their resonance point, and the positive effect of intensity enhancement dominates the negative effect of radiative loss, and the intensity increases to 8.7. As a result, multilayers that have a relatively higher intensity enhancement due to minimized losses, as well as a smaller dielectric thickness correspond to a dielectric thickness between 80-100 nm, which provide intensity enhancements between 5.18-5.5

2.4 Conclusion

In conclusion, various multilayer configurations of gold-cobalt films were investigated to increase the performance of integrated recording heads. Optimum configurations were identified for minimum radiation loss and load-induced damping due to the magnetic film. It was demonstrated that a higher intensity enhancement on cobalt is obtained when evanescent coupling is stronger and load-induced damping is lower. It was shown that load-induced damping dominates evanescent coupling when gold and cobalt are much closer than the coupling length.

3 INVESTIGATING THE RELIABILITY AND PERFORMANCE OF HAMR INTEGRATED HEADS VIA MULTILAYER CONFIGURATIONS

3.1 Weakening and Losing Plasmon Resonances in the Presence of Magnetic Layers

Free-standing plasmonic nanostructures and plasmonic layers may provide very high intensity enhancements due to surface plasmon resonances when plasmon resonances are excited at their resonance point. When near or integrated with a lossy medium however, they may be exposed to several losses that are as a result of the material properties of the adjacent medium. Due to these losses the plasmonic enhancements may be weakened. A proper example can be given for a HAMR system. In a HAMR integrated head, a plasmonic nanotransducer is integrated with a magnetic head. The plasmonic enhancement from the nanotransducer weakens in the presence of the magnetic head. The intensity enhancement is yet high that enables HAMR recording; however, it is weakened.

In some other cases, surface plasmons cannot be excited on nanostructures or at an interface between two media, and very low intensity enhancements may result due the lack of plasmon resonances. In this section, prior to investigating the weakening of plasmon resonances in the subsequent sections, the existence of plasmon resonances between a gold layer as and cobalt layer is investigated as illustrated in Figure 3.1, and possible outcomes of the results are explained.

Surface plasmons that are excited at an interface between two media posses a parallel and normal component of their wavevector. The parallel component of the wavevector as a function of the angular frequency can be expressed as,

$$k_x = \sqrt{\frac{\varepsilon_1 \varepsilon_2}{\varepsilon_1 + \varepsilon_2}} \frac{\omega}{c} \quad (3.1)$$

and the normal component of the wavevector can be expressed as

$$k_{j,z} = \frac{\varepsilon_j}{\sqrt{\varepsilon_1 + \varepsilon_2}} \frac{\omega}{c} \quad (3.2)$$

where ε_j is the dielectric function of the corresponding medium j where $j = 1, 2$. Taking into account the wavevector expressions, surface plasmons can be excited under the fulfillment of two conditions. Firstly, they should propagate along an interface to exhibit a wave character and therefore the parallel component of the wavevector in Equation (3.1) should be real. This is possible if the denominator and numerator of Equation (3.1) is either positive or negative. Secondly, surface plasmons should decay exponentially from the interface in both media because they are bound electromagnetic waves that provide enhancement values that are higher at the interface. This means an imaginary value for the normal component of the wavevector in Equation (3.2). A negative value for the denominator in Equation (3.2) makes this possible. Consequently, the following relations ensure the existence of surface plasmons,

$$\begin{aligned} \varepsilon_1 \varepsilon_2 &< 0 \\ \varepsilon_1 + \varepsilon_2 &< 0 \end{aligned} \quad (3.3)$$

For the case in Figure 3.1, where a cobalt layer is adjacent to a gold layer, the plasmon excitation conditions in Equation (3.3) cannot be fulfilled, since the real part of the dielectric function of gold and cobalt is both negative for various wavelengths, as depicted in Figure 3.2. As seen in Figure 3.3, for a high-index/gold/dielectric (h-g-d) multilayer with a gold thickness of 50 nm, a well-defined plasmon resonance curve is obtained. However, the resonance curve is broadened in the presence of a cobalt layer in a high-index/gold/cobalt (h-g-c) multilayer. The dip of the reflectivity curve shifts from 60.32° to 60.33° , and the reflectivity value drastically increases from 0.002 to 0.849. The electric field intensity profiles of the h-g-d and h-g-c multilayers are depicted in Figure 3.4. As shown in Figure 3.4, at the gold interface the intensity

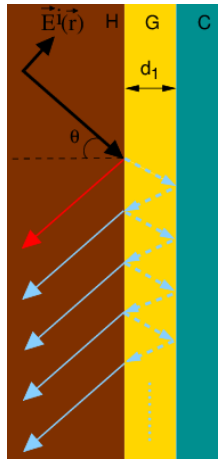


Figure 3.1 Schematic illustration of a three-layer multilayer with a gold thin-film adjacent to a cobalt thin-film. The thickness of the gold layer is d_1 .

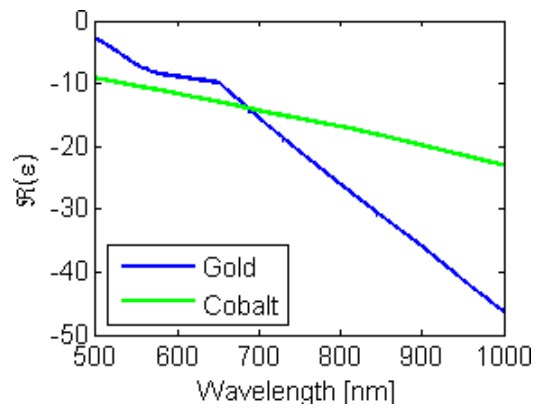


Figure 3.2 Real part of the dielectric functions of gold and cobalt as a function of wavelength.

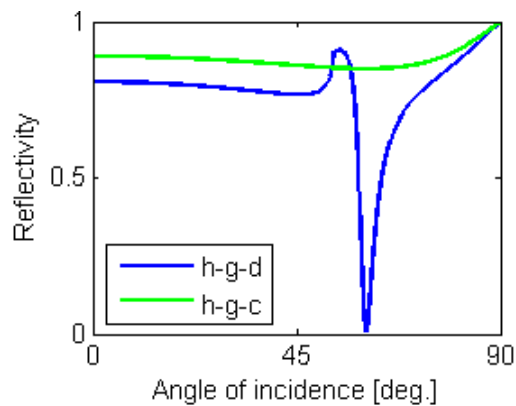


Figure 3.3 Reflectivity as a function of the angle of incidence. h-g-d denotes the High-index/Gold/Dielectric multilayer, and h-g-c denotes the High-index / Gold / Cobalt multilayer. The incident wavelength is 633 nm.

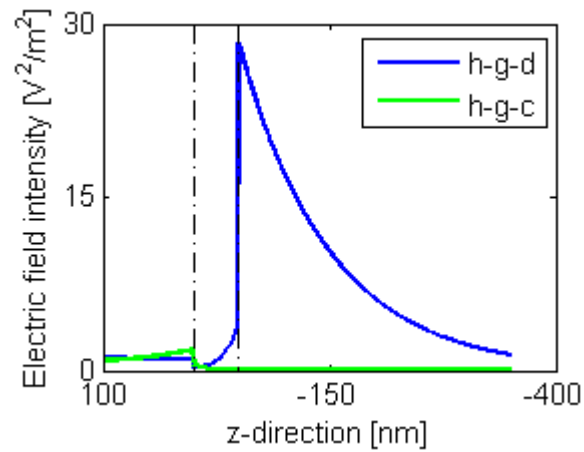


Figure 3.4 Electric field intensity profiles of various layers that laminated on the gold layer. The incident wavelength is 633 nm.

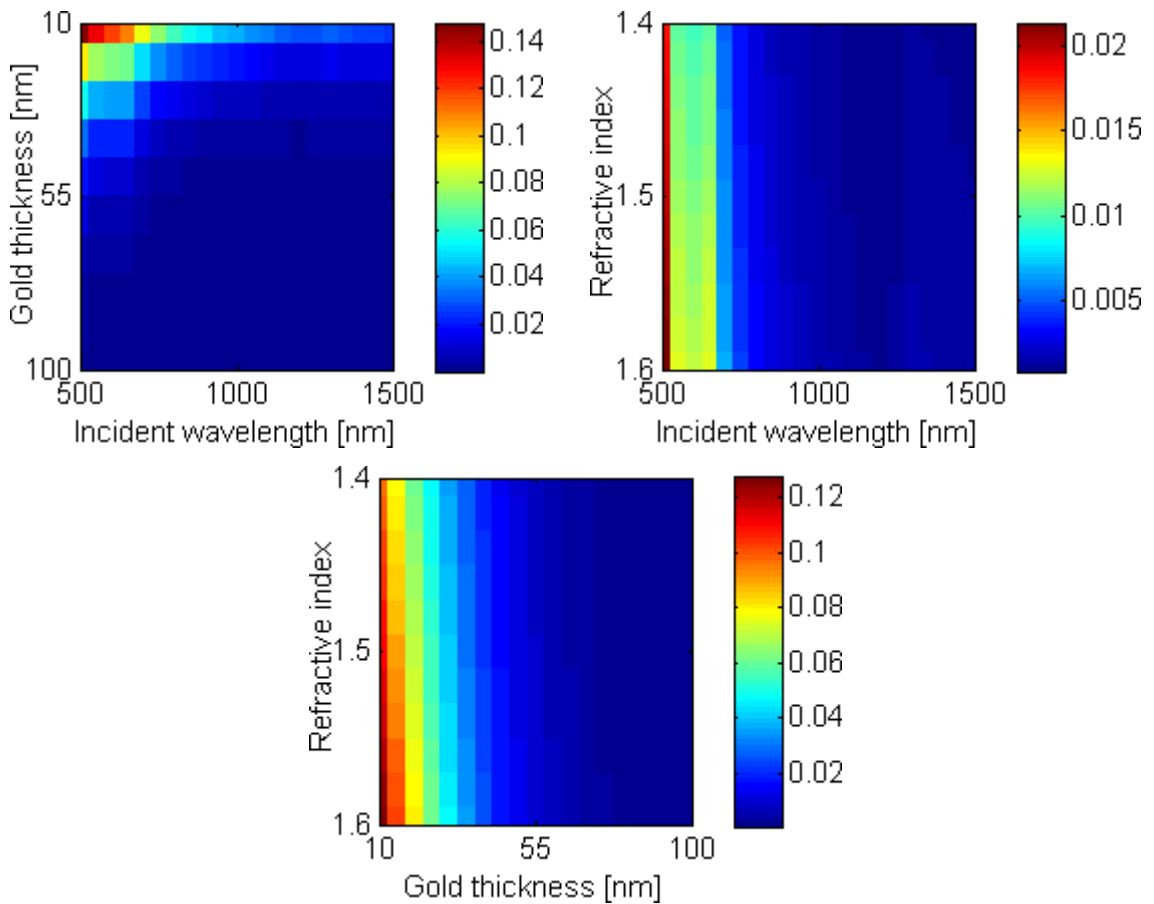


Figure 3.5 Intensity values at the gold-cobalt interface as a function of incident wavelength, gold thickness, and refractive index of the high-index medium. The wave amplitude of the incident wave is selected as 1 V/m.

enhancement drops from 28.37 to 0.01. As illustrated in Figure 3.5, plasmon resonances cannot be recovered back by adjusting the incident wavelength, gold thickness, and refractive index of the high-index medium.

3.2 Recovering the Intensity Enhancement and Plasmon Resonances via Thin-Film Coatings

In a HAMR system, the magnetic grains of the recording media are locally heated by a nanoscale optical spot in order to reduce the coercivity of the magnetic grains. In a HAMR system, the nanoscale optical spot is produced by a plasmonic nanotransducer that is integrated with a magnetic head. In order to reduce the coercivity value to a lower value compared to the head field value in a few nanoseconds, the electric field intensity and field gradients from the nanotransducer must be sufficiently high in the presence of the magnetic head. However, plasmon resonances of nanotransducers get weakened near magnetic heads. Therefore, the weakened plasmon resonances that are produced by thin gold films in multilayers in the presence of cobalt layers may be investigated to find out how the plasmon resonances can be recovered back in an integrated magnetic head.

For this purpose, a thin-film gold coating with a thickness of 30 nm is laminated between the cobalt and a dielectric layer, which forms a high-index / gold / dielectric / gold / cobalt (h-g-d-g-c) multilayer, as illustrated in Figure 3.6. As shown in Figure 3.6, the reflectivity curve is recovered back, which has a dip at an incident angle of 72.21°. The electric intensity profile of the h-g-d-g-c multilayer is shown in Figure 3.8. It can be seen that the intensity has a higher value at the middle of the dielectric layer and at the dielectric/cobalt interface of 5.0 and 8.8, respectively.

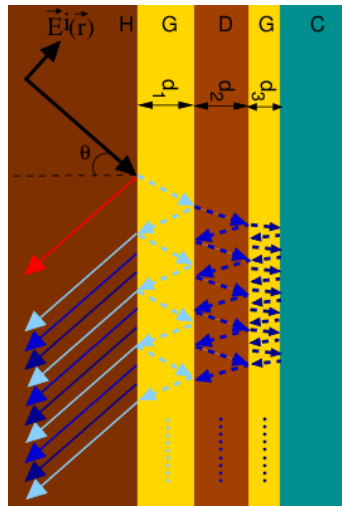


Figure 3.6 Schematic illustration of a five-layer multilayer with a gold thin-film near a cobalt layer. The red arrow illustrates the primary reflections from the H-G interface. The light blue, blue, and dark blue arrows represent the reflections from the G-D, D-G, and G-C interfaces, respectively. The thickness of gold and dielectric layers is d_1 , d_2 , and d_3 .

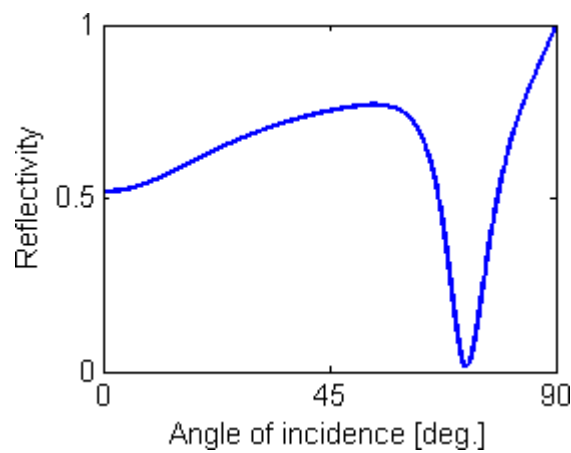


Figure 3.7 Reflectivity as a function of the angle of incidence for a high-index / gold / dielectric / gold / cobalt multilayer. The thickness of the gold layers is 30 nm, and the dielectric layer is 176 nm.

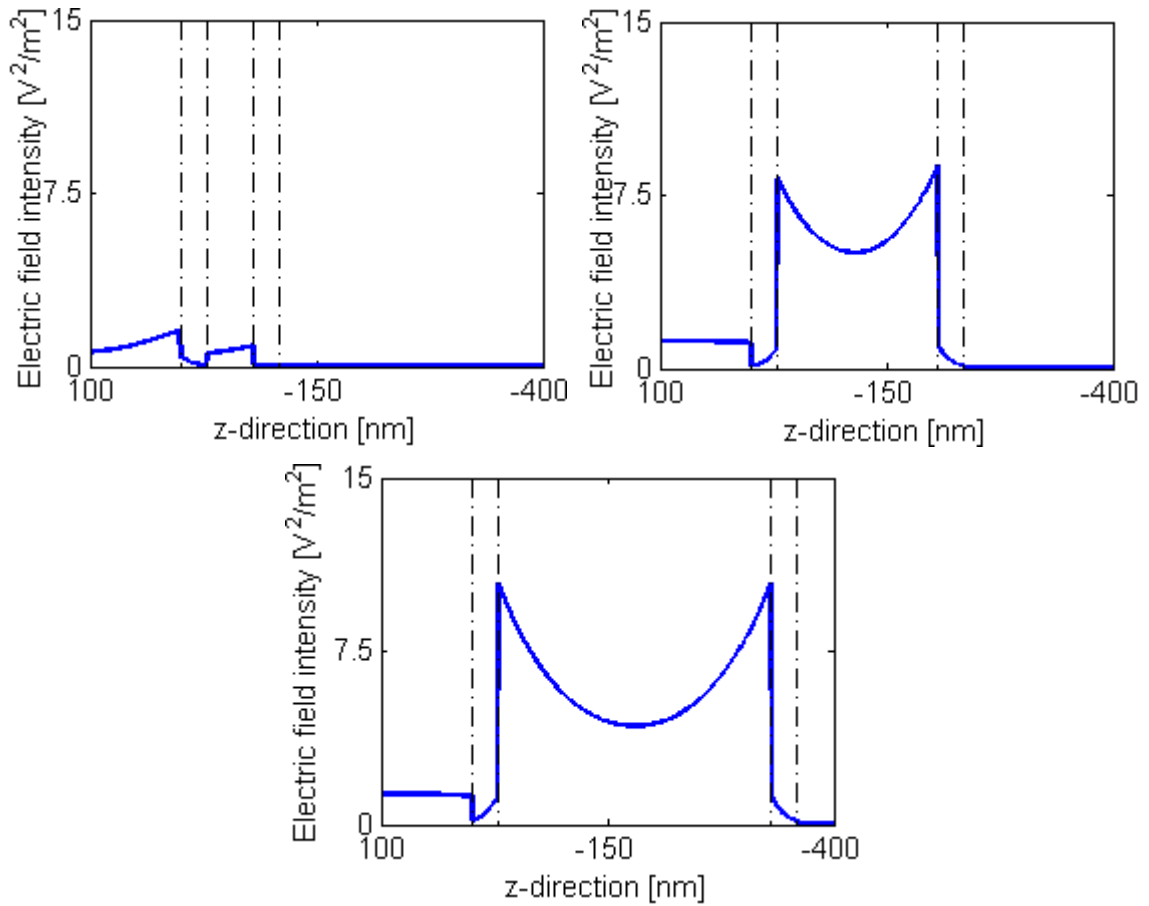


Figure 3.8 Electric field intensity profiles of various multilayers with a dielectric thickness of (a) 300 nm, (b) 176 nm, and (c) 50 nm. The thickness of the gold layer is selected as 30 nm. Refractive index of the dielectric layer is $n = 1.2$. The operation wavelength is 633 nm.

3.3 Improving Optical Field Intensities and Optical Field Gradients to Facilitate HAMR Recording

HAMR is a promising technique to extend the areal density of hard drives beyond that of conventional recording techniques [66,67]. In HAMR, localized optical spots that are produced by integrated heads are utilized to heat the magnetic medium during the recording process [68-70]. The coercivity of the magnetic grains can therefore be lowered by optical spots during the recording process below the available head field. The localized optical spots create the high field gradients that enable high write field gradients during the recording process [66,71,72]. The field gradient at the recording point specifies the quality of the written transitions [73]. In addition to several other

technical challenges [74,79], an effective engineering of the field gradients in a HAMR system is therefore a crucial issue.

Recently, several studies in the literature have focused on the field-gradient aspects of HAMR [72,73,80]. An experimental technique is developed to measure the thermal gradient in down-track and cross-track directions. The effect of the heat-sinking of the media is specified, and it is shown that the thermal gradient increases due to the strong heat-sinking of the media [72]. Furthermore, a thermal William-Comstock model is utilized to predict the transition length in a HAMR system. The transition length is minimized by specifying an optimal alignment between the thermal profile and the magnetic head [73]. A micromagnetic recording model is utilized to study the effect of thermal and field-gradient alignment in HAMR by varying the separation between the thermal spot and the leading edge of the head field [80].

Since the field gradient specifies the quality of the written transitions, a higher field gradient of the optical spots is desired. It is therefore important to identify head configurations that will positively impact the field gradient. In this study, we propose an additional thin plasmonic coating layer on top of magnetic heads, which minimizes the interaction of the plasmonic transducer and the recording head. Figure 1 provides a schematic illustration of the proposed plasmonic layer, which appears adjacent to the magnetic head. This additional plasmonic layer isolates the plasmonic transducer and magnetic head, and therefore, eliminates the negative impact of the magnetic head on the operation of the plasmonic transducer. In this study, we demonstrate that the down-track optical field gradients are improved as a result of this additional layer. In addition, we demonstrate that the field gradients can be effectively engineered by plasmonic thin-film stack thicknesses and materials. A parametric study is performed to reach optimized conditions. The dielectric layer thickness, gold layer thickness, incident angle, and incident wavelength are utilized to tailor the field gradients in the down-track direction.

In this study, various multilayer configurations with gold thin-films near magnetic films are investigated, and optimum configurations are identified that obtain higher field gradients in the down-track direction. The thin-film stack is composed of high-

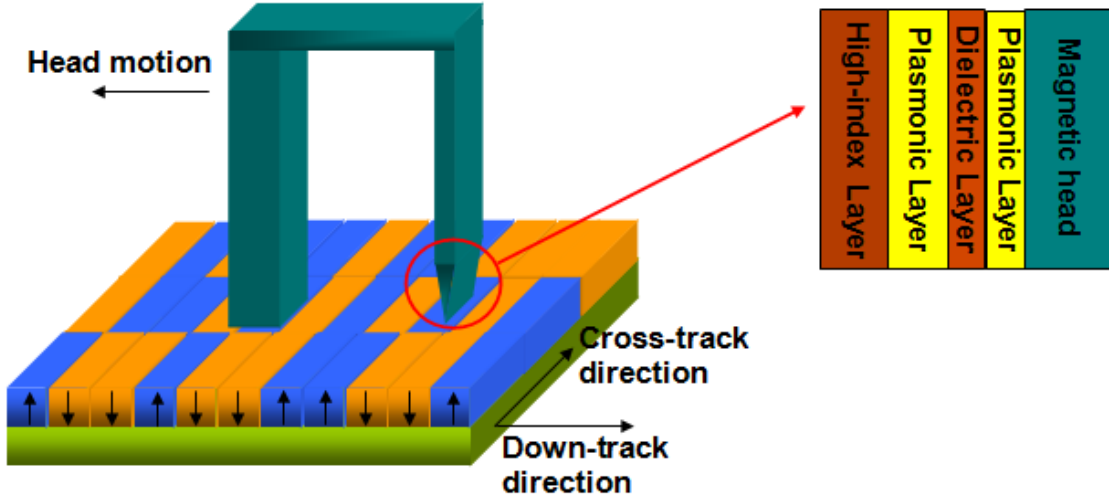


Figure 3.9 Schematic illustration of the proposed layer in an integrated head in a HAMR system. The proposed plasmonic layer is adjacent to the magnetic head, and it isolates the optical interaction of the other plasmonic layer with the magnetic head.

index/gold/dielectric/gold/magnetic-head (H-G-D-G-M) layers as shown in Figure 3.9. The plasmonic transducer is placed adjacent to the high-index layer. The gold thin-film that is adjacent to the head strengthens the plasmonic effects in the dielectric layer. A linearly polarized plane wave is incident on the quartz/gold interface. The quartz layer is chosen to increase the value of the incident wave vector to the surface plasmon wave vector in order to excite surface plasmons on the gold thin-film. The magnitude of the incident field is selected as 1 V/m in this study. Thus, the electric field intensity values that are obtained in the multilayers correspond to intensity enhancements.

3.3.1 Methodology

In this study, various multilayer configurations are investigated to optimize the field gradients by engineering them. To analyze this problem, the propagation matrix method [78, 81] is employed. The multilayer is illuminated with a linearly polarized plane wave that can be expressed as

$$\vec{E}^i(\vec{r}) = \vec{E}_0^i \exp(i\vec{k} \cdot \vec{r}) . \quad (3.4)$$

where \vec{E}_0^i is composed of tangential and perpendicular components to the quartz/gold interface. When the incident field \vec{E}^i interacts with the multilayer film, various primary and secondary reflections and transmissions occur at the interfaces that generate scattered field \vec{E}^s . The total field \vec{E}^t is the summation of the incident field \vec{E}^i and scattered field \vec{E}^s .

Considering the continuity of the tangential component of the electric field across an interface between two layers, a propagation matrix may be obtained that relates the electric field amplitudes of the total field \vec{E}^t in the quartz layer to other layers [16]. This matrix can be expressed as

$$\begin{pmatrix} E_m^r \exp(-ik_{zm}d_m) \\ E_m^i \exp(ik_{zm}d_m) \end{pmatrix} = \bar{\bar{V}}_{m(m-1)} \cdot \bar{\bar{V}}_{(m-1)(m-2)} \dots \bar{\bar{V}}_{(l+1)l} \cdot \begin{pmatrix} E_l^r \exp(-ik_{zl}d_l) \\ E_l^i \exp(ik_{zl}d_l) \end{pmatrix} \quad (3.5)$$

where E_l^i and E_m^i are the incident field amplitudes, and the sub-index denotes the layer number. E_l^r and E_m^r are the reflected field amplitudes in layer l and layer m . For $m > l$ a forward propagation matrix is obtained that relates the field amplitudes of an upper layer to a lower layer. $\bar{\bar{V}}_{(l+1)l}$ is the propagation matrix, which relates the incident and reflected field amplitudes in layer l to that in layer $l+1$. As expressed in Equation (3.5), by the multiplication of propagation matrices the electric fields in various layers can be obtained. By adding the fields in each layer, the total field \vec{E}^t is obtained.

The field gradients are then obtained by the central difference formula as

$$\frac{d|\vec{E}^t|}{dx} = \frac{d|\vec{E}^t(i+1)| - d|\vec{E}^t(i-1)|}{x(i+1) - x(i-1)} \quad (3.6)$$

where E is the value of the electric field in the dielectric layer along the down-track direction, and x is the down-track direction. The parameter i is the index of the arguments of E and x .

3.3.2 Engineering the Field Gradient

In HAMR systems, an optical spot beyond the diffraction limit is produced by a plasmonic transducer that is integrated with a magnetic head. In order to reduce the coercivity value to a lower value compared to the head field value in a few nanoseconds, the electric field intensity value and the electric field gradient value of the optical spot should be sufficiently high in the presence of the magnetic head. On the other hand, plasmon resonances of nanotransducers get weakened [78] near magnetic heads that reduce the electric field intensity enhancement, and thereby the electric field gradient values. It is crucial to find effective integrated head configuration that will minimize the negative impact of the magnetic head on the performance of the plasmonic transducer. In this section, we propose an additional plasmonic layer and investigate how the plasmon resonances can be recovered back in an integrated head.

In an integrated head, a plasmonic transducer that is in the vicinity of a magnetic head may be represented as a high-index-gold-magnetic-head (H-G-M) or high-index-gold-dielectric-gold-magnetic-head (H-G-D-M) multilayer, depending on whether the plasmonic transducer and magnetic head are separated by a dielectric layer. The dispersion relation of an H-G-M and H-G-D-M multilayer is represented in Figure 3.10. Every single pixel in Figure 3.10 corresponds to a reflectivity value. As depicted in Figure 3.10(a), there does not exist any energy band between $\lambda_{inc}=500-1000$ nm. In other words, the presence of the magnetic head in the vicinity of plasmonic transducer eliminates the plasmon resonances. Similarly, for the H-G-D-M multilayer in Figure 3.10(b), there are high and low energy bands, but for lower energies the energy band is less visible between $\lambda_{inc}=700-1000$ nm. However, the presence of the magnetic head has still a negative effect on the plasmon resonances, such that it broadens –and therefore obscures- the deep trenches of a typical plasmon resonance curve.

To alleviate the negative interaction between the magnetic head and plasmonic transducer, we propose an additional plasmonic layer next to a magnetic head. This additional plasmonic layer appears next to the magnetic head. The additional gold thin-film is laminated between the magnetic and the dielectric layer, which constitutes a

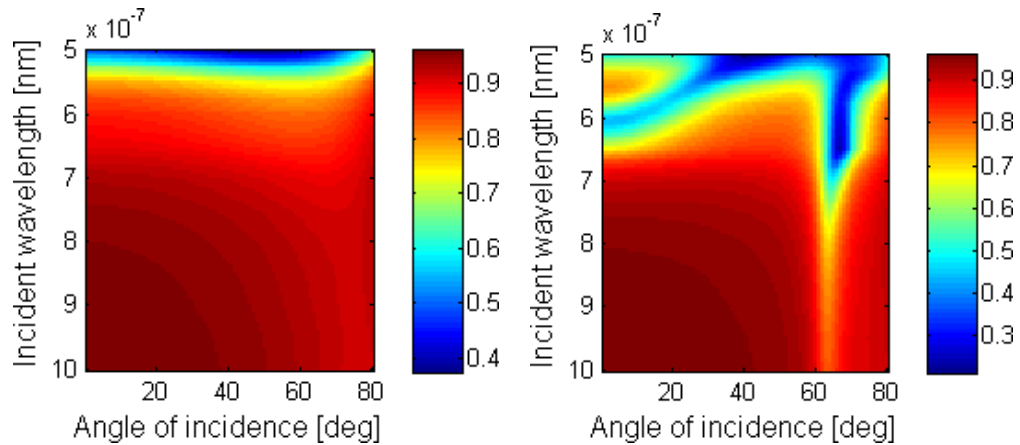


Figure 3.10 Dispersion relation of H-G-M and H-G-D-M multilayers. The thickness of the gold layer (d_1), dielectric layer (d_2), and gold layer (d_3) is selected as 50 nm, 200 nm, and 50 nm, respectively. The refractive index of the high-index layer is selected as 1.5.

H-G-D-G-M multilayer, as illustrated in Figure 3.9. The first gold layer in this multilayer depicts a plasmonic nanotransducer, and the magnetic layer depicts a magnetic head.

The dispersion relations of a H-G-D-G (MIM configuration) and the H-G-D-G-M multilayer are shown in Figure 3.11. As seen in Figure 3.10, there exists a high energy and a low energy band for the H-G-D-G and H-G-D-G-M configuration and the dispersion relation of the configurations are very similar. By comparing Figure 3.10 and Figure 3.11, it is obvious that the lost high-quality plasmonic resonances are recovered by an additional plasmonic layer in the H-G-D-G-M configuration. Furthermore, similarity of the H-G-D-G and H-G-D-G-M configurations show that the presence of the magnetic head does not negatively impact the performance of the plasmonic transducer. It can be concluded that the addition of a magnetic layer has minimum effect on the dispersion relation of the H-G-D-G multilayer. Thus, surface plasmons in an H-G-D-G-M multilayer show almost the same behavior as in an H-G-D-G multilayer.

The underlying physical mechanism for the improved performance due to the addition of the laminated plasmonic layer next to the magnetic head can be explained as follows: In Figure 3.16, for larger incident wavelengths more of the incident light is reflected back to the high-index layer for the H-G-M and H-G-D-M multilayers

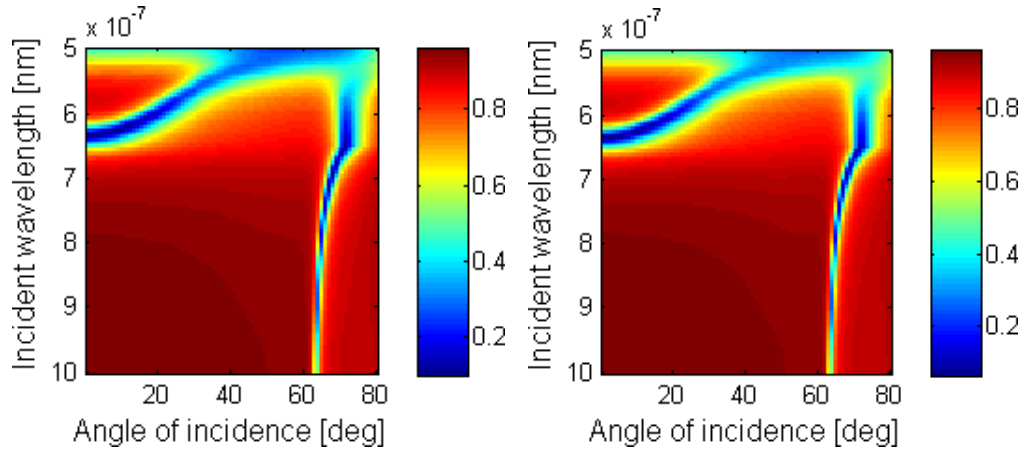


Figure 3.11 Dispersion relation of H-G-D-G (MIM configuration) and H-G-D-G-M multilayers. The thickness of the gold layer (d_1), dielectric layer (d_2), and gold layer (d_3) is selected as 50 nm, 200 nm, and 50 nm, respectively. The refractive index of the high-index layer is selected as 1.5.

compared to the H-G-D-G-M multilayer in Figure 3.17. Thus, the plasmonic enhancement on the G-D interface is higher for the H-G-D-G-M multilayer at longer wavelengths. Therefore, higher field gradients can be obtained at these wavelengths. The reason for adding a second gold layer between the dielectric and magnetic layer is similar to obtain a metal-insulator-metal (MIM) waveguide [82] within the multilayer. The second gold layer enables the recovery of the surface plasmon waves on the gold surfaces due to the strong coupling between the two gold layers. Therefore, a higher intensity enhancement is obtained, as well as a higher field gradient.

The field gradient in the down-track direction of the H-G-D-G-M multilayer is shown in Figure 3.18. As shown in Figure 3.12(a), when the dielectric spacing thickness increases to 176 nm the value of the optical field gradient increases at the D-G interface. In addition, the field gradient value is also higher at center of the dielectric layer compared to other cases. When the gold thickness is 70 nm as shown in Figure 3.18(b), the field gradient is higher both at the boundaries and at the center of the dielectric. The field gradient value is higher at an incident wavelength of 633 nm as shown in Figure 3.18(c) because surface plasmons are at resonance. The value of the intensity gradient increases within the dielectric layer when the incident angle varies to 72° as shown in Figure 3.18(d), which is the surface plasmon resonance angle for the multilayer configuration. Furthermore, when surface plasmons are excited

on the gold films, the intensity gradient has a maximum and minimum value at the G-D and D-G interface, respectively.

The electric field intensity gradient values for different system parameters are presented in Figure 3.19. The optimum system parameters that yield a higher field gradient in Figure 3.13(a) can be given for a gold thickness $d_1=34$ nm and a dielectric thickness $d_2=200$ nm. In Figure 3.13(b) the optimum parameters are for a gold thickness $d_3=100$ nm. The refractive indices that yield a higher field gradient in Figure 3.13(c) are $n_0=1.42$ and $n_2=1.98$. In Figure 3.13(d) the optimum wavelength is given as $\lambda_{inc}=1180$ nm.

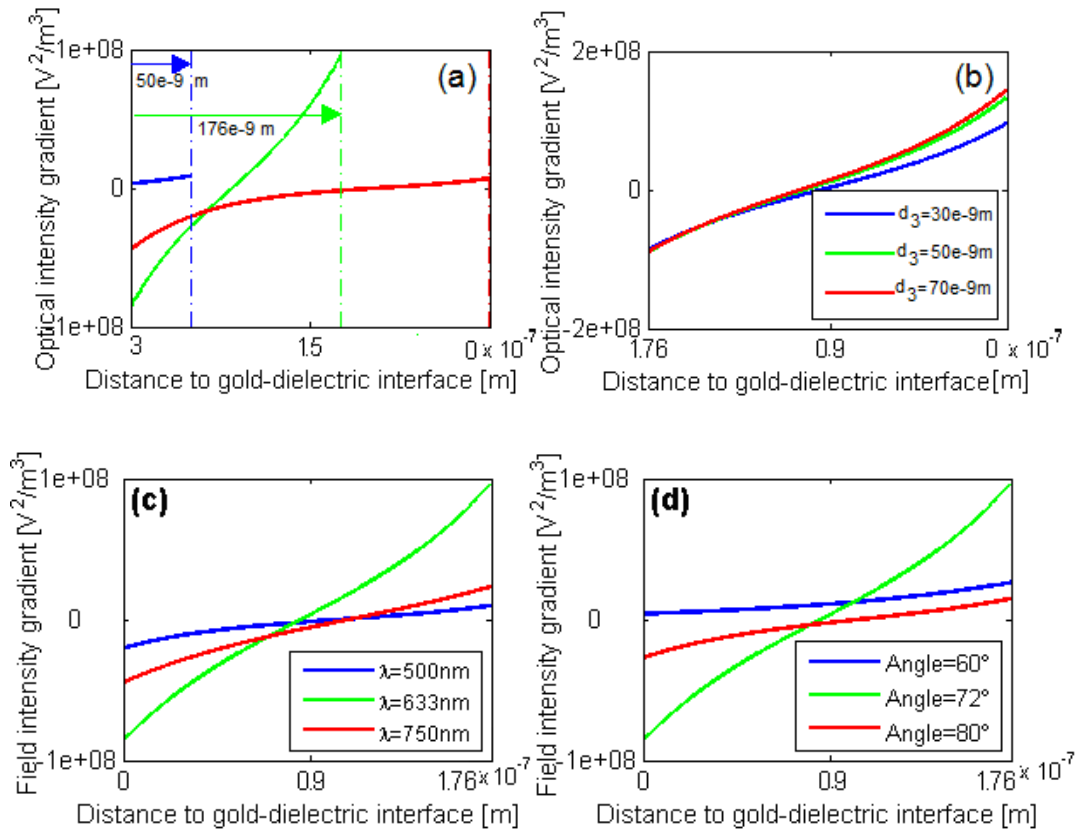


Figure 3.12 Electric field intensity gradient profiles in the dielectric layer as a function of (a) the dielectric thickness, (b) gold thickness, (c) incident wavelength, and (d) incident angle. The gold thickness (d_1), and dielectric thickness (d_2), and gold thickness (d_3) is 30 nm, 176 nm, and 30 nm, respectively for (a) and (b). The refractive index of the high-index layer is selected as 1.5.

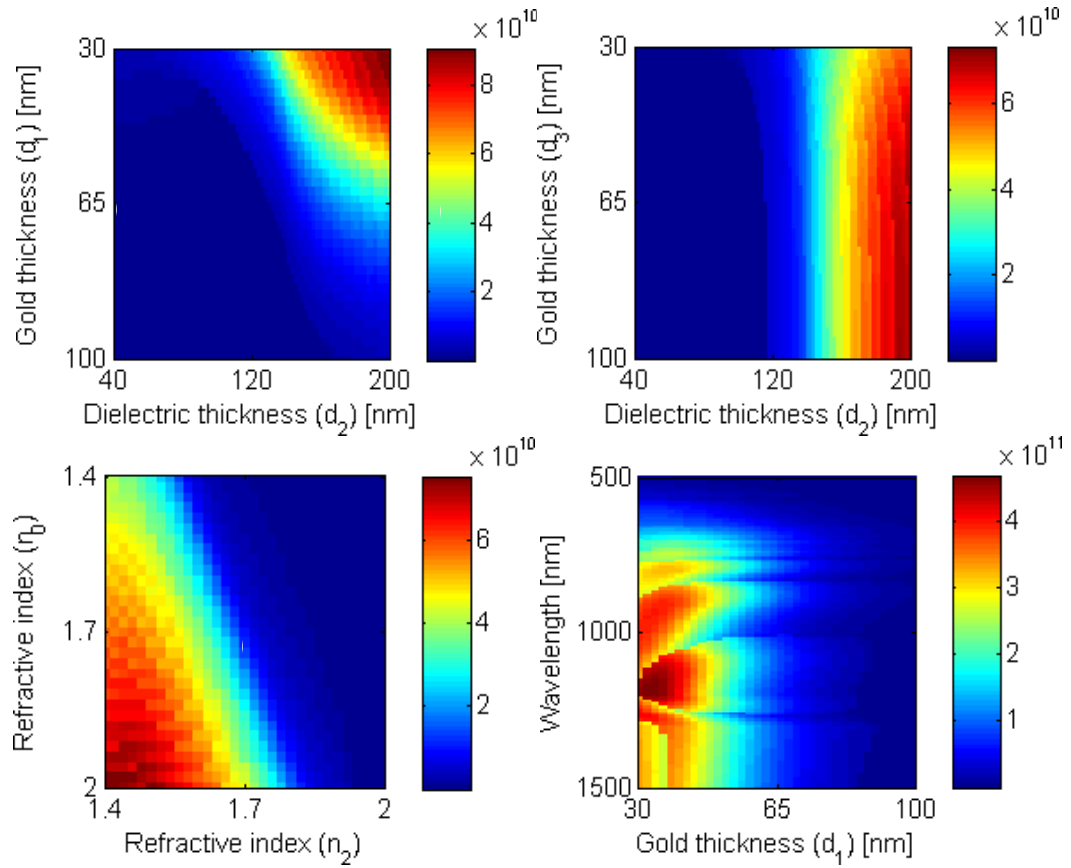


Figure 3.13 Electric field intensity gradient values as a function of the (a) dielectric thickness (d_2) and gold thickness (d_1), (b) dielectric thickness (d_2) and gold thickness (d_3), (c) refractive indices n_0 and n_2 , and (d) gold thickness (d_1) and incident wavelength.. The thickness of the gold layer (d_1), dielectric layer (d_2), and gold layer (d_3) is selected as 50 nm, 200 nm, and 50 nm, respectively. The refractive index of the high-index layer is selected as 1.5.

Internal damping of the H-G-D-G-M multilayer is represented in Figure 3.14. Internal damping is defined as the ratio of the dissipated power in the gold and cobalt layers to the incident power. Thus, it provides a percentage of the dissipated power in the gold and magnetic layers. For the regions where the field gradient are higher in Figure 3.13, the internal damping of the multilayer is also higher, as seen in Figure 3.14. These results indicate that the load-induced damping of the plasmonic resonances are the dominant loss mechanism, and the internal damping does not play a significant role in determining the optimal conditions.

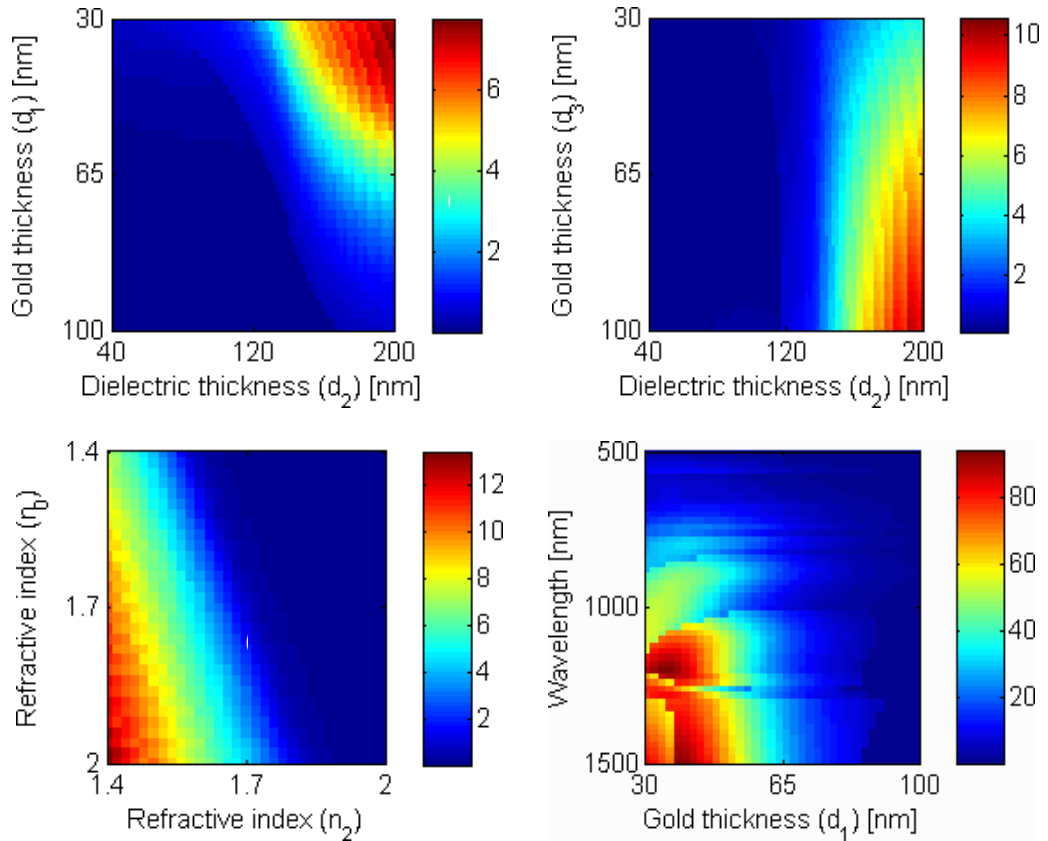


Figure 3.14 Internal damping of the H-G-D-G-C multilayer as a function of various system parameters.

In summary, an additional thin plasmonic coating layer on top of magnetic heads is proposed to improve the field gradients in HAMR. This additional plasmonic layer minimizes the interaction of the plasmonic transducer and the recording head. In addition, this additional plasmonic layer isolates the plasmonic transducer and magnetic head, and therefore, eliminates the negative impact of the magnetic head on the operation of the plasmonic transducer. It was shown that this integrated head configuration can provide higher field gradients for longer incident wavelengths. In addition optimum configurations that yield higher field gradients regions in the down-track direction are identified.

3.4 Predicting and Minimizing the Wavevector Shift in Dispersion Curves

Free-standing plasmonic structures, such as gold thin-films on a high-index layer as in the Kretschmann configuration, which is illustrated in Figure 3.15, present a well-defined reflectivity curve for surface plasmons as shown in Figure 3.16. On the other

hand, when various other layers, such as gold, dielectric and cobalt layers are laminated on the gold film, the dip of the reflectivity curve shifts to other angles and the reflectivity curve broadens as illustrated in Figure 3.16. As a result of this shift, surface plasmons are excited at a different operation point compared to the Kretschmann geometry, and therefore exhibit a lower plasmonic enhancement than the Kretschmann configuration. This shifting effect is especially crucial in HAMR, where the resonance point of a plasmonic nanotransducer is shifted to other wavelengths or incident angles near a magnetic head, thus exhibit a lower plasmonic intensity enhancement compared to its plasmonic enhancement in the absence of the magnetic head.

In this section, the shift of the dispersion curves of surface plasmons in a multilayer stack are predicted and engineered so that the shift is minimized. A high-index/gold/dielectric/gold/cobalt multilayer stack is investigated, as illustrated in Figure 3.6. As shown in Figure 3.16(a) the dip of the reflectivity curves shift from 60.33° to 72.21° in the presence of a gold layer and magnetic layer. By increasing the refractive index of the high-index layer from $n=1.5$ to $n=2$, the dip of the reflectivity curve shifts

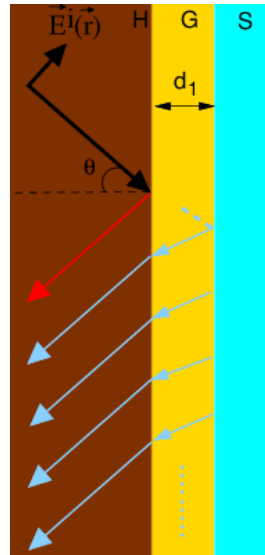


Figure 3.15 Schematic illustration of a three-layer multilayer with a gold thin-film that is laminated on a high-index layer. The thickness of the gold layer is d_1 .

to smaller angles as depicted in Figure 3.17(a). Furthermore, when $n=1.655$, the reflectivity dip has an angle of 60.37° , and the shift is minimized. As illustrated in Figure 3.17(b), the plasmonic enhancement at the D-G interface has a value of 14.1,

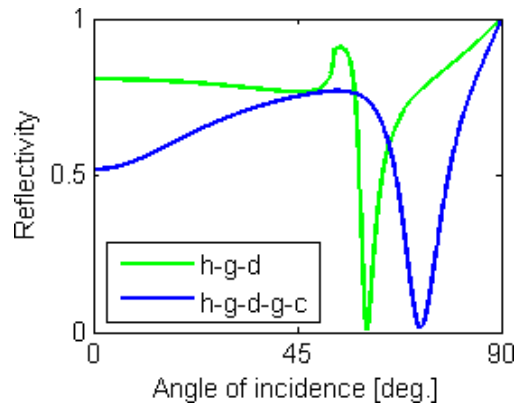


Figure 3.16 Reflectivity as a function of the incident angle for a three layer H-G-D and five layer H-G-D-G-C configuration.

which is higher than that in Figure 3.8. The effect of the dielectric index on the amount of shift is represented in

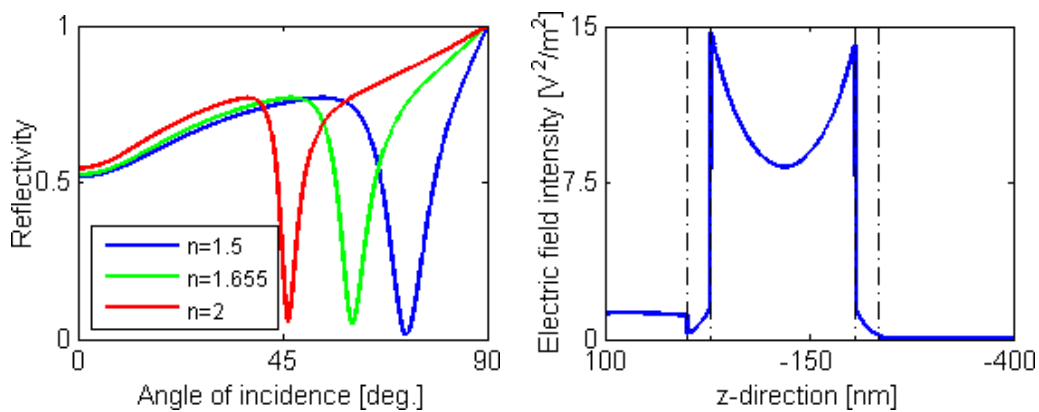


Figure 3.17(a) Reflectivity as a function of the refractive index of the high-index layer, and (b) electric field intensity profile for $n=1.655$.

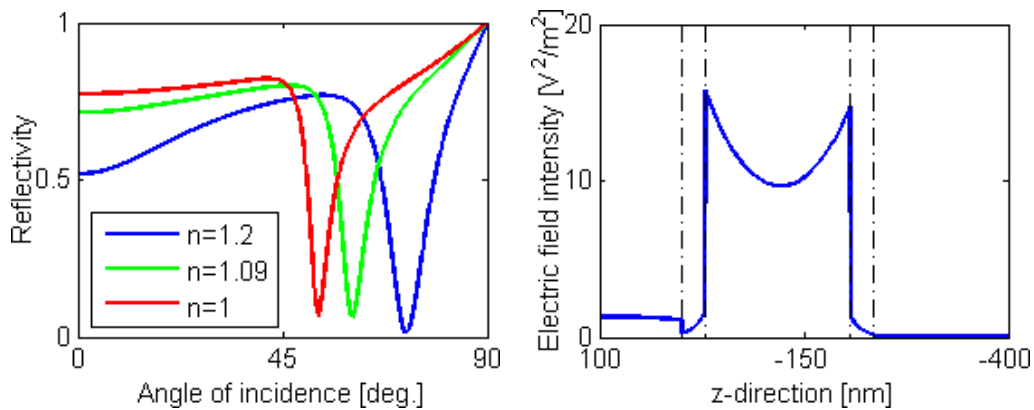


Figure 3.18 Reflectivity as a function of the dielectric index, and (b) electric field intensity profile for $n=1.09$.

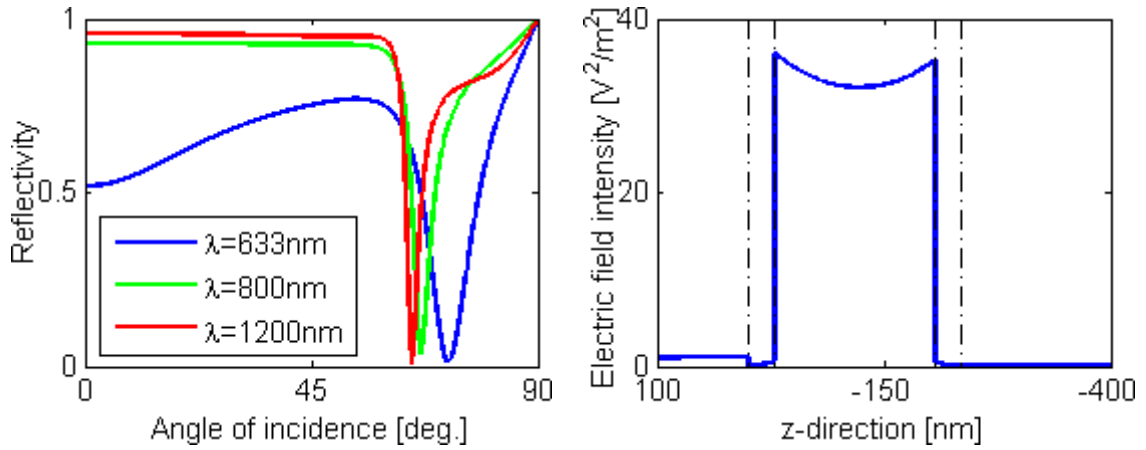


Figure 3.19 Reflectivity as a function of the incident wavelength, and (b) electric field intensity profile for $\lambda=1200\text{ nm}$.

Figure 3.18. As the refractive index varies from $n=1.2$ to $n=1$ the reflectivity curve shifts to smaller angles. When $n=1.09$ the dip angle has a value of 60.33° . The plasmonic enhancement at the D-G interface, which is shown in Figure 3.18(b), has a value of 14.76. In Figure 3.19, the incident wavelength is also considered and varied between 633 nm and 1200 nm. For 1200 nm, the reflectivity dip varied to smaller angles and obtained a value of 64.96° . The plasmonic enhancement increases at the D-G interface and obtains a value of 35.99.

3.5 Conclusion

In conclusion, various multilayer configurations of with gold thin-films near cobalt were investigated to increase the performance of integrated recording heads. Optimum configurations were identified for minimum radiation loss and load-induced damping due to the magnetic film. It was demonstrated that a higher intensity enhancement on cobalt is obtained when evanescent coupling is stronger and load-induced damping is lower. It was shown that load-induced damping dominates evanescent coupling when gold and cobalt are much closer than the coupling length

Furthermore, the field gradient in the down-track direction was engineered for various configurations. It was shown that the gradient value varies with dielectric thickness, gold thickness, incident angle, and incident wavelength. Optimum values for these parameters were specified. It was also demonstrated that field gradient has a

maximum and minimum value at the interfaces of the dielectric, and passes through a nearly zero value in between at the center. The wavevector shift was also predicted and minimized in multilayer configurations. It was shown that a higher dielectric index and a lower value for the index of the high-index layer resulted in a shift of the reflectivity dip to smaller incident angles. In addition, it was shown that an increase in the incident wavelength shifted the reflectivity dip to smaller incident angles.

4 PLASMONIC PLANAR SOLID IMMERSION MIRROR (PLASMONIC PSIM)

4.1 Introduction

In the literature, near-field optical systems have been investigated due to their ability to provide small optical spots. They have been successfully used in near-field optical scanning microscopes for imaging particles with sizes below the resolution limits of optical lenses. Despite their heavy utilization in near-field imaging systems, near-field optical systems have not been used in other potential applications, such as data storage devices. This is mainly due to their size, large body mass, high price, and difficulty in manufacturing them in the large quantities required by these applications. Solid immersion lenses, apertures on metals, bow-tie antennas, ridge waveguides, tapered optical fibers, apertureless near-field techniques are among the possible ways to achieve intense optical spots with small sizes. These near-field techniques can be combined to further improve the performance. For example a bow-tie nano-antenna can be placed at the focus of a solid immersion lens to obtain better transmission efficiency with a small optical spot. However, such a device has a number of disadvantages. Some practical applications, such as magneto-optical recording, require a small body mass since the optical device will be mounted on a slider. Therefore, an optical lens system with a massive solid immersion lens is not feasible. In addition, the cost of such an optical system is quite high, since it uses traditional lens manufacturing, such as grinding and polishing.

Thin film waveguides with planar lenses, mirrors, and nano-optical transducers hold promise to address these concerns. The body mass is small and they can be easily mounted on a slider. They can be mass-produced at low costs with lithographic and thin film deposition techniques known from modern integrated circuit processing. These techniques are compatible with the current manufacturing techniques of potential

applications, therefore, they can be manufactured at the current manufacturing facilities. Thin film structures can make advanced optical devices more accessible to consumer electronics and research tools due to reduced cost. In addition, thin films provide a small body mass compared to traditional lenses, which makes some applications more feasible. A design that provides high transmission efficiency will be a major breakthrough to bring nano-optical devices into these applications. The need for highly efficient nano-optical systems has been increasing as the current technologies are approaching to their limits.

Light can be highly confined in one dimension within planar dielectric thin film waveguides. The simplest planar waveguide consists of a high index dielectric core laminated on both sides with lower index claddings. A large difference between the refractive indices of the core and cladding is desirable to provide the highest degree of confinement of the light energy within the waveguide. The thickness of the core layer also determines the degree of confinement. To confine the light in the other dimension, optical lenses and mirrors on the waveguide are necessary. Using lithographic techniques, micro-optical structures consisting of planar versions of lenses and mirrors can be etched over the planar waveguide. These lenses and mirrors can effectively confine and focus a propagating beam of light with high optical transmission efficiency into a spot smaller than the wavelength of incident light. The light confined with these planar lenses and mirrors will still be limited by the diffraction limit. To further improve the optical resolution, a nano-optical transducer can be used. A nano-optical transducer can be placed at the focus of these planar mirrors and lenses to provide smaller optical spots for better resolution. A thin film waveguide with planar optical lenses having a nano-optical transducer at the focus can address the practical issues of different applications. Such a system can be mass-produced with lithographic and thin film deposition techniques known from modern integrated circuit processing.

Especially two specific planar micro-transducers gain interest in the literature to obtain diffraction-limited optical spots: A planar solid immersion mirror (PSIM), and a planar solid immersion lens (PSIL). These micro-transducers are also utilized with nano-transducers to produce optical spots beyond the diffraction limit. A PSIM is a two-dimensional three-layer dielectric waveguide having a truncated parabolic geometry. It can obtain a diffraction-limited optical spot with a dimension that is about a quarter

wavelength of an incident light $\sim \lambda_{\text{inc}}/4$ [1]. The focal point of the PSIM is at the center of the truncated part as shown in Figure 4.1 and Figure 4.2(a). This planar dielectric structure consists of a high index dielectric core region that is sandwiched between lower index cladding regions as seen in Figure 4.2(b). Due to the specific geometry of the PSIM an optical spot is obtained at the focus by two physical means: (a) A dielectric slab waveguide confines an incident light in the direction that is perpendicular to the plane of the waveguide. A field confinement in the waveguide core is in the direction perpendicular the plane of the waveguide, and (b) Waveguide modes that reflect from the parabolic edges on either sides of the waveguide propagate to the focal point of the parabola. A confined field via the parabolic edge is in the direction that is parallel to the plane of the waveguide. Therefore, a two-dimensional field confinement may be achieved by a PSIM. For an incident wavelength of $\lambda_{\text{inc}}=413$ nm, a full-width at half-maximum (FWHM) spot size of 90 nm is obtained [83]. The reason for a field confinement by a PSIM with relatively small FWHM spot size is due to its high numerical aperture. Another reason is that a PSIM is free of chromatic aberration, hence all light rays entering it are incident on the focal point.

To demonstrate a PSIM for near-field optical recording, extensive studies have been carried out in the literature. A PSIM is interacted with a phase change medium [84]. The transverse field component of the electric field in the focal plane of the PSIM interacts with the medium, and mark sizes of $\lambda/4$ are obtained. In addition, a PSIM is integrated with a near-field transducer that is placed at the focus of the PSIM [85]. An incident light is coupled to the PSIM waveguide by a coupling grating, and the TE waveguide mode is focused by the PSIM on the near-field transducer. The electric field at the focal plane of the PSIM excites a surface plasmon resonance of the near-field transducer. The sharp tip of the transducer further enhances the focused field. Therefore, an intense optical spot beyond the diffraction limit is produced by the near-field transducer. Furthermore, Challener et. al. utilized from a near-field applications, such as data storage devices. This is mainly due to their size, large body mass, high price, and difficulty in manufacturing them in the large quantities required by these applications. Solid immersion lenses, apertures on metals, bow-tie antennas, ridge waveguides, tapered optical fibers, apertureless near-field techniques are among the possible ways to achieve intense optical spots with small sizes. These near-field techniques can be combined to further improve the performance. For example a bow-tie nano-antenna can

be placed at the focus of a solid immersion lens to obtain better transmission efficiency with a small optical spot. However, such a device has a number of disadvantages. Some practical applications, such as magneto-optical recording, require a small body mass since the optical device will be mounted on a slider. Therefore, an optical lens system with a massive solid immersion lens is not feasible. In addition, the cost of such an optical system is quite high, since it uses traditional lens manufacturing, such as grinding and polishing.

Thin film waveguides with planar lenses, mirrors, and nano-optical transducers hold promise to address these concerns. The body mass is small and they can be easily mounted on a slider. They can be mass-produced at low costs with lithographic and thin film deposition techniques known from modern integrated circuit processing. These techniques are compatible with the current manufacturing techniques of potential applications, therefore, they can be manufactured at the current manufacturing facilities. Thin film structures can make advanced optical devices more accessible to consumer electronics and research tools due to reduced cost. In addition, thin films provide a small body mass compared to traditional lenses, which makes some applications more feasible. A design that provides high transmission efficiency will be a major breakthrough to bring nano-optical devices into these applications. The need for highly efficient nano-optical systems has been increasing as the current technologies are approaching to their limits.

Light can be highly confined in one dimension within planar dielectric thin film waveguides. The simplest planar waveguide consists of a high index dielectric core laminated on both sides with lower index claddings. A large difference between the refractive indices of the core and cladding is desirable to provide the highest degree of confinement of the light energy within the waveguide. The thickness of the core layer also determines the degree of confinement. To confine the light in the other dimension, optical lenses and mirrors on the waveguide are necessary. Using lithographic techniques, micro-optical structures consisting of planar versions of lenses and mirrors can be etched over the planar waveguide. These lenses and mirrors can effectively confine and focus a propagating beam of light with high optical transmission efficiency into a spot smaller than the wavelength of incident light. The light confined with these planar lenses and mirrors will still be limited by the diffraction limit. To further improve

the optical resolution, a nano-optical transducer can be used. A nano-optical transducer can be placed at the focus of these planar mirrors and lenses to provide smaller optical spots for better resolution. A thin film waveguide with planar optical lenses having a nano-optical transducer at the focus can address the practical issues of different applications. Such a system can be mass-produced with lithographic and thin film deposition techniques known from modern integrated circuit processing.

Especially two specific planar micro-transducers gain interest in the literature to obtain diffraction-limited optical spots: A PSIM, and a planar solid immersion lens (PSIL). These micro-transducers are also utilized with nano-transducers to produce optical spots beyond the diffraction limit. A PSIM is a two-dimensional three-layer dielectric waveguide having a truncated parabolic geometry. It can obtain a diffraction-limited optical spot with a dimension that is about a quarter wavelength of an incident light $\sim \lambda_{inc}/4$ [83]. The focal point of the PSIM is at the center of the truncated part as shown in Figure 4.1 and Figure 4.2(a). This planar dielectric structure consists of a high index dielectric core region that is sandwiched between lower index cladding regions as seen in Figure 4.2(b). Due to the specific geometry of the PSIM an optical spot is obtained at the focus by two physical means: (a) A dielectric slab waveguide confines an incident light in the direction that is perpendicular to the plane of the waveguide. A field confinement in the waveguide core is in the direction perpendicular the plane of the waveguide, and (b) Waveguide modes that reflect from the parabolic edges on either sides of the waveguide propagate to the focal point of the parabola. A confined field via the parabolic edge is in the direction that is parallel to the plane of the waveguide. Therefore, a two-dimensional field confinement may be achieved by a PSIM. For an incident wavelength of $\lambda_{inc}=413$ nm, a FWHM spot size of 90 nm is obtained [83]. The reason for a field confinement by a PSIM with relatively small FWHM spot size is due to its high numerical aperture. Another reason is that a PSIM is free of chromatic aberration, hence all light rays entering it are incident on the focal point.

To demonstrate a PSIM for near-field optical recording, extensive studies have been carried out in the literature. A PSIM is interacted with a phase change medium [2].

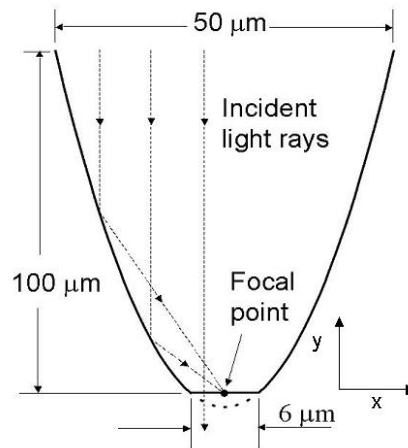


Figure 4.1 A schematic illustration of a PSIM. Light rays that enter the PSIM are reflected at different angles from the parabolic side walls at either sides to the focal point of the PSIM. Courtesy of Challener et.al., *Optics Express*, 13, 18 (2005).

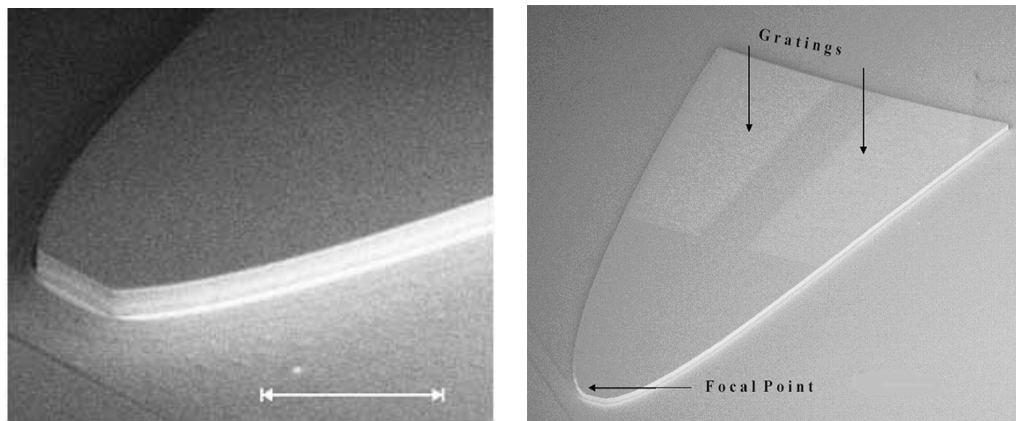


Figure 4.2 Images of fabricated PSIMs with $\text{Al}_2\text{O}_3/\text{Ta}_2\text{O}_5/\text{Al}_2\text{O}_3$ dielectric layers that sit on a ceramic substrate. (a) Light is incident on the two coupling gratings that are fabricated at the upper region of the PSIM, and (b) A three-layer PSIM with a high index core that is sandwiched between lower index claddings is shown. Courtesy of Rottmayer et.al., *IEEE Transactions on Magnetics*, 42, 10 (2006), and Challener et.al., *Optics Express*, 13, 18 (2005).

The transverse field component of the electric field in the focal plane of the PSIM interacts with the medium, and mark sizes of $\lambda/4$ are obtained. In addition, a PSIM is integrated with a near-field transducer that is placed at the focus of the PSIM [85]. An incident light is coupled to the PSIM waveguide by a coupling grating, and the TE waveguide mode is focused by the PSIM on the near-field transducer. The electric field at the focal plane of the PSIM excites a surface plasmon resonance of the near-field

transducer. The sharp tip of the transducer further enhances the focused field. Therefore, an intense optical spot beyond the diffraction limit is produced by the near-field transducer. Furthermore, Challener et. al. utilized from a near-field nanotransducer that is placed at the focus of a PSIM in a heat assisted magnetic recording system, which is integrated with a recording head [86]. The PSIM is integrated with the read/write coil of the recording head in vertical position, so the focal point of the PSIM and the nanotransducer fly a few nanometers above the magnetic recording disk. The PSIM waveguide has two coupling gratings that are vertically offset by half a period with respect to each other. An incident light on each grating excites a TE waveguide mode, and the electric field components of this mode has a phase difference of π with respect to each other in either sides of the PSIM. Due to this phase difference the electric field at the focus has vertical polarization. As a result, surface charge density oscillation of the nanotransducer is in the vertical direction. This oscillation produces an intense and localized electric field in the vicinity of the peg of the nanotransducer. Since a PSIM is a diffraction-limited transducer, it is utilized with a nanotransducer, therefore an intense optical spot with a size beyond the diffraction limit can be produced. An areal density of 375 Tb/m², and a track width of about 70 nm is observed in the recording medium.

4.2 Planar Transducers for Heat-Assisted Magnetic Recording

4.2.1 Planar Transducers With Diffraction-Limited Optical Spots

Light can be highly confined in one dimension within planar dielectric thin film waveguides. A simplest planar waveguide may consist of a high index dielectric core laminated on both sides with lower index dielectric claddings. A large difference between the refractive indices of the core and cladding is desirable to provide a high degree of confinement of the light energy within the waveguide. The thickness of the core layer also determines the degree of confinement. To confine the light in the other dimension, optical lenses and mirrors on the waveguide are necessary. Using lithographic techniques, micro-optical structures consisting of planar versions of lenses and mirrors can be etched over a planar waveguide to confine light in the other dimension, as shown in Figure 4.3. This planar micro-optical structure is called a planar solid immersion mirror (PSIM). Such lenses and mirrors can effectively confine and

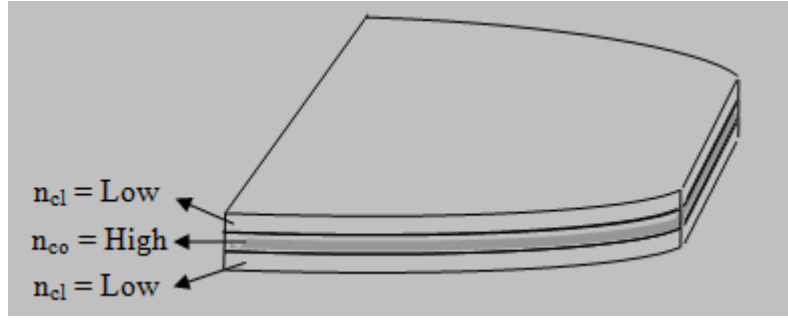


Figure 4.3 Schematic illustration of a planar dielectric waveguide with a high index core n_{co} laminated between lower index claddings n_{cl} that is etched into a planar mirror.

focus a propagating beam of light with high optical transmission efficiency into a spot smaller than the wavelength of incident light. The light confined via these planar lenses and mirrors will still be diffraction limited.

To obtain diffraction-limited optical spots smaller than an incident wavelength from a PSIM, firstly a TE_0 mode profile of a slab symmetric dielectric planar waveguide is investigated. Consider a slab symmetric waveguide with boundaries at $x = 0$ and $x = d$, as shown in Figure 4.4. Region 0 is the core region having a relative permittivity ϵ_{r0} . Region -1 and Region 1 are the cladding regions, which are semi-infinite. They have the same relative permittivity ϵ_{r1} . The relative permeability of the core μ_{r0} and cladding μ_{r1} is equal to 1. A transverse electric (TE) plane wave is incident on the waveguide, and propagates in the z -direction, as Figure 4.4 illustrates.

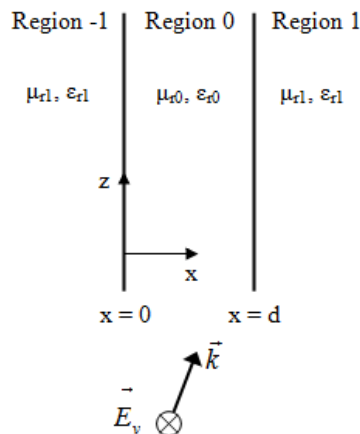


Figure 4.4 A TE plane wave is incident at an oblique incidence on the core and cladding regions of a symmetric slab waveguide. The relative permittivity of the core is ϵ_{r0} and that of the cladding is ϵ_{r1} . The thickness of the core region is d .

TE wave solutions of Maxwell's equations are considered in Region -1, 0, and 1. For wave guidance, the solutions for \mathbf{E}_{-1} and \mathbf{E}_1 outside the core region should be evanescent in the -x and x directions. As depicted in Equation (4.1) and (4.3), \mathbf{E}_1 decays in the x direction and \mathbf{E}_{-1} decays in the -x direction.

$$\vec{E}_1 = \hat{y}E_1 e^{-\alpha_{1x}x + ik_z z} \quad d \leq x \quad (4.1)$$

$$\vec{E}_0 = \hat{y}(A_0 e^{ik_x x} + B_0 e^{-ik_x x}) e^{-ik_z z} \quad 0 \leq x \leq d \quad (4.2)$$

$$\vec{E}_{-1} = \hat{y}E_{-1} e^{\alpha_{1x}x + ik_z z} \quad x \leq 0 \quad (4.3)$$

where E_1 , E_{-1} are the field amplitudes for the evanescent waves in Region 1 and -1, respectively. A_0 and B_0 are the field amplitudes in Region 0 and have a value of 1 V/m. k_x is the transverse wavenumber for waves in Region 0 and it is an unknown constant. α_{1x} is the attenuation constant for waves in the x direction and is an unknown constant. k_z is the longitudinal wavenumber and has an equal value for waves within the core and the cladding regions due to the phase matching condition. It is an unknown that may be specified from Equation (4.4) once α_{1x} is known.

The dispersion relations in Region 0 and Region 1 can be written as

$$k_z^2 - \alpha_{1x}^2 = \omega^2 \mu_1 \epsilon_1 = k_1^2 \quad (4.4)$$

$$k_z^2 + k_x^2 = \omega^2 \mu \epsilon = k^2 \quad (4.5)$$

where k and k_1 are the wave numbers for waves in the core and the cladding, respectively. ω is the operation frequency of the waveguide. To specify α_{1x} and k_x , the dispersion relation may be rewritten as

$$(k_x d)^2 + (\alpha_{1x} d)^2 = (k^2 - k_1^2) d^2 \quad (4.6)$$

where d is the thickness of the core. Equation (4.6) defines is a circle on the $\alpha_{1x} - k_x d$ plane with a radius of $r = \sqrt{(k^2 - k_1^2)} d$. Since there are two unknowns α_{1x} and k_x in

Equation (4.6) a second equation is required to reach for a solution. The guidance condition for a symmetric slab waveguide can be defined as

$$(\alpha_{1x}d) = \frac{\mu_1}{\mu} k_x d \tan\left(\frac{k_x d}{2} - \frac{m\pi}{2}\right) \quad (4.7)$$

where m is the mode of the guided wave. When Equation (4.6) is and (4.7) represent two curves, which intersect at a single point on the $\alpha_{1x} - k_x d$ plane for a specific value of m where $m = 0$ for a TE₀ mode. When Equation (4.7) is plugged into Equation (4.6) the resulting equation is a transcendental equation, and can be solved by graphical or iterative methods. Newton's iteration is utilized to determine specific values of the attenuation constant α_{1x} and the wavenumber k_x for $m = 0$.

In Figure 4.5, normalized electric field intensity distribution $|\mathbf{E}(x=0,y=0,z)|^2$ in a symmetric slab waveguide is plotted for various refractive indices of the core $n_{co}=1.5, 2, 2.5, 3$ is presented. The refractive index of the cladding is $n_{cl} = 1.4$, and the thickness of the core is $d = 105$ nm. A plane wave is incident with an amplitude of 1 V/m. The operation frequency of the waveguide is $1.52 \cdot 10^7$ rad/sec. As depicted in Figure 4.5, the electric field intensity $|\mathbf{E}(x=0,y=0,z)|^2$ varies in the core region, and it exponentially decays in the cladding regions. Therefore, an incident plane wave is confined within the core of the waveguide. The field intensity is maximum at the center of the core $x = 52.5$ nm. As Figure 4.5 shows, the FWHM intensity for $n_{co} = 1.5$ is $506 \text{ V}^2/\text{m}^2$ and that for $n_{co} = 3$ is $78 \text{ V}^2/\text{m}^2$.

The FWHM intensity can be improved by tuning the material and geometric parameters of the waveguide. Figure 4.6 demonstrates normalized electric field intensity distribution $|\mathbf{E}(x=0,y=0,z)|^2$ for $n_{co}=1.5, 2, 2.5, 3$. In Figure 4.6, the value of the cladding index is decreased to $n_{cl} = 1$. The core thickness is $d = 105$ nm. As seen, the FWHM intensity for $n_{co} = 1.5$ has decreased to $122 \text{ V}^2/\text{m}^2$ and that for $n_{co} = 3$ has decreased to $76 \text{ V}^2/\text{m}^2$.

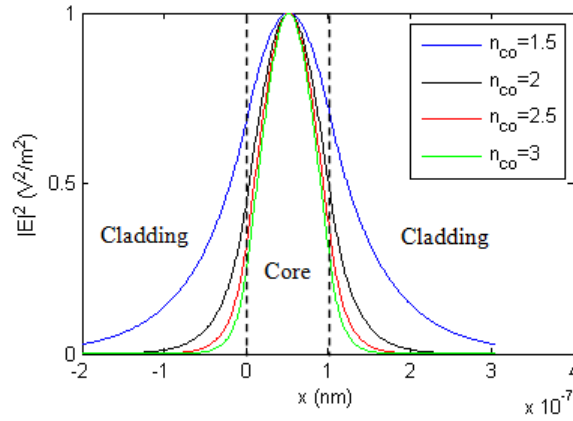


Figure 4.5 Normalized electric field intensity distribution $|E(x=0,y=0,z)|^2$ in a symmetric slab waveguide for various refractive indices of the core n_{co} . The refractive index of the cladding is $n_{cl}=1.4$. The thickness of the core is $d = 105$ nm.

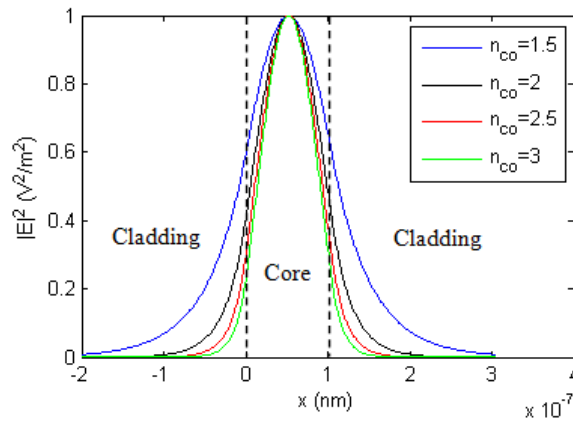


Figure 4.6 Normalized electric field intensity distribution $|E(x=0,y=0,z)|^2$ in a symmetric slab waveguide for various refractive indices of the core n_{co} . The refractive index of the cladding is $n_{cl}=1$. The thickness of the core is $d = 105$ nm.

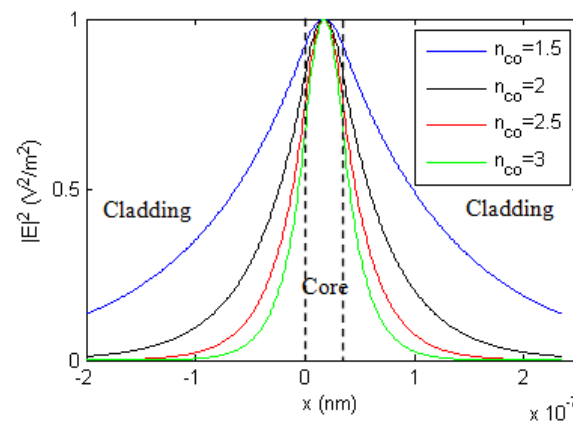


Figure 4.7 Normalized electric field intensity distribution $|E(x=0,y=0,z)|^2$ in a symmetric slab waveguide for various refractive indices of the core n_{co} . The refractive index of the cladding is $n_{cl}=1$. The thickness of the core is $d = 70$ nm.

In Figure 4.7, the thickness of the core layer is decreased to $d = 70$ nm. The cladding index is $n_{cl} = 1$. As seen, FWHM intensity value for $n_{co} = 1.5$ and 3 has dropped to $471 \text{ V}^2/\text{m}^2$ and to $61 \text{ V}^2/\text{m}^2$, respectively. Figure 4.8 presents normalized electric field intensity distribution $|\mathbf{E}(x=0,y=0,z)|^2$ for various core thicknesses $d = 70$ nm and $d = 210$ nm. The core index is chosen as $n_{co} = 4$, and the cladding index is chosen as $n_{cl} = 1$. As seen, the electric field can be better confined in the waveguide core when the core thickness is smaller. FWHM field intensity for $d = 70$ nm and $d = 210$ nm are $79 \text{ V}^2/\text{m}^2$ and $145 \text{ V}^2/\text{m}^2$, respectively. A drop in the core thickness results in an increase in FWHM intensity.

In Figure 4.9, FWHM intensity profile is plotted as a function of the core thickness d . An increase in FWHM intensity is observed between $d = 10$ -70 nm, and a decrease occurs between $d = 10$ -140 nm. For a specific core thickness FWHM decreases as n_{co} increases. Furthermore, a difference in FWHM for $n_{co} = 1.5$ and 2 is larger than for $n_{co} = 2.5$ and 3 at a specific core thickness. Therefore, to increase n_{co} beyond 3 will decrease the FWHM intensity very little. The most evident drop in FWHM is observed between $n_{co} = 1.5$ and $n_{co} = 2$ for a specific core thickness. In addition, when the core thickness is greater than about 8 nm a difference in FWHM intensity for $n_{co} = 2$ and 2.5 is closer to a difference for $n_{co} = 2.5$ and 3 for a specific core index.

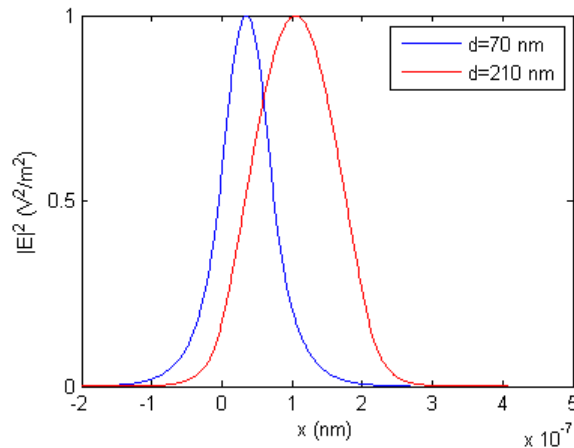


Figure 4.8 Normalized electric field intensity distribution $|\mathbf{E}(x=0,y=0,z)|^2$ in a symmetric slab waveguide for various core thicknesses $d = 70$ nm and $d = 210$ nm. The refractive indices of the core is $n_{co} = 4$ and that of the cladding is $n_{cl} = 1$. The right boundary of the core region is varied from $x = 70$ nm to $x = 210$ nm. The left boundary is kept constant at $x = 0$ nm.

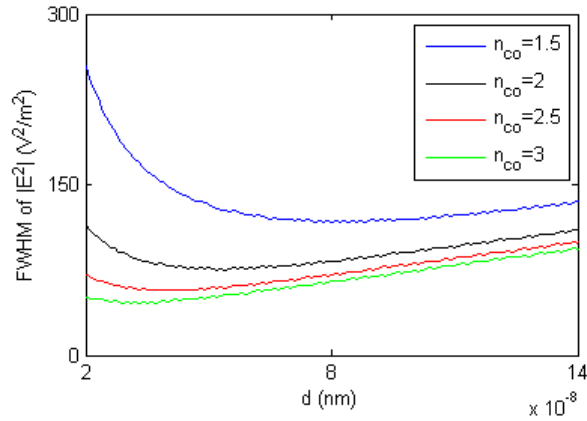


Figure 4.9 Full-width half maximum of electric field intensity $|E(x=0,y=0,z)|^2$ profile as a function of the core thickness for $n_{co} = 1.5, 2, 2.5,$ and 3 . The index of the cladding is $n_{cl} = 1$.

FWHM of electric field intensity $|E(x=0,y=0,z)|^2$ profile as a function of the core index n_{co} for specific values of the core thickness d is presented in Figure 4.10. As seen, for a specific value of d , FWHM intensity decreases as n_{co} increases. In addition, for a specific value of n_{co} , FWHM intensity decreases as d increases.

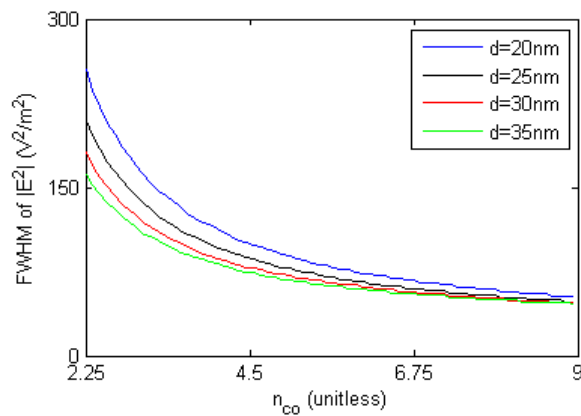


Figure 4.10 Full-width half maximum of electric field intensity $|E(x=0,y=0,z)|^2$ profile as a function of the core index n_{co} for $d = 20, 25, 30,$ and 35 nm. The index of the cladding is $n_{cl} = 1$.

4.2.2 Planar Transducers With Optical Spots Beyond the Diffraction-Limit

4.2.2.1 Introduction

Light can be focused with a dielectric PSIM to produce optical spots with dimensions about a quarter of the incident wavelength. Diffraction-limit hinders the structure to obtain smaller optical spots. On the other hand, the hard disc drive industry requires a continual increase in the size of magnetic information storage devices, which stipulates to obtain smaller optical spots. Since feature dimensions are proportional to the wavelength of the electromagnetic wave that produces the feature, surface plasmons, due to their short wavelength, may be utilized to pass over the diffraction-limit.

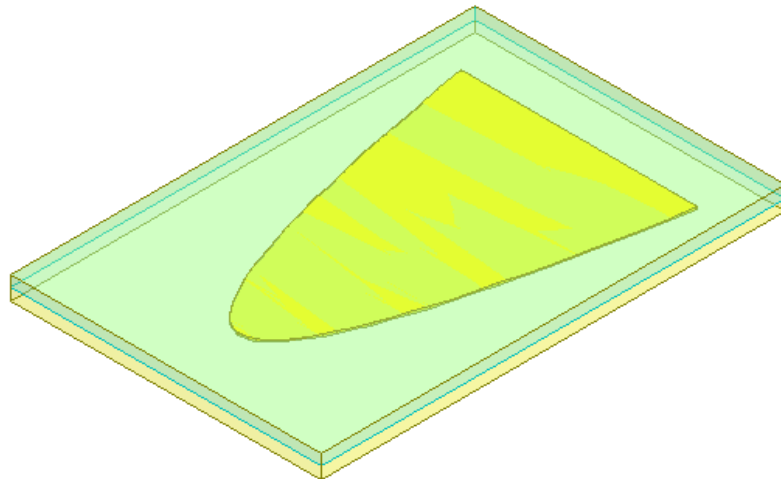


Figure 4.11 The plasmonic planar solid immersion mirror (plasmonic PSIM).

In this study, a plasmonic counterpart of the dielectric PSIM is introduced to obtain optical spots beyond the diffraction limit. To analyze this problem, a 3-D frequency-domain finite element method (FEM) is utilized. The total electric field E^t is composed of the incident field E^i and scattered field E^s . In this study, the incident field is a plane wave. To obtain the scattered field E^s a FEM based full-wave solution of Maxwell's equations is utilized. To represent the scattering geometries accurately, tetrahedral elements are used to discretize the computational domain. On the tetrahedral elements, edge basis functions and second-order interpolation functions are used. Adaptive mesh

refinement is used to improve the coarse solution regions with high field intensities and large field gradients.

In this study, a plasmonic PSIM is investigated to obtain optical spots beyond the diffraction limit. The geometry in Figure 4.11 is the Kretschmann configuration, where a gold layer that is etched into a parabola is sandwiched between a high-index dielectric superstrate and a lower index dielectric substrate, as shown in Figure 4.11. The high-index layer is chosen to increase the value of the incident wave vector to the surface plasmon wave vector in order to excite surface plasmons on the gold thin-film. A p-polarized light is incident on the PSIM, which excites surface plasmons on the upper surface of the PSIM. The magnitude of the incident field is selected as 1 V/m in this study. Thus, the electric field intensity values that are obtained correspond to intensity enhancements. The operation wavelength is selected as $\lambda = 633$ nm. The dielectric constant of gold at 633 nm is $\epsilon_1 = -18.01 - 0.0474i$.

4.2.2.2 Plasmonic PSIMs

Plasmonic PSIMs with various numerical apertures (NA) are presented in Figure 4.12 and Figure 4.13. The dielectric index of the superstrate and substrate is selected as $n_0 = 2.5$ and $n_2 = 1$, respectively. As seen in Figure 4.13(c), the spot size can be reduced to 391 nm x 217 nm by using a high NA plasmonic PSIM. Two factors contribute to increase the resolution. Optical rays that have higher incident angles upon reflection from the side walls, and the excitation of short-wavelength plasma waves on the PSIM. In these configurations however, the plasmon wavelength very close to the photon wavelength; therefore optical spots are still diffraction-limited.

In order to significantly reduce the plasmon wavelength, higher index substrates for the gold layer can be utilized. The relation between the substrate index and plasmon wavelength for surface plasmons at a metal/dielectric interface may be given as

$$\lambda_{spp} \approx \sqrt{\frac{\epsilon'_1 + \epsilon_2}{\epsilon'_1 \epsilon_2}} \lambda \quad (4.8)$$

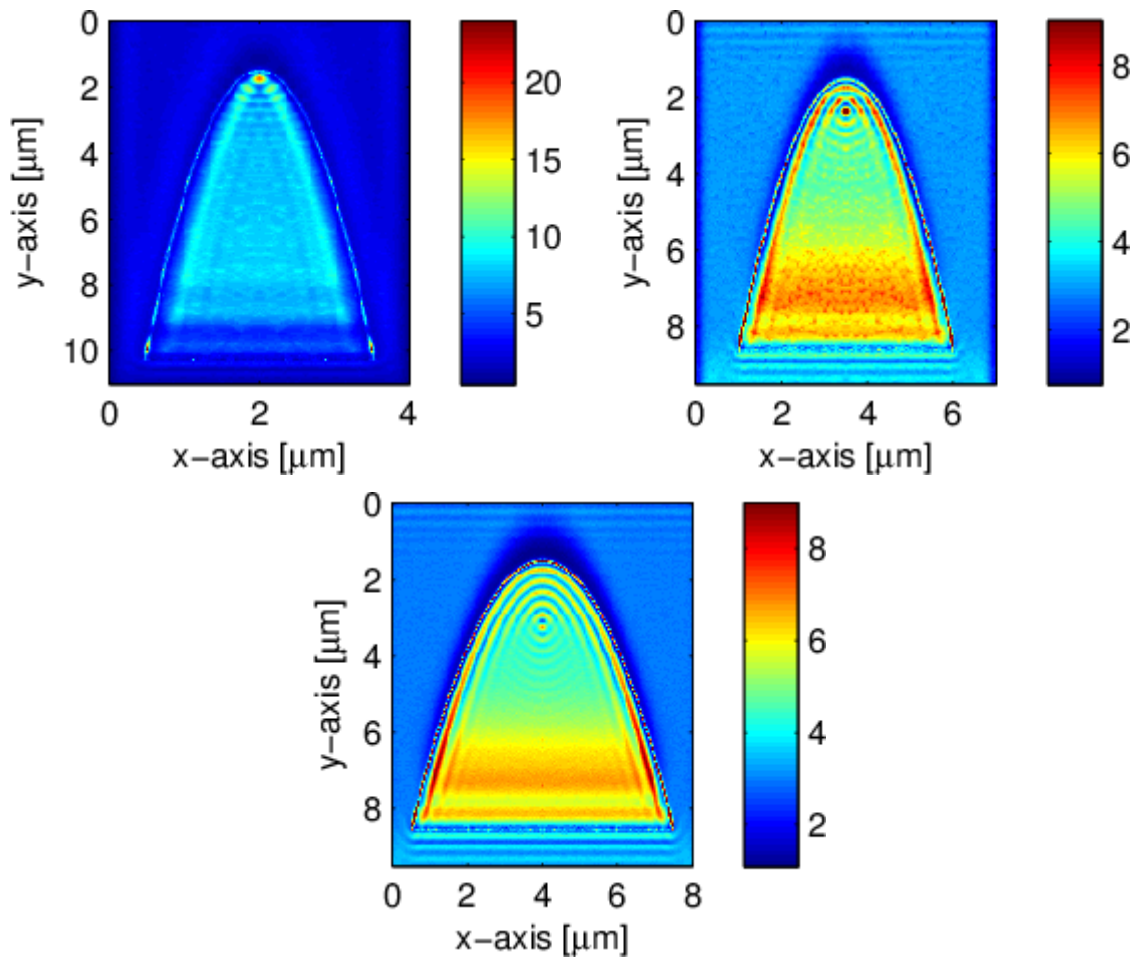
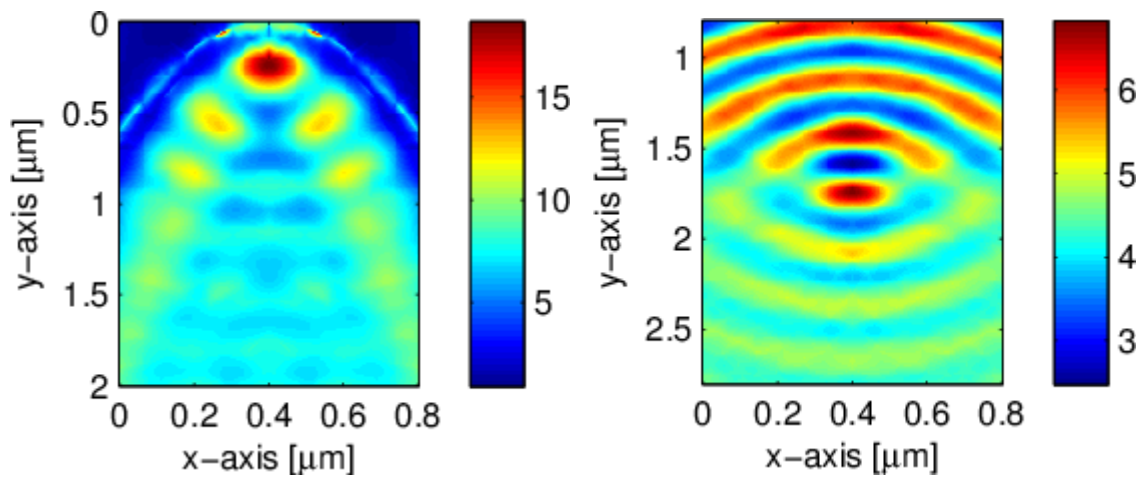


Figure 4.12 Plasmonic PSIM designs with various numerical apertures. The dielectric index of the superstrate and substrate is selected as $n_0=2.5$, and $n_2=1$, respectively. The incident wavelength is 633 nm.



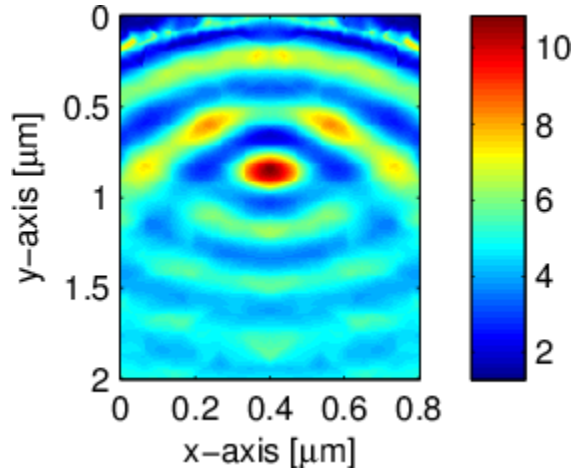


Figure 4.13 A closer view of optical spots for various numerical apertures. (a), (b) and (c) represent the electric field intensity distributions along the $z=0$ cut-plane $|\mathbf{E}(x,y,z=0)|$. The dielectric index of the superstrate and substrate is selected as $n_0=2.5$, and $n_2=1$, respectively. The incident wavelength is 633 nm.

where λ_{spp} is the plasmon wavelength and λ is the excitation wavelength in vacuum. ϵ'_1 and ϵ_2 are the relative permittivities of the metal and dielectric semi-infinite layers. In Figure 4.14, the plasmon wavelength is represented as a function of the refractive index of the dielectric layer n_2 for an incident wavelength of $\lambda = 633$ nm. As seen in Figure 4.14, the plasmon wavelength is $\lambda_{\text{spp}} = 615$ nm for $n_2 = 1$, and reduces to $\lambda_{\text{spp}} = 53$ nm for $n_2 = 4$, which corresponds to a ratio of about $\lambda_{\text{spp}} = \lambda/12$.

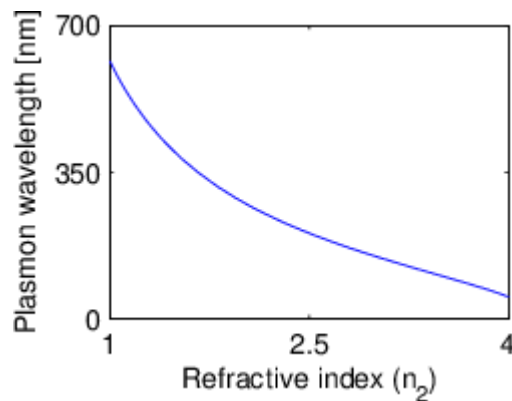


Figure 4.14 Surface plasmon wavelength in an dielectric/metal configuration as a function of the refractive index of the dielectric medium n_2 . The incident wavelength is $\lambda = 633$ nm.

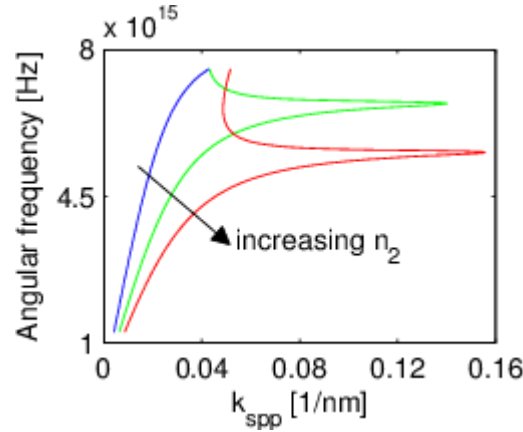


Figure 4.15 Dispersion relations of surface plasmons at a metal/dielectric interface as a function of various dielectric indices $n_2 = 1, 1.5,$ and 2 .

Various dispersion relations of surface plasmons at a metal/dielectric interface support the above theoretical arguments, as presented in Figure 4.15. As seen in Figure 4.15, when the dielectric index is increased higher k_{spp} values are obtained for an incident wavelength of $\lambda = 633$ nm. More specifically, for an incident wavelength of $\lambda = 633$ nm plasmon wavelengths of $\lambda_{spp} = 615$ nm, 394 nm, and 279 nm are obtained for dielectric indices of $n_2 = 1, 1.5,$ and 2 , respectively. Thus, utilizing from higher index substrates, optical spot dimensions can be significantly reduced.

The substrate index is not the only factor that has an effect on the plasmon wavelength. It should be recalled that the plasmonic PSIM is build upon the Kretschmann configuration. Thus, a superstrate should be utilized to ensure the phase matching condition. The superstrate index is also crucial in obtaining smaller optical spots. For the Kretschmann configuration the parallel component of the wavevector can be given as

$$k_x = n_0 \frac{\omega}{c} \sin(\theta_{spp}) \quad (4.9)$$

where n_0 is the refractive index of the superstrate, ω is the operation frequency, and θ_{spp} is resonant angle for surface plasmon excitation. The parallel wavevector k_x is aimed to be increased to reduce the spot size. As seen in Equation (4.9), for a specific operation

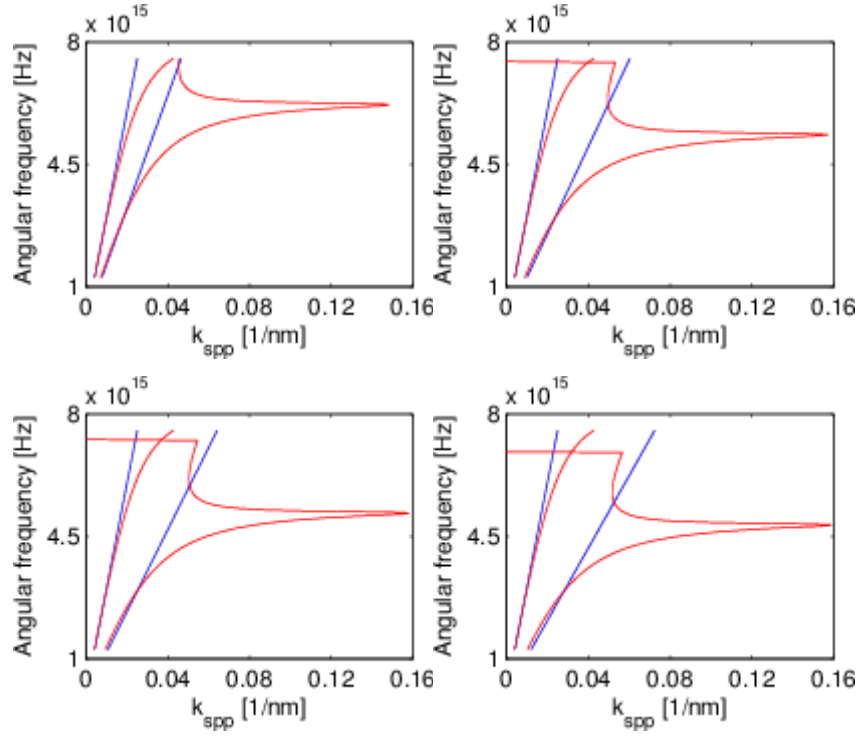


Figure 4.16 Dispersion relations of plasmonic PSIMs with various substrate and superstrate indices. The dispersion relation for a metal/air interface, as well as the light line in air is given as a reference. (a) $n_0 = 2$, $n_2 = 1.7$, (b) $n_0 = 2.6$, $n_2 = 2.1$, (c) $n_0 = 2.8$, $n_2 = 2.2$, and (d) $n_0 = 3.2$, $n_2 = 2.4$. The incident wavelength is 633 nm.

frequency, k_x has a higher value when n_0 and θ_{spp} are increased. On the other hand, the value of the critical angle of total internal reflection (TIR) and n_0 are inversely proportional, as given in (4.10), and since resonance occurs just after the TIR condition is satisfied, θ_{spp} decreases as n_0 increases. Therefore, to obtain a higher value for θ_{spp} , the ratio n_2/n_0 can be increased. This allows increasing both θ_{spp} and n_0 in Equation (4.9) despite their inverse relation. Furthermore, since a higher value is obtained for n_2/n_0 ,

$$\sin(\theta_c) = \frac{n_2}{n_0} \quad (4.10)$$

n_2 is increased as well, which contributes to decrease the resolution as depicted in Equation (4.8)

Dispersion relations of plasmonic PSIMs with various substrate and superstrate indices are shown in Figure 4.16. The dispersion relation for a metal/air interface, as well as the

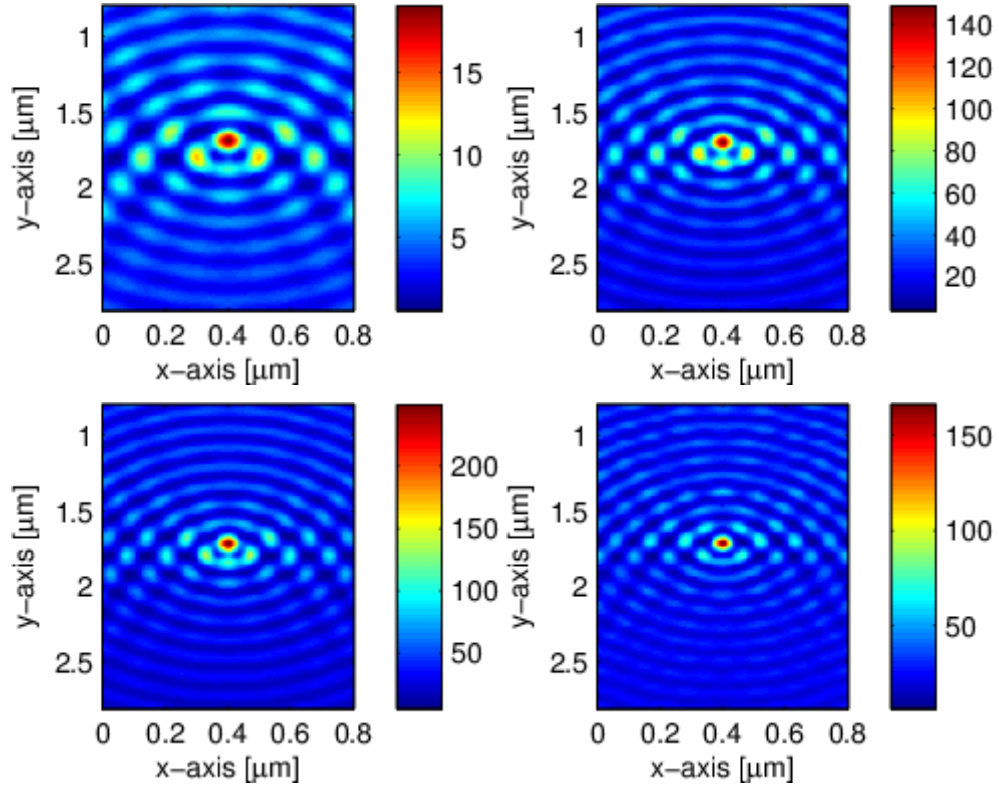


Figure 4.17 Plasmonic PSIMs with various substrate and superstrate indices. (a) $n_0 = 2$, $n_2 = 1.7$, (b) $n_0 = 2.6$, $n_2 = 2.1$, (c) $n_0 = 2.8$, $n_2 = 2.2$, and (d) $n_0 = 3.2$, $n_2 = 2.4$. The incident wavelength is 633 nm.

light line in air is also plotted as a reference. As seen, the dispersion relations provide a higher k_{spp} value for a specified operation frequency when the substrate index increases. Moreover, the light line for the substrate is tilted when the ratio n_2/n_0 increases, and intersects with the dispersion curve at higher k_{spp} values.

Plasmonic PSIMs with various substrate and superstrate indices are presented in Figure 4.17. As seen from the electric field intensity distributions in Figure 4.17(a)-(d), spot sizes of 169 nm x 122 nm, 133 nm x 102 nm, 119 nm x 97 nm, and 106 nm x 81 nm are obtained on the x-y plane of the plasmonic PSIM, respectively. These spot size correspond to a ratio of $\lambda/5$, $\lambda/6.2$, $\lambda/6.5$, and $\lambda/7.8$ for the incident wavelength. Surface plasmon wavelengths in these configurations are 342 nm, 266 nm, 251 nm, and 222 nm, respectively. Smaller spot sizes can be obtained as the plasmon wavelength decreases. Furthermore, as depicted in Figure 4.16, k_{spp} values as high as 0.16 [1/nm] can be obtained that corresponds to a plasmon wavelength of 39 nm by using higher index

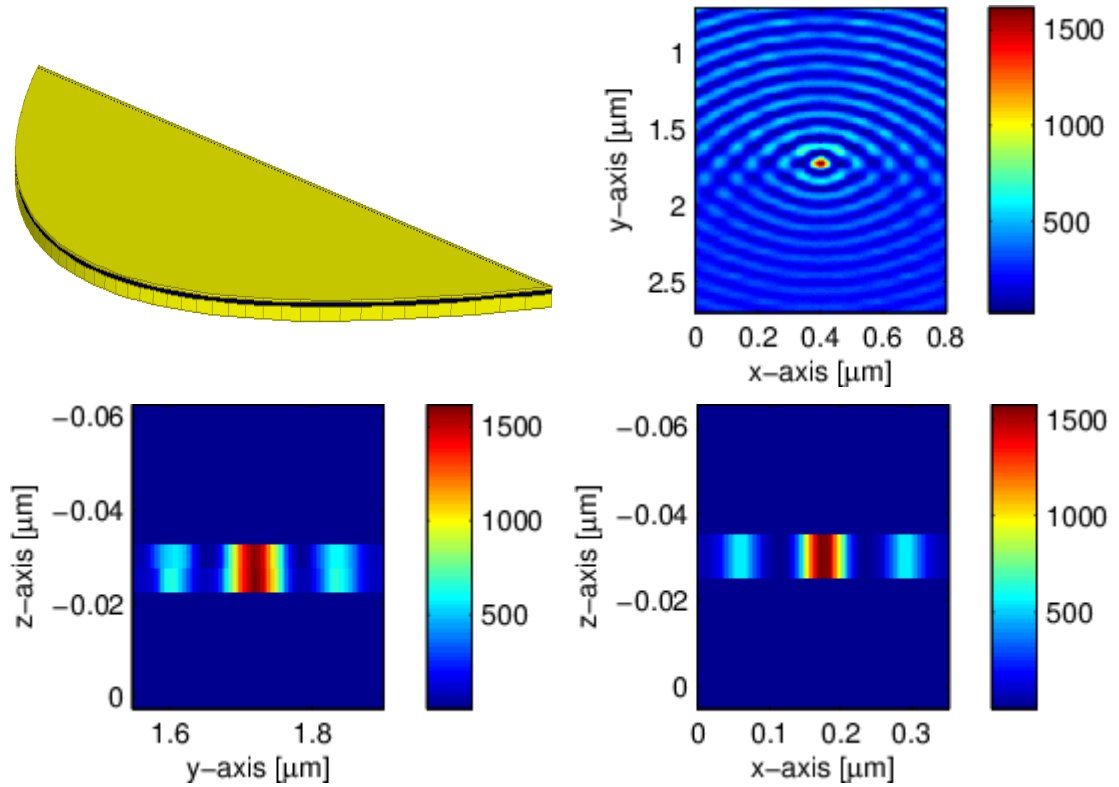


Figure 4.18 Plasmonic PSIMs in the form of metal/insulator/metal (MIM) configurations. (a) Schematic representation of the MIM geometry, (b) $|\mathbf{E}(x,y,z=0)|$, (c) $|\mathbf{E}(x=0,y,z)|$, and (d) $|\mathbf{E}(x,y=0,z)|$. Refractive index of the superstrate and the dielectric interlayer is selected as 3.2 and 1.2, respectively. The incident wavelength is 633 nm.

substrates in the Kretschmann configuration. Thus, in principle, it is possible to significantly reduce spot sizes below 39 nm. The interference patterns also provide information about the plasmon wavelength and the degree of confinement. As seen in Figure 4.17, the fringe spacing is about half of the plasmon wavelength. As the degree of confinement increases, the fringe spacing decreases.

The Kretschmann configuration provides a unique way to confine light in two dimensions by the plasmonic PSIM. However, along the thickness direction, the confinement may be weak due to the evanescent nature of the field in the substrate. In order to increase the confinement, a metal/insulator/metal (MIM) configuration can be utilized, as schematically represented in Figure 4.18(a). The bottom metal layer in the MIM configuration supports surface plasmons as the first layer, and when the spacing between the metal layers is sufficiently thin, surface plasmons couple to each other and

form a hybrid plasmon mode. In this configuration, the thickness of the insulator is selected as 10 nm, thus a higher confinement can be obtained as seen in is Figure 4.18(b) and Figure 4.18(c). In the x-y plane of the plasmonic PSIM, an optical spot with dimensions of 106 nm x 65 nm is obtained that corresponds to $\lambda/9.7$ in the y-direction.

4.2.3 Near-Field Scanning Optical Microscope (NSOM) Measurements of the Plasmonic PSIM

In order to demonstrate the operation of the plasmonic PSIM, near-field scanning optical microscopy (NSOM) measurements are performed. Various plasmonic PSIMs with a height of 8.7 μm and width of 6 μm are fabricated with electron beam lithography on fused silica substrates ($n_0=1.45$ at 633 nm). The PSIMs before and after the lift-off process are presented in Figure 4.19. Monochromatic p-polarized light with a

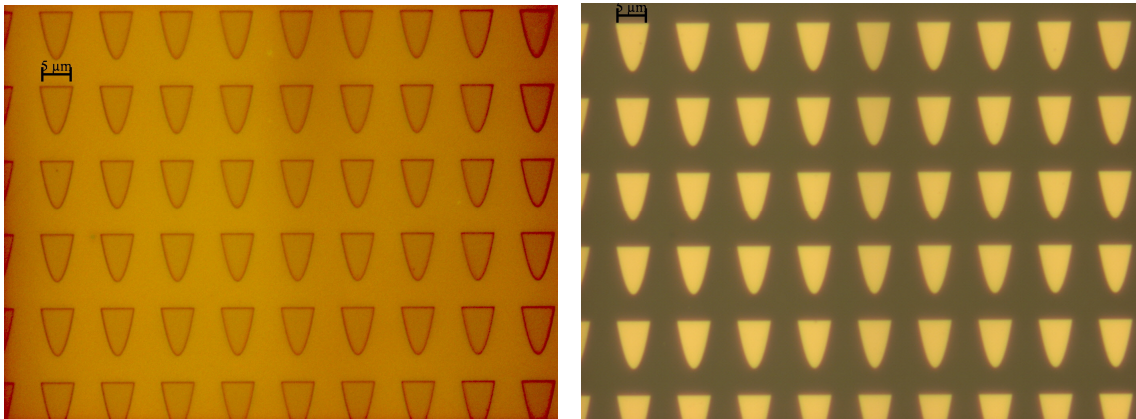


Figure 4.19 Plasmonic PSIMs (a) before lift-off, and (b) after lift-off. The height and width of the structures is 8.7 μm and 6 μm , respectively.

wavelength of 632.8 nm is oriented on the fused silica substrates at the open end of the PSIM and the incident angle is adjusted to satisfy TIR condition. After satisfying the TIR condition, the incident angle of the laser beam tuned to reduce the reflectivity from the plasmonic PSIMs. When surface plasmons are excited on the structures, the NSOM is utilized in the collection mode, and an NSOM tip with a 100 nm aperture is raster scanned on the structures. Figure 4.20 demonstrates various NSOM images of the plasmonic PSIMs. As seen in Figure 4.20(a) and Figure 4.20(b), the experimental and

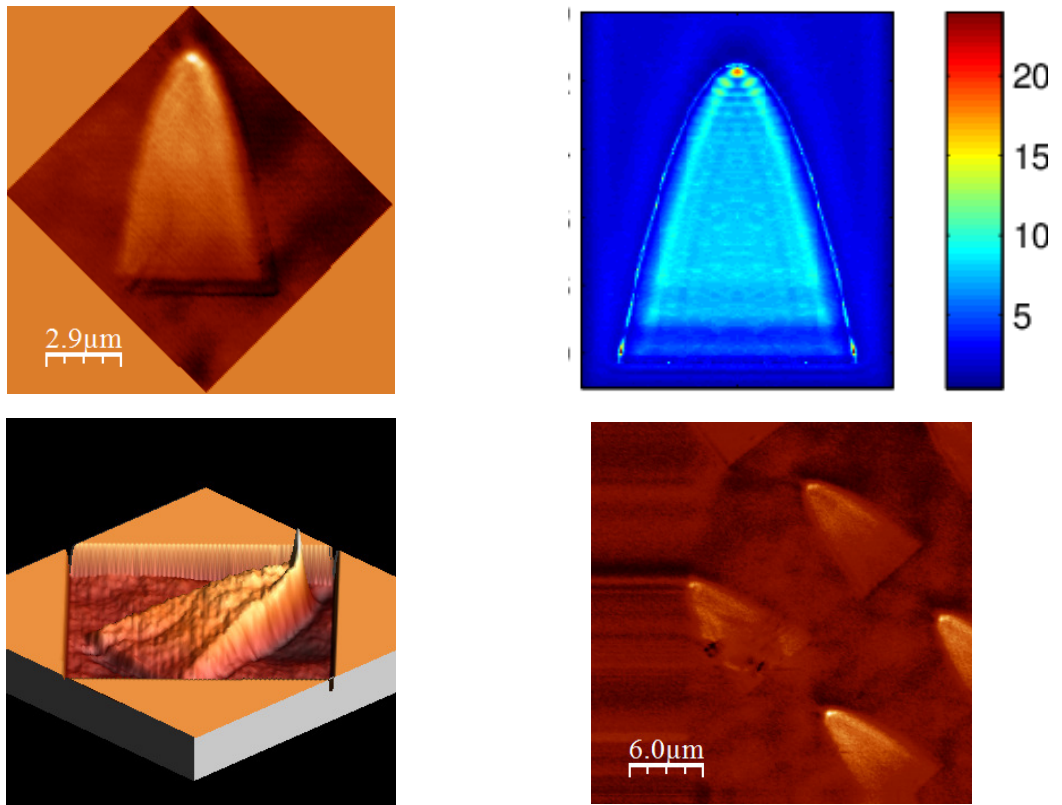


Figure 4.20 NSOM and simulation results of PSIMs. (a) 2D view of an NSOM image of a single PSIM, (b) simulation of a single PSIM, (c) 2D view of an array of PSIMs, and (d) 3D view of a single PSIM.

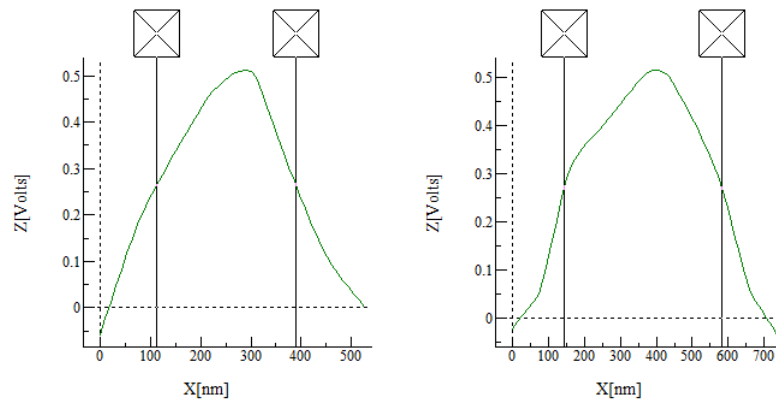


Figure 4.21 Intensity profiles along the x-direction and y-direction of the PSIM.

simulation results well agree with each other. As seen in Figure 4.21, optical spot sizes of 277 nm x 438 nm are obtained.

4.3 Conclusion

In conclusion, a dielectric PSIM is demonstrated that can produce diffraction-limited optical spots. The effect of core thickness and index of the core and claddings are investigated. It is shown that optical spot sizes can be reduced to about $\lambda/4$. Furthermore, various plasmonic PSIM designs are theoretically and experimentally demonstrated that can beat the diffraction-limit. Spot sizes of 106 nm x 65 nm are obtained with MIM configurations corresponding to $\lambda/9.7$. The plasmonic PSIMs are realized by electron beam lithography on fused silica substrates. NSOM measurements are performed where intense and localized optical spots are obtained. The theoretical and experimental results are shown to be in well agreement with each other.

5 RECOVERING DAMPED PLASMON RESONANCES IN SURFACE PLASMON RESONANCE SENSORS WITH LOSSY LAYERS

5.1 Introduction

Surface plasmon resonance (SPR) sensors have been extensively utilized in label-free and real-time characterization of thin-films and detection of binding events near metal interfaces. Due to their simplicity and effectiveness they are utilized in a variety of sensing applications such as biosensing [87], detection of foodborne pathogens [88,89,90] and Alzheimer disease biomarker [91], sensing of single viruses [92], and gas sensing experiments [93]. During their utilization in these applications, the performance characteristics of SPR sensors such as sensitivity, linearity, resolution, accuracy and limit of detection may be degraded by specific factors. One of the factors is the absorptive losses of the samples. Thin-film samples and analytes with high losses may influence the performance of SPR sensors negatively. Specifically, lossy samples may cause significant variations in the resonance characteristics of SPR sensors and make the sensors underperform during measurements.

Various studies in the literature have investigated the resonance characteristics of SPR sensors in the presence of lossy samples. In one of the studies, it was demonstrated that thick and strongly absorbing sample layers resulted in greater angular shifts in the reflectivity minimum than thin and weakly absorbing layers [94]. In addition, a lossy binding layer within the sensor has been shown to have a negative effect on the performance characteristics. When the thickness of the binding layer increased the resonance curve broadened and the value of the reflectivity minimum increased. In another study [95], Langmuir-Blodgett films containing dye molecules were deposited on silver surfaces. As a result, a broadening and a decrease in the depth of the reflectivity signal was observed. Operating SPR sensors in the presence of highly lossy samples is important to fulfill the performance characteristics of SPR sensors. Specific

sensor configurations are therefore required that can provide a higher performance in the presence of lossy samples.

In this study, it is demonstrated that surface plasmon resonances are broadened and shifted in the presence of highly absorbing thick-film samples, and it is theoretically shown that the damped resonances can be recovered with simple configurations resulting in sharper resonances. A glass-gold-sensing-dielectric-cobalt configuration is investigated, and the permittivity and thickness of the dielectric layer is adjusted to recover surface plasmon resonances.

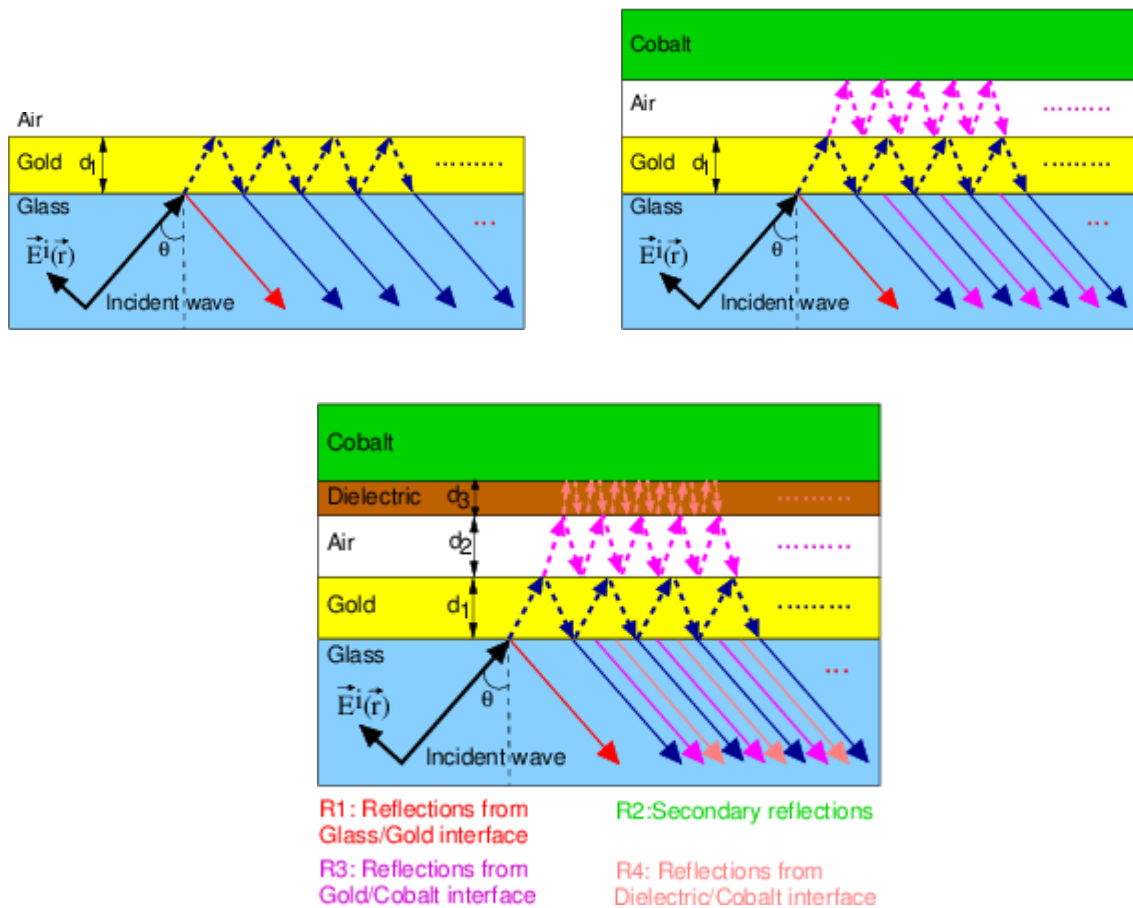


Figure 5.1 Schematic illustration of the (a) Kretschmann configuration, (b) a glass-gold-air-cobalt configuration, and (c) a glass-gold-sensing-dielectric-cobalt configuration.

A p-polarized plane wave is obliquely incident on the glass/gold interface of various multilayers at an incident angle of θ , as illustrated Figure 5.1. The glass layer is utilized to excite surface plasmons on the gold thin-film by increasing the wavevector of the incident wave in glass to the wavevector of surface plasmons. The magnitude of the incident field is selected as $|E_i(r)| = 1$ V/m in this study. Thus, the electric field intensity values correspond to intensity enhancements in the multilayer. The operation wavelength is selected as $\lambda = 633$ nm. The dielectric constants of gold and cobalt at 633 nm are $\epsilon_g = -9.51 + 1.15i$ and $\epsilon_c = -12.49 + 18.45i$, respectively [96].

5.2 Methodology

In this study, SPR sensors in the form of multilayer configurations with glass, gold, dielectric and cobalt films are investigated to increase their sensing performance in the presence of lossy samples. To analyze this problem, various methodologies are followed. In the first methodology, the poles of various multilayer systems are obtained by the transfer functions of the systems and tuned to recover the plasmon resonances of the systems. After recovering the resonances, a second methodology is followed to present the performance enhancement of the sensor configurations by obtaining the electric field intensity profiles of the configurations. In the following sections, these two methodologies are discussed in a detail.

5.2.1 Obtaining and Tuning the Poles of Various SPR Sensor Configurations to Recover Plasmon Resonances

Surface plasmons are collective charge-density oscillations that propagate along the interface between a noble metal and a dielectric medium. As illustrated in Figure 5.1(a), they can be practically excited via a glass-metal-sensing configuration. As illustrated in Figure 5.1(b), when a lossy sample such as cobalt is deposited on the sensing layer of the glass-metal-sensing configuration, surface plasmons can no longer be excited due to the high optical losses of cobalt. To recover plasmon resonances various methodologies can be followed. A specific methodology that is treated in this

study is to express the plasmon resonances with their corresponding transfer functions and tuning the poles of the transfer functions to obtain higher quality resonances. Since the transfer function of a multilayer system is basically the reflectance response of the system to an incident wave, the resonance characteristics can be identified and tuned by investigating the transfer functions of the system.

The transfer function of a glass-metal-sensing layer can be expressed as

$$r_{pms} = \frac{r_{pm} + r_{ms} \exp(2ik_{mz}d_1)}{1 + r_{pm}r_{ms} \exp(2ik_{mz}d_1)} \quad (5.1)$$

and

$$r_{ms} = \frac{k_{mz}\epsilon_s - k_{sz}\epsilon_m}{k_{mz}\epsilon_s + k_{sz}\epsilon_m} \quad (5.2)$$

where r_{ms} and r_{pm} is the reflectivity of a metal-sensing and glass-metal bilayer, respectively. k_{mz} and k_{sz} is the magnitude of the perpendicular component of the wavevector in layer m and s , respectively. ϵ_m and ϵ_s is the relative permittivity of the metal and sensing layer, respectively. The parameter r_{ms} in Equation (5.2) can be denoted as the transfer function of the metal-sensing interface of the glass-metal-sensing configuration, which is illustrated in Figure 5.1(a). A strong pole of this transfer function exists when its denominator $k_{mz}\epsilon_s + k_{sz}\epsilon_m$ is zero [100]. The existence of a strong pole indicates itself by assigning practically very high values to the transfer function r_{ms} in Equation (5.2). A pole of a system may be strong or weak depending on the value of the denominator. When a strong pole exists, surface plasmons are at resonance; however when a weaker pole exists, surface plasmons of the corresponding system may be damped. For the glass-metal-sensing configuration, strong poles may be expected because surface plasmons are excited via this configuration.

When a cobalt layer is deposited on the sensing layer of the glass-metal-sensing configuration a new introduced to the system. The new transfer function of the resulting glass-gold-sensing-cobalt multilayer can be expressed as

$$r_{pmc} = \frac{r_{pm} + r_{msc} \exp(2ik_{mz}d_3)}{1 + r_{pm}r_{msc} \exp(2ik_{mz}d_3)} \quad (5.3)$$

and

$$r_{msc} = \frac{r_{ms} + r_{sc} \exp(2ik_{sz}d_1)}{1 + r_{ms}r_{sc} \exp(2ik_{sz}d_2)} \quad (5.4)$$

where r_{msc} is the transfer function and $1 + r_{ms}r_{sc} \exp(2ik_{sz}d_2)$ is the pole of the metal-sensing-cobalt multilayer when $1 + r_{ms}r_{sc} \exp(2ik_{sz}d_2) = 0$. In this case, surface plasmons may not be efficiently excited due to the presence of cobalt. Thus, the pole of the transfer function r_{msc} may be weakened. The weakened pole of the system should be recovered to obtain sharper resonances. Various configurations that will be addressed in this study aim to recover the weakened poles to obtain better quality plasmon resonances.

5.2.2 Obtaining the Electric Field Profiles of Various Multilayer Configurations

In this section, the propagation matrix method [97] is discussed, which is utilized to obtain the reflectivity curves, transfer functions, and electric field intensity profiles of various multilayers. Other methods also exist in the literature that is used to obtain the electric field intensity profiles in multilayer SPR sensors [98]. The propagation matrix method is especially useful in obtaining the field profiles in a recursive manner, therefore it is exploited in this study. The multilayer is illuminated with a p-polarized plane wave that can be expressed as

$$E^i(\vec{r}) = E_0^i(\vec{r}) \exp(i\vec{k}\vec{r}) \quad (5.5)$$

where \vec{E}_0^i is composed of tangential and perpendicular components to the quartz/gold interface. When the incident field \vec{E}^i interacts with the multilayer film, various primary and secondary reflections and transmissions occur at the interfaces that generate the scattered field \vec{E}^s . The total field \vec{E}^t is the summation of the incident field and scattered field. The electric field profiles are obtained from the total field in each layer. To obtain the total field the reflection coefficient of a five-layer multilayer [97] is utilized, which can be expressed as

$$R = \frac{\exp(2ik_{z0}d_0)}{R_{01}} + \frac{[1 - (1/R_{01}^2)]\exp[2i(k_{z0} + k_{z1})d_0]}{(1/R_{01})\exp(2ik_{z1}d_0)} + \frac{\exp[2ik_{z2}d_1]}{R_{12}} + \dots + \frac{[1 - (1/R_{23}^2)]\exp[2i(k_{z2} + k_{z3})(d_1 + d_2)]}{(1/R_{23})\exp[2ik_{z3}(d_1 + d_2)]} + R_{34} \exp[2ik_{z3}(d_1 + d_2 + d_3)] \quad (5.6)$$

where R_{01} , R_{12} , R_{23} , and R_{34} are the reflection coefficients of the glass-gold, gold-sensing, sensing-dielectric, and dielectric-cobalt interfaces, respectively. In addition, d_0 , d_1 , d_2 , and d_3 are the thicknesses of the gold, sensing, dielectric, and cobalt layers, respectively. k_{z0} , k_{z1} , k_{z2} , and k_{z3} are the transverse wave numbers in glass, gold, sensing, dielectric, and cobalt layers respectively. The vertical bar $|$ in the numerator of the second term in the reflection coefficient expression operates as a continued fraction. Due to the continued fraction form of the reflection coefficient expression, initially, the last term of the expression calculated and the calculation procedure is advanced to the first term. In this study, the reflectivity curves of various multilayers are obtained using Equation (5.6).

Considering the continuity of the tangential component of the electric field across an interface between two layers, a propagation matrix may be obtained that relates the electric field amplitudes of the total field in the quartz layer to other layers [97]. This matrix can be expressed as

$$\begin{bmatrix} E_m^r \exp(-ik_{zm}d_m) \\ E_m^i \exp(ik_{zm}d_m) \end{bmatrix} = \bar{\bar{V}}_{m(m-1)} \bar{\bar{V}}_{(m-1)(m-2)} \cdots \bar{\bar{V}}_{(l+1)(l)} \cdot \begin{bmatrix} E_l^r \exp(-ik_{zl}d_l) \\ E_l^i \exp(ik_{zl}d_l) \end{bmatrix} \quad (5.7)$$

where E_l^i and E_m^i are the incident field amplitudes, and the sub-index denotes the layer number. E_m^r and E_l^r are the reflected field amplitudes in layer l and layer m . For $m > l$ a forward propagation matrix is obtained that relates the field amplitudes of an upper layer to a lower layer. $\overline{\overline{V}}_{(l+1)(l)}$ is the propagation matrix, which relates the incident and reflected field amplitudes in layer l to that in layer $l+1$. As expressed in Equation (5.7), by the multiplication of propagation matrices the electric fields in various layers can be obtained. By adding the fields in each layer, the total field is obtained.

5.3 Results and Discussion

5.3.1 Damping of Plasmon Resonances Near Absorbing Layers

Damping of surface plasmon resonances in a multilayer system can be characterized by two features of the reflectivity curve of the system: the width and dip value. Surface plasmons in glass-metal-sensing configurations exhibit a sharp resonance and a zero dip value [99] when a gold thickness of 50 nm, and glass and sensing layer permittivities of 2.25 and 1.8 are utilized, respectively, as shown in Figure 5.2. The underlying reason for a zero dip value is due to the destructive interference between the incident and backscattered waves. An incident wave that is reflected from the glass-gold interface excites surface plasmons via its evanescent tail at the gold-sensing interface. The induced excitations at this interface radiate back to the glass layer, and they are in anti-phase with the incoming wave for certain thicknesses and dielectric constants of the constituting layers, causing destructive interference. As a consequence, the field intensity in the glass layer diminishes and yields a zero reflectivity value of the system.

When a cobalt layer is deposited on top of the sensing layer of the glass-metal-sensing configuration, the dip value of the reflectivity curve of the new configuration increases from 0 to 0.82, as depicted in Figure 5.2. The increase in the reflectivity points out that the backscattered and incoming waves are no longer anti-phase at the quartz-gold interface, which is as a result of the backscattered wave contributions of the cobalt-

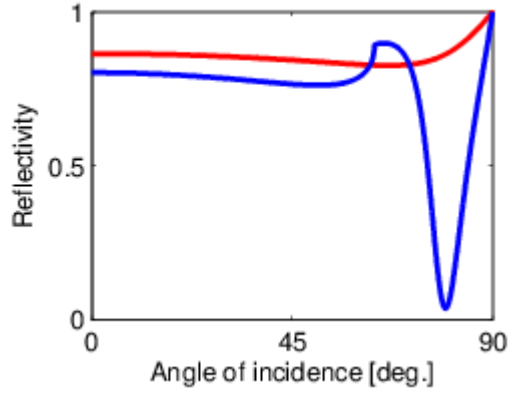


Figure 5.2 Reflectivity curve of (a) the glass-metal-sensing configuration, and (b) glass-gold-sensing-cobalt multilayer. The thickness of the gold and sensing layer is selected as 50 nm and 100 nm, respectively. The permittivity of the glass and the sensing layer is selected as 2.25 and 1.8, respectively.

sensing interface as illustrated in Figure 5.1(b). In addition to an increase in the dip position the linewidth of the resonance curve substantially increases. Furthermore, the dip position of the resonance curve shifts from 79.42° to 66.60° . As a result of the increase in the dip value of the resonance curve and broadening of the linewidth, the resonance of the four-layer configuration is almost completely lost, as seen in Figure 5.2. Since the deposition of the cobalt

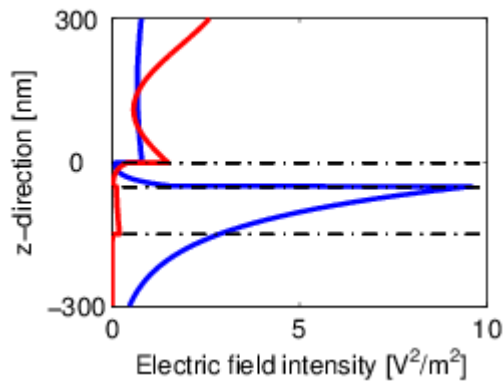


Figure 5.3 Electric field intensity profiles $|\vec{E}(x=0, y=0, z)|^2$ of metal-gold-sensing and metal-gold-sensing-cobalt multilayers.

layer degrades the resonance characteristics, the electric field intensity values near the sensing layers are reduced from 9.81 to $0.03 \text{ V}^2/\text{m}^2$.

5.3.2 Recovering Surface Plasmon Resonances with a Glass-Gold-Sensing-Dielectric-Cobalt Configuration

As mentioned in the previous section, the transfer function of the metal-sensing system has a very high value when a pole of the system exists. As seen in Figure 5.4, the transfer function $|r_{ms}|$ has a value of 758.10 at a resonance angle of 50.32°. On the other hand, when a cobalt layer is deposited on the sensing layer of the glass-metal-sensing configuration, the cobalt layer causes a decrease in the value the transfer function of the new configuration $|r_{msc}|$, decreasing to a value of 57.34 at 62.76°. The reduced value of the transfer function obviously suggests a very weak pole of the system. This pole causes damped plasmons resonances in the glass-metal-sensing-cobalt configuration. The intensity value at the gold-sensing interface also brings an evidence for damping of surface plasmons. The intensity value decreases to 0.03 V²/m² when the cobalt layer exists in the multilayer, as shown in Figure 5.3.

Damped surface plasmons can be recovered by gaining back the pole of the system. For this purpose, an additional dielectric layer with a specific thickness and permittivity may be introduced between the sensing and cobalt layer. As illustrated in Figure 5.1(c), the resulting configuration is a glass-gold-sensing-dielectric-cobalt configuration. The reflectivity expression of the novel configuration

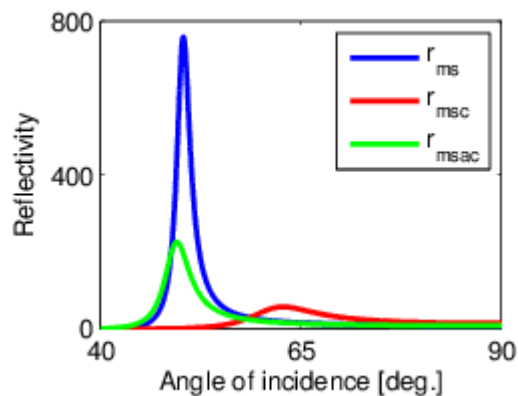


Figure 5.4 Transfer functions $|r_{ms}|$, $|r_{msc}|$, $|r_{msdc}|$ of gold-sensing, gold-sensing-cobalt, and gold-sensing-dielectric-cobalt multilayers, respectively.

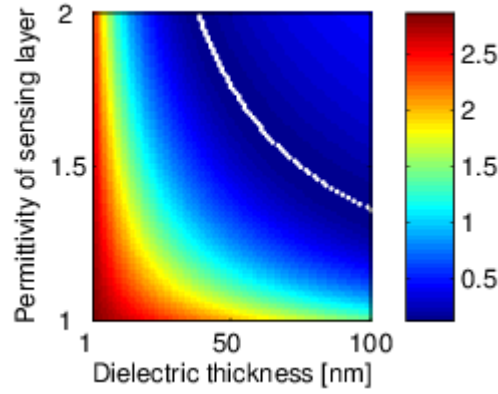


Figure 5.5 Two-dimensional dispersion plot of the sensing-dielectric-cobalt multilayer as a function of the dielectric thickness and permittivity of the sensing layer. White-dotted regions denote the reflectivity values for $|r_{sdc}| \approx 0$ of the multilayer.

can be expressed as

$$r_{pmsdc} = \frac{r_{pm} + r_{msdc} \exp(2ik_{mz} d_1)}{1 + r_{pm} r_{msdc} \exp(2ik_{mz} d_1)} \quad (5.8)$$

and

$$r_{msdc} = \frac{r_{ms} + r_{sdc} \exp(2ik_{sz} d_2)}{1 + r_{ms} r_{sdc} \exp(2ik_{sz} d_2)} \quad (5.9)$$

where r_{pmsdc} and r_{msdc} is the transfer function of the glass-metal-sensing-dielectric-cobalt and metal-sensing-dielectric-cobalt configuration. The parameter r_{sdc} is the transfer function of the sensing-dielectric-cobalt configuration. By tuning the thickness of the dielectric layer the value of r_{sdc} can be reduced. Then, the transfer functions $r_{msdc} \approx r_{ms}$ in Equation (5.9), and $r_{pmsdc} \approx r_{pms}$ in Equation (5.8). $r_{pmsdc} \approx r_{pms}$ physically signify that the resonance characteristics of the glass-metal-sensing-dielectric-cobalt and a glass-metal-sensing multilayer are the similar for a specific dielectric thickness. Since high quality resonances can be obtained by the glass-metal-sensing configuration, similar resonances can also be obtained by the glass-metal-sensing-dielectric-cobalt

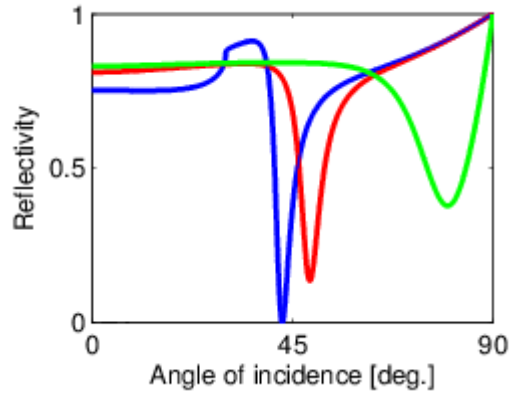


Figure 5.6 Reflectivity curve of (a) prism-gold-sensing, (b) prism-gold-sensing-dielectric multilayer and (c) prism-gold-sensing-dielectric-cobalt multilayer. The thickness of the gold, sensing, and dielectric layer is selected as 50 nm, 100 nm, and 40 nm, respectively. The relative permittivity of the prism, sensing, and dielectric layers is selected as 4, 1.8, and 1, respectively.

configuration by tuning the thickness of the dielectric layer. Thus, the pole of the system is recovered. The dielectric layer brings an additional degree of freedom to the multilayer system that allows to tune the value of the transfer function r_{sdc} .

Since the value of r_{sdc} depends on various parameters such as the dielectric thickness and the permittivity of the sensing layer, it can also be varied by utilizing from these parameters. Various $|r_{sdc}|$ values as a function of the dielectric thickness and the permittivity of the sensing layer are presented in Figure 5.5. As denoted by white-dotted regions in Figure 5.5, for various configurations $|r_{sdc}| \approx 0$. Specifically, for $d_3 = 100$ nm and $\epsilon_s = 1$ the reflectivity curve of the prism-metal-sensing-dielectric-cobalt multilayer is presented in Figure 5.6. As demonstrated in Figure 5.6, the reflectivity curve has a sharp resonance with an angular width of 9.14° . The angular width can be further increased by increasing the permittivity of the glass. As shown in Figure 5.6, when $\epsilon_p = 4$, angular width decreases to 6.52° . The angular width of this configuration has a value that is very close to the glass-metal-sensing configuration, which is 3.46° , as shown in Figure 5.6. Furthermore, electric field intensity profiles

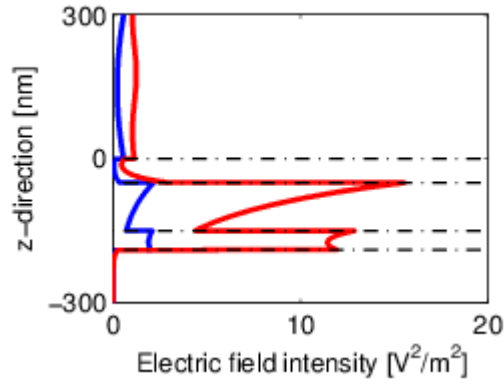


Figure 5.7 Electric field intensity profiles $|\vec{E}(x = 0, y = 0, z)|^2$ of glass-gold-sensing-dielectric-cobalt multilayers for glass permittivities of 2.25 and 4.

$|\vec{E}(x = 0, y = 0, z)|^2$ of glass-gold-sensing-dielectric-cobalt multilayers for various glass permittivities are presented in Figure 5.7. As shown in Figure 5.7, at the gold-sensing interface the intensity enhancement increases from 2.17 to 15.53.

5.4 Conclusion

In conclusion, multilayer surface plasmon resonance sensors with lossy samples are investigated. It is demonstrated that the plasmon resonances are broadened and shifted in the presence of the samples. A glass-gold-sensing-dielectric-cobalt configuration is investigated, and the permittivity and thickness of the dielectric layer is adjusted to recover the plasmon resonances. Utilizing from the transfer function of the configurations the poles of the transfer function are tuned to recover the resonances. For the recovered configurations enhanced electric field values are obtained on the sensing layer indicating recovered resonances.

6 CONCLUSION

In this thesis, multilayer configurations with plasmonic thin-films near magnetic films were investigated in various aspects, including HAMR and surface plasmon resonance sensors. For HAMR, the performance and reliability of integrated heads were investigated to reduce various losses that result due to the magnetic write head and other components of the head. The magnetic head and the plasmonic nanotransducer in a HAMR head are integrated with each other, which degrades the performance of the head due to various losses. Therefore, proper configurations should be specified to recover the performance of the integrated head.

This thesis investigates HAMR integrated heads that are modeled as multilayer configurations with plasmonic films near magnetic films. Various multilayer configurations of gold-cobalt films were investigated to increase the performance of integrated recording heads. Parametric studies were carried out to minimize internal damping and load-induced losses in the integrated head. Optimum configurations were identified for multilayer configurations that minimize internal damping, and load-induced losses due to the magnetic film. It was shown that a higher electric field intensity enhancement can be obtained on the magnetic film when evanescent coupling is stronger and load-induced damping is lower. This was obtained through adjusting layer thicknesses in multilayer configurations.

Furthermore, a specific approach was demonstrated to isolate the magnetic head from the plasmonic nanotransducer to reduce load-induced losses in this thesis. In order to protect the plasmonic transducer from the load-induced damping effect of the magnetic write head a novel planarly modeled HAMR head was introduced. A gold layer was placed near the magnetic layer in an integrated head. The gold layer behaved as a reflective coating between the plasmonic transducer and the magnetic film, and

reduced the damping effect of the magnetic head on the plasmonic transducer. Thus, a higher intensity enhancement from the nanotransducer could be obtained.

Moreover, the field gradient in the down-track direction was engineered for various configurations. By engineering the field gradients in the head, optimum configurations were specified that yielded higher field gradient regions in the down-track direction. It was shown that the gradient value varies with dielectric thickness, gold thickness, incident angle, and incident wavelength. Optimum values for these parameters were specified. It was also demonstrated that field gradient had a maximum and minimum value at the interfaces of the dielectric, and passed through a nearly zero value in between at the center.

This thesis also demonstrated a novel light delivery structure; the plasmonic PSIM, and investigated various characteristics of the structure both numerically and experimentally. Finite-element method simulations and near-field scanning electron microscopy experiments revealed intense and localized optical spots beyond the diffraction limit from the plasmonic PSIM that have dimensions as small as $1/60$ of the incident wavelength. Various plasmonic PSIM designs are theoretically and experimentally demonstrated that can beat the diffraction-limit. Spot sizes of as small as $106 \text{ nm} \times 65 \text{ nm}$ are obtained with MIM configurations corresponding to $\lambda/9.7$. The plasmonic PSIMs were produced by electron beam lithography on fused silica substrates. The theoretical and experimental results were in good agreement with each other.

The HAMR concept was left at the end of the thesis to investigate the underlying reasons of damped plasmon resonances in multilayered SPR sensors with thick lossy samples. Surface plasmon resonance sensors generally operate with lossless samples or lossy thin-films. On the other hand, when thick and lossy samples are present, surface plasmon resonances are affected by load-induced damping of the samples and therefore degrade, which negatively affects the performance of the sensors. Specific sensor configurations were presented that recover the plasmon resonances in the presence of lossy samples. It was demonstrated that plasmon resonances are broadened and shifted in the presence of lossy samples. A glass-gold-sensing-dielectric-cobalt configuration was investigated, and the permittivity and thickness of the dielectric layer was adjusted

to recover the plasmon resonances. Utilizing from the transfer function of the configurations the poles of the transfer function were tuned to recover the resonances. For the recovered configurations enhanced electric field values were obtained on the sensing layer indicating recovered resonances.

7 REFERENCES

- [1] S. I. Iwasaki and J. Hokkyo, *Perpendicular Magnetic Recording* (IOS, Amsterdam, 1991).
- [2] M. Mallary, A. Torabi, and M. Benakli, “One terabit per square inch perpendicular recording conceptual design,” *IEEE Trans. Magn.* **38**, 1719–1724 (2002).
- [3] R. Wood, “Feasibility of Magnetic Recording at 1 Terabit per Square Inch,” *IEEE Trans. Magn.* **36**, 36–42 (2000).
- [4] P. L. Lu and S. H. Charap, “Magnetic viscosity in high-density recording,” *J. Appl. Phys.* **75**, 5768–5770 (1994).
- [5] D. Weller and A. Moser, “Thermal effect limits in ultrahigh density magnetic recording,” *IEEE Trans. Magn.* **35**, 4423–4439 (1999).
- [6] T. W. McDaniel, W. A. Challener, and K. Sendur, “Issues in heat-assisted perpendicular recording,” *IEEE Trans. Magn.* **39**, 1972–1979 (2003).
- [7] M. H. Kryder, E. C. Gage, T.W. McDaniel, W. A. Challener, R. E. Rottmayer, G. Ju, Y.-T. Hsia, and M. F. Erden, “Heat Assisted Magnetic Recording,” *Proc. IEEE* **96**, 1810–1835 (2008).
- [8] W. A. Challener, C. Peng, A. V. Itagi, D. Karns, W. Peng, Y. Peng, X. Yang, X. Zhu, N. J. Gokemeijer, Y.-T. Hsia, G. Ju, R. E. Rottmayer, M. A. Seigler, and E. C. Gage, “Heat-assisted magnetic recording by a near-field transducer with efficient optical energy transfer,” *Nature Photon.* **3**, 220–224 (2009).
- [9] B. C. Stipe, T. C. Strand, C. C. Poon, H. Balamane, T. D. Boone, J. A. Katine, J.-L. Li, V. Rawat, H. Nemoto, A. Hirotsune, O. Hellwig, R. Ruiz, E. Dobisz, D. S. Kercher,

- N. Robertson, T. R. Albrecht and B. D. Terris, "Magnetic recording at 1.5 Pb m^{-2} using an integrated plasmonic antenna", *Nature Photon.* **4**, 484-488, (2010).
- [10] A. Q. Wu, Y. Kubota, T. Klemmer, T. Rausch, C. Peng, Y. Peng, D. Karns, X. Zhu, Y. Ding, E. K. C. Chang, Y. Zhao, H. Zhou, K. Gao, J.-U. Thiele, M. Seigler, G. Ju, and E. Gage, "HAMR Areal Density Demonstration of 1+ Tbps on Spinstand", *IEEE Trans. Magn.*, **49**, 779-782, (2013)
- [11] D. Weller, G. Parker, O. Mosendz, E. Champion, B. Stipe, X. Wang, T. Klemmer, G. Ju, and A. Ajan, "A HAMR Media Technology Roadmap to an Areal Density of 4 Tb/in²", *IEEE Trans. Magn.*, **50**, (2014).
- [12] L. Pan and D. B. Bogy, "Heat Assisted Magnetic Recording," *Nature Photon.* **3**, 189-190 (2009).
- [13] Challener, W.A., Mihalcea C., Peng C., and Pelhos K., *Optics Express*, **13**, 18 (2005).
- [14] J.-I. Ikemoto, Y. Imai, and S. Nakagawa, "Control of Curie Temperature of FePt(Cu) Films Prepared From Pt(Cu)/Fe Bilayers", *IEEE Trans. Magn.*, **44**, 11, (2008).
- [15] M. A. Seigler, W. A. Challener, E. Gage, N. Gokemeijer, G. Ju, B. Lu, K. Pelhos, C. Peng, R. E. Rottmayer, X. Yang, H. Zhou, and T. Rausch, "Integrated Heat Assisted Magnetic Recording Head: Design and Recording Demonstration," *IEEE Trans. Magn.*, vol. 44, no. 1, pp. 119-124, 2008.
- [16] M. H. Kryder, E. C. Gage, T. W. McDaniel, W. A. Challener, R. E. Rottmayer, G. Ju, Y-T Hsia, and M. F. Erden, "Heat Assisted Magnetic Recording," *Proc. IEEE*, vol. 96, no. 11, pp. 1810-1835, 2008.
- [17] D. Weller, G. Parker, O. Mosendz, E. Champion, B. Stipe, X. Wang, T. Klemmer, G. Ju, and A. Ajan, "A HAMR Media Technology Roadmap to an Areal Density of 4 Tb/in²," *IEEE Trans. Magn.*, vol. 50, no.1, 2014.

- [18] N. Zhou, E. C. Kinzel, and X. Xu, "Nanoscale ridge aperture as near-field transducer for heat-assisted magnetic recording," *Appl. Opt.*, vol. 50, no. 31, 2011.
- [19] D.-S. Lim and Y.-J. Kim, "Enhancement of Near-Field Optical Throughput using Double Grating Structure for HAMR Head," *Asia Pacific Magnetic Recording Conference*, pp. 1-2, 2006.
- [20] S. Hussain, S. Y. Siew, C. S. Bhatia, H. Yang, A. J. Danner, "Characterization of near field transducers for high density heat assisted magnetic recording combined with FePt recording media," *Photonics Global Conference*, pp. 1-5 2012.
- [21] Y. Kong, M. Chabalko, E. Black, S. Powell, J. A. Bain, T. E. Schlesinger, and Yi Luo, "Evanescent Coupling Between Dielectric and Plasmonic Waveguides for HAMR Applications," *IEEE Trans. Magn*, vol. 47, pp. 2364-2367, 2011.
- [22] W. A. Challener, C. Mihalcea, C. Peng, and K. Pelhos, "Miniature planar solid immersion mirror with focused spot less than a quarter wavelength," *Opt. Express*, vol. 13, no. 18, pp. 7189-7197, 2005
- [23] C. Peng, W. A. Challener, A. Itagi, M. Seigler, and E. C. Gage, "Surface-Plasmon Resonance Characterization of a Near-Field transducer," *IEEE Trans. Magn*, vol. 48, pp. 1801-1806, 2012.
- [24] C. Peng, "Efficient excitation of a monopole optical transducer for near-field recording," *Appl. Phys. Lett.*, 112, 043108, 2012.
- [25] A. Ghoreyshi and R. H. Victora, "Heat assisted magnetic recording with patterned FePt recording media using a lollipop near field transducer," *J. Appl. Phys.* 115, 17B719, 2014.
- [26] B. Xu, Z. Cen, Y. T. Toh, J. Li, K. Ye, and J. Z., "Efficiency Analysis of Near Field Optical Transducer Used in Heat-Assisted Magnetic Recording," *IEEE Trans. Magn.*, vol. 49, pp. 3580-3583, 2013.

- [27] S. Hussain, C. S. Bhatia, H. Yang, and A. J. Danner, "Effect of FePt on resonant behaviour of a near field transducer for high areal density heat assisted magnetic recording," *Appl. Phys. Lett.*, 104, 111107, 2014.
- [28] L. Miao and T. Y. Hsiang, "Tapered Waveguide Design for Heat-Assisted Magnetic Recording Applications," *IEEE Trans. Magn.*, vol. 50, no. 1, 2014.
- [29] S. Omodani, T. Saiki, and M. Obara, "Metallic slit aperture as a near-field optical head for heat-assisted magnetic recording," *J. Appl. Phys.*, 105, 013101, 2009.
- [30] T. Matsumoto, F. Akagi, M. Mochizuki, H. Miyamoto, and B. Stipe, "Integrated head design using a nanobeak antenna for thermally assisted magnetic recording," *Opt. Express*, vol. 20, no. 17, pp. 18946-18954, 2012.
- [31] C. Peng, C. Mihalcea, D. Büchel, W. A. Challener, and E. C. Gage, "Near-field optical recording using a planar solid immersion mirror," *Appl. Phys. Lett.*, 87, 151105, 2005.
- [32] W. A. Challener, C. Peng, A. V. Itagi, D. Karns, W. Peng, Y. Peng, X. Yang, X. Zhu, N. J. Gokemeijer, Y.-T. Hsia, G. Ju, R. E. Rottmayer, M. A. Seigler, and E. C. Gage, "Heat-assisted magnetic recording by a near-field transducer with efficient optical energy transfer," *Nature Photon.*, vol. 3, no. 4, pp. 220-224, 2009.
- [33] B. C. Stipe, T. C. Strand, C. C. Poon, H. Balamane, T. D. Boone, J. A. Katine, J.-L. Li, V. Rawat, H. Nemoto, A. Hirotsune, O. Hellwig, R. Ruiz, E. Dobisz, D. S. Kercher, N. Robertson, T. R. Albrecht, and B. D. Terris, "Magnetic recording at 1.5 Pb m⁻² using an integrated plasmonic antenna," *Nature Photon.*, vol. 4, no. 7, pp. 484-488, 2010.
- [34] K. Şendur and W. Challener, "Patterned medium for heat assisted magnetic recording," *Appl. Phys. Lett.*, 94, 032503, 2009.

- [35] B. Xu, Z. Cen, J. H. Goh, J. Li, K. Ye, J. Zhang, H. Yang, Y. T. Toh, and C. Quan, "HAMR Media Design in Optical and Thermal Aspects," *IEEE Trans. Magn.*, vol. 49, no. 6, 2013.
- [36] T. Rausch, J. A. Bain, D. D. Stancil, and T. E. Schlesinger, "Thermal Williams–Comstock Model for Predicting Transition Lengths in a Heat Assisted Magnetic Recording System" *IEEE Trans. Magn.*, vol. 40, no. 1, 2004.
- [37] D.-S. Lim, M.-H. Shin, H.-S. Oh, and Y.-J. K., "Opto-Thermal Analysis of Novel Heat Assisted Magnetic Recording Media Based on Surface Plasmon Enhancement" *IEEE Trans. Magn.*, vol. 45, no. 10, 2009.
- [38] Q. D. Zhang, B. X. Xu, J. Zhang, N. Y. Liu, G. L. Chin, K. Sundaravadivelu, and E. H. Ong, "Numerical Investigation of Thermal Problems in Heat-Assisted Magnetic Recording System," *IEEE Trans. Magn.*, vol. 45, no. 11, 2009.
- [39] J. Li, B. Xu, Z. Cen, J. Zhang, and K. Ye, "Power Absorption and Thermal Analysis of Head and Media for Heat-Assisted Magnetic Recording," *IEEE Trans. Magn.*, vol. 49, no. 7, 2013.
- [40] S. Xiong, J. Kim, Y. Wang, X. Zhang, and D. Bogy, "A two-stage heating scheme for heat assisted magnetic recording," *Appl. Phys. Lett.*, 115, 17B702, 2014.
- [41] N. J. Gokemeijer, H. Zhou, D. Karns, S. Batra, M. Mallery, T. McDaniel, M. Seigler, G. Ju, Y. Peng, M. Xiao, and E. Gage, "Effect of gradient alignment in heat assisted magnetic recording," *Appl. Phys. Lett.*, 105, 07B905, 2009.
- [42] A. F. Torabi, J. V. Ek, E. Champion, and J. Wang, "Micromagnetic Modeling Study of Thermal Gradient Effect in Heat-Assisted Magnetic Recording (HAMR)" *IEEE Trans. Magn.*, 45, 10, 2009.

- [43] D. Regatos, B. Sepúlveda, D. Fariña, L. G. Carrascosa, and L. M. Lechuga, "Suitable combination of noble/ferromagnetic metal multilayers for enhanced magneto-plasmonic biosensing," *Opt. Express*, vol. 19, no. 9, 2011.
- [44] J. C. Banthí, D. Meneses-Rodríguez, F. García, M. U. González, A. García-Martín, A. Cebollada, and G. Armelles, "High Magneto Optical Activity and Low Optical Losses in Metal-Dielectric Au/Co/Au–SiO₂ Magnetoplasmonic Nanodisks", *Adv. Mater.*, vol. 24, no. 10, 2002.
- [45] J. B. González-Díaz, B. Sepúlveda, A. García-Martín, and G. Armelles, "Cobalt dependence of the magneto-optical response in magnetoplasmonic nanodisks," *Appl. Phys. Lett.*, 97, 043114, 2010.
- [46] D. Martín-Becerra, J. B. González-Díaz, V. V. Temnov, A. Cebollada, G. Armelles, T. Thomay, A. Leitenstorfer, R. Bratschitsch, A. García-Martín, and M. U. González, "Enhancement of the magnetic modulation of surface plasmon polaritons in Au/Co/Au films", *Appl. Phys. Lett.*, 97, 183114, 2010.
- [47] V. V. Temnova , G. Armelles, U. Woggon, D. Guzatov, A. Cebollada, A. Garcia-Martin, J.-M. Garcia-Martin, T. Thomays, A. Leitenstorfers and R. Bratschitschs, "Active magneto-plasmonics in hybrid metal-ferromagnet structures," *Nature Photon.*, 4, 2, pp. 107-111, 2010.
- [48] D. Weller and A. Moser, "Thermal effect limits in ultrahigh density magnetic recording," *IEEE Trans. Magn.*, vol. 35, pp. 4423-4439, 1999.
- [49] P. L. Lu and S. H. Charap, "Magnetic viscosity in high-density recording," *J. Appl Phys.*, vol. 75, pp. 5768-5770, 1994.
- [50] M. H. Kryder et al., "Heat-assisted magnetic recording," *Proc. IEEE*, vol. 96, pp. 1810-1835, 2008.

- [51] M. A. Seigler et. al., "Integrated heat assisted magnetic recording head: design and recording demonstration," *IEEE Trans. Magn.*, vol. 44, pp. 119-124, 2008.
- [52] W. A. Challener et al., "Heat-assisted magnetic recording by a near-field transducer with efficient optical energy transfer," *Nat. Photonics*, vol. 3, pp. 220-224, 2009.
- [53] B. C. Stipe et al., "Magnetic recording at 1.5 Pb m⁻² using an integrated plasmonic antenna," *Nat. Photonics*, vol. 4, pp. 484-488, 2010.
- [54] R. E. Rottmayer et. al., "Heat-assisted magnetic recording," *IEEE Trans. Magn.*, vol. 42, pp. 2417-2421, 2006.
- [55] Y. Kong et al., "Evanescent coupling between dielectric and plasmonic waveguides for HAMR applications," *IEEE Trans. Magn.*, vol. 47, pp. 2364-2367, 2011.
- [56] T. W. McDaniel, W. A. Challener, and K. Sendur, "Issues in heat-assisted perpendicular recording," *IEEE Trans. Magn.*, vol. 39, pp. 1972-1979, 2003.
- [57] W. Peng, Y.-T. Hsia, K. Sendur, and T. McDaniel, "Thermal-magnetic-mechanical analysis of head disk interface in heat assisted magnetic recording," *Tribology Int.*, vol. 38, pp. 588-593, 2005.
- [58] K. Sendur and W. Challener, "Patterned medium for heat assisted magnetic recording," *Appl. Phys. Lett.*, vol. 94, 032503, 2009.
- [59] K. Sendur, "Perpendicular oriented single-pole nano-optical transducer," *Opt. Exp.*, vol. 18, pp. 4920-4930, 2010.
- [60] T. Matsumoto, F. Akagi, M. Mochizuki, H. Miyamoto, and B. Stipe, "Integrated head design using a nanobeak antenna for thermally assisted magnetic recording," *Opt. Exp.*, vol. 20, pp. 18946 -18954, 2012.
- [61] V. V. Temnov et al., "Active magneto-plasmonics in hybrid metal-ferromagnet structures," *Nat. Photonics*, vol. 4, pp. 107-111, 2009.

- [62] D. Regatos, B. Sepúlveda, D. Fariña, L. G. Carrascosa, and L. M. Lechuga, "Suitable combination of noble/ferromagnetic metal multilayers for enhanced magneto-plasmonic biosensing," *Opt. Exp.*, vol. 19, pp. 8336-8346, 2011.
- [63] E. D. Palik, *Handbook of Optical Constants of Solids*. San Diego, CA: Academic Press, 1998.
- [64] J. A. Kong, *Electromagnetic Wave Theory*. Cambridge, MA: EMW Publishing, 2000.
- [65] W. C. Chew, *Waves and Fields in Inhomogeneous Media*. NY: IEEE Press, 1995.
- [66] M. H. Kryder et al., "Heat-assisted magnetic recording," *Proc. IEEE*, vol. 96, pp. 1810-1835, 2008.
- [67] R. E. Rottmayer et. al., "Heat-assisted magnetic recording," *IEEE Trans. Magn.*, vol. 42, pp. 2417-2421, 2006.
- [68] M. A. Seigler et. al., "Integrated heat assisted magnetic recording head: design and recording demonstration," *IEEE Trans. Magn.*, vol. 44, pp. 119-124, 2008.
- [69] W. A. Challener et al., "Heat-assisted magnetic recording by a near-field transducer with efficient optical energy transfer," *Nat. Photonics*, vol. 3, pp. 220-224, 2009.
- [70] B. C. Stipe et al., "Magnetic recording at 1.5 Pb m^{-2} using an integrated plasmonic antenna," *Nat. Photonics*, vol. 4, pp. 484-488, 2010.
- [71] X. Wang, K. Gao, H. Zhou; A. Itagi, M. Seigler, E. Gage., "HAMR Recording Limitations and Extendibility" *IEEE Trans. Magn.*, vol. 49, pp. 686-692, 2013.
- [72] H. J. Richter, C. C. Poon, G. Parker, M. Staffaroni, O. Mosendz, R. Zakai, and B. C. Stipe, "Direct Measurement of the Thermal Gradient in Heat Assisted Magnetic Recording", *IEEE Trans. Magn.*, vol. 49, pp. 5378-5381, 2013.

- [73] T. Rausch, J. A. Bain, D. D. Stancil, and T. E. Schlesinger, "Thermal Williams–Comstock Model for Predicting Transition Lengths in a Heat-Assisted Magnetic Recording System," *IEEE Trans. Magn.*, vol. 40, pp. 137-147, 2004.
- [74] T. W. McDaniel, W. A. Challener, and K. Sendur, "Issues in heat-assisted perpendicular recording," *IEEE Trans. Magn.*, vol. 39, pp. 1972-1979, 2003.
- [75] W. Peng, Y.-T. Hsia, K. Sendur, and T. McDaniel, "Thermal-magnetic-mechanical analysis of head disk interface in heat assisted magnetic recording," *Tribology Int.*, vol. 38, pp. 588-593, 2005.
- [76] K. Sendur and W. Challener, "Patterned medium for heat assisted magnetic recording," *Appl. Phys. Lett.*, vol. 94, 032503, 2009.
- [77] Y. Kong et al., "Evanescent coupling between dielectric and plasmonic waveguides for HAMR applications," *IEEE Trans. Magn.*, vol. 47, pp. 2364-2367, 2011.
- [78] E. Ogut, M. P. Menguc, and K. Sendur, "Integrating Magnetic Heads With Plasmonic Nanostructures in Multilayer Configurations," *IEEE Trans. Magn.*, vol. 49, pp. 3687-3690, 2013.
- [79] K. Sendur, "Perpendicular oriented single-pole nano-optical transducer," *Opt. Exp.*, vol. 18, pp. 4920-4930, 2010.
- [80] N. J. Gokemeijer, H. Zhou, D. Karns, S. Batra, M. Mallery, T. McDaniel, M. Seigler, G. Ju, Y. Peng, M. Xiao, and E. Gage, "Effect of gradient alignment in heat assisted magnetic recording," *Appl. Phys. Lett.*, vol. 105, 2009.
- [81] J. A. Kong, *Electromagnetic Wave Theory*. Cambridge, MA: EMW Publishing, 2006.
- [82] J. A. Dionne, L. A. Sweatlock, H. A. Atwater, and A. Polman, "Plasmon slot waveguides: Towards chip-scale propagation with subwavelength-scale localization," *Phys. Rev. B*, vol. 73, 035407, 2006.

- [83] Rottmayer, S. Batra, D. Buechel, W. Challener, J. Hohlfeld, Y. Kubota, L. Li, B. Lu, C. Mihalcea, K. Mountfield, K. Pelhos, C. Peng, T. Rausch, M. Seigler, D. Weller, and X. Yang, "Heat-assisted magnetic recording," *IEEE Trans. Mag.* **42**, 2417–2421 (2006).
- [84] P. L. Lu and S. H. Charap, "Magnetic viscosity in high-density recording," *J. Appl. Phys.* **75**, 5768-5770 (1994).
- [85] D. Weller and A. Moser, "Thermal effect limits in ultrahigh density magnetic recording," *IEEE Trans. Magn.* **35**, 4423–4439 (1999).
- [86] S. I. Iwasaki and J. Hokkyo, *Perpendicular Magnetic Recording* (IOS, Amsterdam, 1991).
- [87] B. Liedberg, C. Nylander, I. Lundstrom, Surface plasmon resonance for gas detection and biosensing, *Sens. Actuators*, 4 (1983), 299-304.
- [88] V. Koubova, E. Brynda, L. Karasova, J. Skvor, J. Homola, J. Dostalek, P. Tobiska, J. Rosick, Detection of foodborne pathogens using surface plasmon resonance biosensors, *Sens. Actuators B: Chem*, 74 (2001), 100-105.
- [89] V. Velusamy, K. Arshak, O. Korostynska, K. Oliwa, C. Adley, An overview of foodborne pathogen detection: In the perspective of biosensors, *Biotechnol. Adv.*, 28 (2010), 232-254.
- [90] A. D. Taylor, J. Ladd, Q. Yu, S. Chen, J. Homola, S. Jiang, Quantitative and simultaneous detection of four foodborne bacterial pathogens with a multi-channel SPR sensor, *Biosens. Bioelectron.*, 22 (2006), 752-758.
- [91] K. Hegnerova, M. Bockova, H. Vaisocherov´a, Z. Kristofikova, J. Rıcný, D. Rıpova, J. Homola, Surface plasmon resonance biosensors for detection of Alzheimer disease biomarker, *Sens. Actuators B: Chem*, 139 (2009), 69-73.

- [92] S. Wang, X. Shan, U. Patel, X. Huang, J. Lu, J. Li, N. Tao, Label-free imaging, detection, and mass measurement of single viruses by surface plasmon resonance, *Proc. Natl. Acad. Sci.*, 107 (2010), 16028-16032.
- [93] A. Berriera, P. Oermans, R. Cools, B. van Megen, W. Knoben, G. Vecchi, J. G. Rivas, M. Crego-Calama, S. H. Brongersma, Enhancing the gas sensitivity of surface plasmon resonance with a nanoporous silica matrix, *Sens. Actuators B: Chem*, 160 (2011), 181-188.
- [94] S. Ekgasita, A. Tangcharoenbumrungsuka, F. Yub, A. Babab, W. Knollb, Resonance shifts in SPR curves of nonabsorbing, weakly absorbing, and strongly absorbing dielectrics, *Sens. Actuators B: Chem*, 105 (2005), 532-541.
- [95] C. R. Lawrence, A. S. Martin, J. R. Sambles, Surface plasmon polariton studies of highly absorbing Langmuir-Blodgett films, *Thin Solid Films*, 208 (1992), 269-273
- [96] E. D. Palik, *Handbook of Optical Constants of Solids*, Academic Press, San Diego, 1998.
- [97] J. A. Kong, *Electromagnetic Wave Theory*, EMW Publishing, Cambridge, 2000.
- [98] A. Shalabney, I. Abdulhalim, Electromagnetic fields distribution in multilayer thin film structures and the origin of sensitivity enhancement in surface plasmon resonance sensors, *Sens. Actuators A: Physical*, 159 (2010), 24-32.
- [99] E. Kretschmann, The determination of the optical constants of metals by excitation of surface plasmons, *Z. Physik*, 241 (1971), 313-324.
- [100] K. Kurihara, K. Nakamura, K. Suzuki, Asymmetric SPR sensor response curve-fitting equation for the accurate determination of SPR resonance angle, *Sens. Actuators B: Chemical*, 86 (2002), 49-57.